THE HOST GALAXIES OF LUMINOUS REDDENED QUASARS AT $z \sim 2$

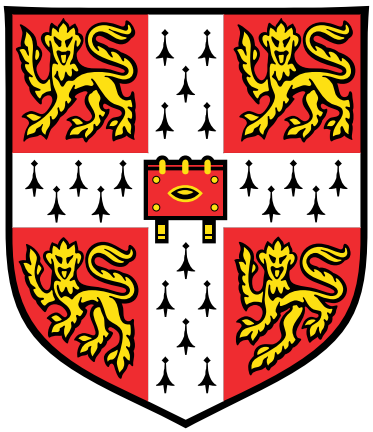

CLARE WETHERS

Supervisors: Manda Banerji & Paul Hewett

Institute of Astronomy

University of Cambridge

This dissertation is submitted for the degree of

Doctor of Philosophy

DARWIN COLLEGE JUNE 2018

Abstract

THE HOST GALAXIES OF LUMINOUS REDDENED QUASARS AT Z$\sim$ 2

CLARE WETHERS

The work in this thesis concerns the host galaxies of a class of luminous, yet heavily-obscured, quasars at z$\sim$2 - a peak epoch of both star formation and black hole accretion. Here, we seek to characterise the star-forming properties of these obscured quasars to improve our understanding of galaxy-quasar coevolution.

A key issue facing host galaxy studies among populations of the most luminous quasars is being able to disentangle the galaxy emission from that of the quasar. With combined observations from the Dark Energy Survey (DES), the VISTA Hemisphere Survey (VHS) and the UKIDSS Large Area Survey (ULAS), we exploit the quasar dust extinction in our sample to demonstrate that the quasar and galaxy emission can be separated via SED-fitting in these systems. By isolating the galaxy emission in this way, we estimate instantaneous SFRs for the galaxies in our sample, based on the restframe UV emission. In general, we find obscured quasars to reside in prodigiously star forming hosts with $25 \lesssim \mathrm{SFR_{UV}} \lesssim 365\ \mathrm{M_{\odot}yr^{-1}}$. Furthermore, we show that the most luminous quasars reside in the most actively star-forming galaxies, potentially indicating the same gas supply is fuelling both star formation and accretion on to the black hole.

Having isolated the galaxy emission via SED-fitting, we test our ability to model the restframe-UV emission of obscured z$\sim$2 quasar hosts in 2D. Until now, morphological studies of luminous quasar hosts have typically been limited to low redshifts or relied on space-based imaging. By making use of a multi-band modelling code however, we demonstrate that it is possible to accurately infer several galaxy properties (i.e. the position of the galaxy in the image, (X,Y), its radius, $\mathrm{R_{eff}}$, axis ratio, $\mathrm{q_{GAL}}$, angle of orientation, θ,

and Sérsic index, n), based on current ground-based imaging, accross the full range of galaxy and quasar luminosities considered in our sample. This potentially opens the door to future ground-based morphological studies of obscured quasars at high redshift.

At sub-mm wavelengths, thermal emission from cold dust peaks, meaning these wavelengths can be used to probe the dust heating by star formation, effectively giving a measure of the obscured star formation in the galaxy. Using targeted observations from SCUBA-2, we trace the 850μm emission in a sample of obscured quasars, finding evidence for prodigious star formation > 2400 $M_{\odot}yr^{-1}$ in three of the 19 quasars in our sample. The detection rate of our obscured quasar sample is found to be consistent with that of both more heavily-obscured Hot-DOGs and UV-luminous quasars, once the samples have been matched in luminosity and redshift. Furthermore, we find evidence that several of the obscured quasars lie in overdense regions of the sky (~ 3 times denser than sub-mm blank fields).

Declaration

I hereby declare that except where specific reference is made to the work of others, the contents of this dissertation are original and have not been submitted in whole or in part for consideration for any other degree or qualification in this, or any other university. This dissertation is my own work and contains nothing which is the outcome of work done in collaboration with others, except as specified in the text and Acknowledgements. This dissertation contains fewer than 60,000 words including appendices, bibliography, footnotes, tables and equations and has fewer than 150 figures.

CLARE WETHERS

JUNE 2018

Acknowledgements

First and foremost, I would like to express my sincere gratitude to my supervisors Manda and Paul, who have been a constant source of support and encouragement throughout my PhD. I am also grateful to Matt, whose enthusiasm and ideas have greatly contributed to this work and to the Science and Technology Facilities Council for funding my research.

To my office mates past and present - thank you for so graciously putting up with me every day and for helping me to de-bug my code on a regular basis. Thanks also to my house mates Dominika, Matt and Björn, without whom Cambridge would not be the same, and to my course mates for making my time at the IoA so enjoyable. Finally, I am eternally grateful to my good friend Conor for standing by me through thick and thin and to my family for their unwavering love and support.

CONTENTS

LIST OF FIGURES

LIST OF TABLES

CHAPTER 1

INTRODUCTION

1.1 THE DISCOVERY OF QUASARS

The discovery of quasars is arguably amongst the most ground-breaking astronomical findings of the last century. Their existence not only challenged what we thought possible in observational astronomy but also was the final nail in the coffin for the then popular steady state theory of our Universe. Their discovery is attributed to the CalTECH Astronomer Maarten Schmidt (Schmidt, 1963) when observing the radio source 3C 273. Initially this radio source was thought to be a nearby star due to its extreme brightness, but its spectrum revealed something far more unusual - the emission lines observed in 3C 273 were unlike any known star. Maarten Schmidt recognised these unusual emission lines as the Balmer series shifted in wavelength and thus concluded this object to lie at redshift z = 0.158, making it among the highest redshift observations of the time. The combination of being both very distant and incredibly bright led to a new classification of astronomical objects. Today, we recognise objects such as 3C 273 as quasars (derived from the term *quasi-stellar radio source*).

In the years following their discovery, many astronomers worked to characterise the nature of quasars, finding them to be a luminous class of Active Galactic Nuclei (AGN) powered by the accretion of matter onto a supermassive black hole (e.g. Lynden-Bell, 1969;

Lynden-Bell and Rees, 1971; Salpeter, 1964; Zel'dovich and Novikov, 1965). A major break-though came with the discovery that these exotic systems were not unusual at all, but rather were found to reside in numerous nearby galaxies (Kormendy et al. (1994) + references therein). This led to the idea that black holes potentially exist in the centre of a large proportion, if not all, galaxies and thus may play an important role in their evolution. Thanks largely to direct dynamical measurements, we now understand that supermassive black holes are commonplace in the centres of nearby, massive galaxies (Armitage and Natarajan, 2002; Kormendy and Richstone, 1995; Magorrian et al., 1998; Peterson and Wandel, 2000), but the nature by which they interact with their host galaxies remains an active area of research.

1.2 QUASAR - GALAXY CO-EVOLUTION

Since finding supermassive black holes to be common in galactic centres, astronomers have worked to directly link black hole activity to that of the surrounding galaxy. Observations in recent decades indicate a so-called 'coeval' scenario, in which AGN activity influences the surrounding galaxy, resulting in the simultaneous evolution of the AGN and its host.

1.2.1 M_{BH} AND THE GALACTIC BULGE

Perhaps the strongest evidence for such a 'coeval' scenario is the tight correlation between the black hole mass, M_{BH}, and the velocity dispersion of stars in the galactic bulge, σ_* (e.g. Ferrarese and Merritt, 2000; Gebhardt et al., 2000). Fig. 1.1 shows this relation for a range of different galaxies from spiral systems to ellipticals (Gültekin et al., 2009), with black hole masses derived from direct dynamical measurements compiled from Ferrarese and Ford (2005); Graham et al. (2008); Marconi and Hunt (2003); Tremaine et al. (2002). We note however, that galaxy models without a quantative measure of how well they fit the data (e.g. χ^2) and those appearing to provide a poor fit have been excluded from the galaxy sample in Fig. 1.1. As such, the selection biases of the Gültekin et al. (2009) sample likely tightens

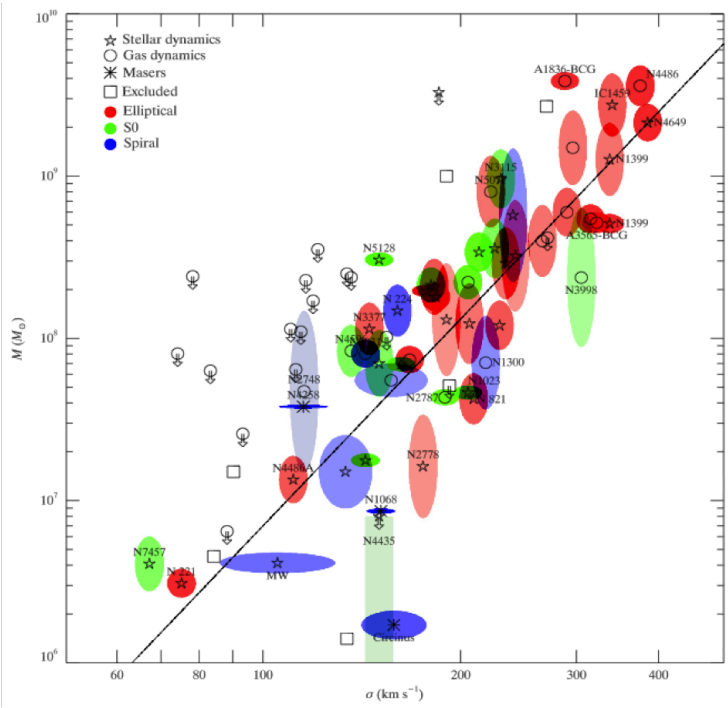

Fig. 1.1 Relation between M_{BH} and the velocity dispersion of stars in the bulge, based on a range of different galaxies. *Image credit:* Gültekin et al. (2009).

the relation observed in Fig. 1.1. Were the full sample to be included, the scatter in Fig. 1.1 would appear much larger.

In nearby galaxies, tight correlations have also been observed between M_{BH} and several other properties of the galactic bulge including the total bulge mass (Magorrian et al., 1998), the bulge luminosity (Faber and Jackson, 1976) and the stellar mass (Kormendy and Ho (2013) + references therein). These relations may appear counter-intuitive given the typical radius of a galactic bulge extends well beyond that of the sphere of influence of a black hole ($r_{\rm inf}$), where

$$r_{\rm inf} = \frac{GM_{\rm BH}}{\sigma^2}. \tag{1.1}$$

This apparent contradiction has long been an active area of research. Since the discovery that the AGN and its host appear linked (Magorrian et al., 1998), understanding the mechanisms by which AGN seemingly influence the outer regions of their host galaxies has been a topic of interest. To explain this phenomenon, one could imagine two extreme scenarios. In

the first instance, the apparent link between AGN and the galactic bulge is entirely driven by the bulge itself, i.e. there exists a regime in which the bulge properties dictate the amount of material available for accretion onto the BH, and therefore its size. At the other extreme, one could instead imagine the BH is entirely responsible for shaping its host. In this regime, dynamical interactions may be invoked to reach beyond the sphere of influence and shape the outer regions of the galaxy. Current thinking suggests the apparent relations between AGN and their hosts is due to some combination of these two extremes (e.g. Di Matteo et al., 2005).

One popular idea is that the amount of energy released as material spirals inward onto the BH is limited by the mass of the BH itself, M_{BH}. The limit on the amount of this energy that can be radiated as luminosity is known as the 'Eddington limit', L_{edd}, and is given by

$$L_{edd} = \frac{4\pi G M_{BH} m_p c}{\sigma_T} = 3 \times 10^4 \frac{M_{BH}}{M_\odot} L_\odot, \tag{1.2}$$

where G is the gravitational constant, m_p is the mass of a proton, c is the speed of light and σ_T is the Thomson cross section. L_{edd} denotes the luminosity at which the outward radiation pressure exceeds the gravitational force causing accretion onto the BH and is directly proportional to M_{BH}. When the accretion rate of the AGN exceeds that allowed by this limit, gas will be driven out of the central regions of the galaxy by radiation. It is this process of gas ejection which is thought to eventually stop the growth of the BH entirely. Simulations by Shankar et al. (2008); Sijacki et al. (2007) show the efficiency with which the AGN expels this gas to be reliant on both the gravitational potential of the bulge and the velocity dispersion of stars in this region, σ, meaning there is a strong interplay between the AGN and the galactic bulge (i.e. the bulge shapes BH accretion, which in turn shapes the bulge).

1.2.2 AGN FEEDBACK

Whilst the connection between galaxies and their black holes is now generally accepted (e.g. Gültekin et al., 2009; King, 2003; Peng et al., 2006), the exact nature of the feedback

processes driving their apparent co-evolution remains widely disputed. One key challenge lies in understanding the role of AGN in both fuelling (via positive feedback) and quenching (via negative feedback) star formation in the host galaxy.

The importance of negative AGN feedback is strongly supported by two key pieces of observational evidence. The first is found in the bright end of the galaxy luminosity function, where the number of bright galaxies is shown to decline more rapidly than models predict. Benson et al. (2003) demonstrate that this feature cannot be explained by cooling processes alone, rather additional feedback is required. The second major piece of evidence is the detection of X-ray cavities. The existence of these cavities (or 'bubbles') was first postulated in 1973 by Gull and Northover (1973), but they were not observed until some 20 years later (Böehringer et al., 1993). The X-ray cavities, made from relativistic plasma, are thought to form via AGN-driven jets (Fabian, 2012) and subsequently rise through the intra-cluster medium (ICM). As the cavities rise, they release vast amounts of thermal energy exceeding that lost via the cooling flows (Graham et al., 2008), thus quenching star formation.

More recently, the role of positive AGN feedback in triggering star formation has also been an active area of research. One mechanism for this triggering is given by Ishibashi and Fabian (2012), who suggest that dusty shells of gas are driven outwards from the central regions of the galaxy by radiation pressure. As these shells expand, it is thought that the surrounding cold gas is compressed, resulting in overdense regions of cool gas, which induces star formation in the shells. A recent study by Ishibashi and Fabian (2014) finds the rate of this induced star formation to increase with black hole mass, indicating the most massive black holes trigger the most star formation.

1.2.3 THE COSMIC EVOLUTION OF GALAXIES AND AGN

Further evidence for the co-evolution of black holes and their hosts can be seen in the similar evolution of galaxies and their AGN with redshift. AGN, for example, exhibit so-called *downsizing* behaviour in their luminosity, in which the number density of high-luminosity AGN peaks at a higher redshift compared to their lower-luminosity counterparts (e.g. Bongiorno et al., 2007). Aird et al. (2015) illustrate this trend among AGN populations

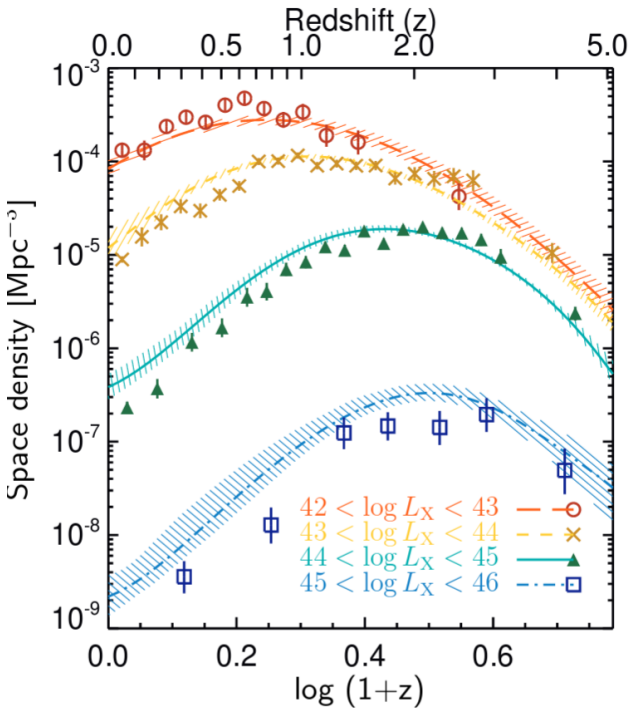

Fig. 1.2 Evolution of the space density of BHs as a function of redshift, given for a range of luminosities. *Image credit:* Madau and Dickinson (2014)

across a range of X-ray luminosities, L_X [1] (Fig. 1.2). Fig. 1.2 shows AGN with the highest X-ray luminosities ($L_X = 10^{45-47}$ergs^{-1}) to peak in number at z$\sim$2 compared to z$\sim$0.5 for those with low X-ray luminosities ($L_X = 10^{42-43}$ergs^{-1}). A similar trend is observed in the assembly of galaxies, with the most massive galaxies appearing to form at early cosmic times (e.g. Collins et al., 2009; Cowie et al., 1996). In this anti-hierachical picture, massive galaxies are thought to assemble the bulk of their stellar mass at high redshift, whilst lower mass systems are observed to form later. Although this idea seemingly contradicts the 'bottoms-up' structure formation predicted by ΛCDM cosmology in which small structures are the first to form (e.g. Bond et al., 1991; Lacey and Cole, 1993; White and Frenk, 1991), several studies have shown that invoking AGN feedback mechanisms can eliminate the need for this hierarchy by preferantially suppressing star formation in massive galaxies at low redshift (e.g. Bower et al., 2006; Croton et al., 2006; Kauffmann and Heckman, 2009; Scannapieco et al., 2005).

[1] $\log_{10}(L_{bol}) = (0.44 \pm 2.30) + (1.02 \pm 0.06) \times \log_{10}(L_X)$ (Grupe, 2004)

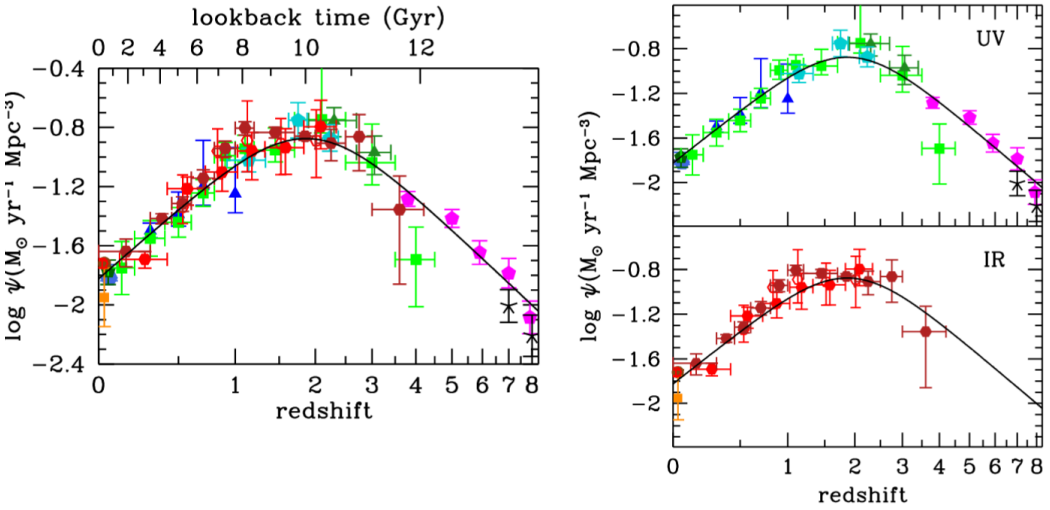

Fig. 1.3 The history of cosmic star formation based on FUV (*top right*), IR (*bottom right*) and combined FUV+IR (*left*) restframe measurements. *Image credit:* Aird et al. (2015) with data points from Miyaji et al. (2015).

Further to illustrating the *downsizing* behaviour of AGN, Fig 1.2 also demontrates AGN activity to peak at z$\sim$2 among the most luminous populations. This peak in AGN activity coincides with that of cosmic star formation, which is also shown to peak at z$\sim$2 (Fig. 1.3). Madau and Dickinson (2014) characterise the evolution of star formation across a general galaxy population, finding the star formation density, $\psi(z)$, to vary with reshift as

$$\psi(z) = 0.015\frac{(1+z)^{2.7}}{1+[(1+z)/2.9]^{5.6}}M_{\odot}year^{-1}Mpc^{-3}, \tag{1.3}$$

shown as solid black curves in Fig. 1.3. Studying populations of luminous AGN and their hosts during this peak of star formation and BH accretion is therefore key to understanding the apparent coevolution of galaxies and their AGN.

1.3 TRIGGERING AGN

The triggering of AGN themselves has proven somewhat controversial over recent decades. Whilst secular processes, such as minor mergers, bar instabilities and stochastic gas accretion appear sufficient in fuelling low- and moderate- luminosity AGN, more violent gas-rich major mergers (merging galaxies of comparable sizes) may be required to trigger the most luminous systems.

In cosmoligical simulations, major mergers are often invoked to model the formation of massive galaxies. Barnes and Hernquist (1991) for example, demonstrate that gas-rich mergers can result in rapid gas assembly in the central regions of the galaxy and trigger violent bursts of star formation, potentially offering an explanation for the existance of luminous IR galaxies. Hopkins et al. (2005, 2007) also demonstrate gas-rich mergers to trigger high rates of star formation and black hole accretion and suggest that the AGN will appear heavily obscured during bursts of star formation, before quasar-driven winds expel the remnant dust and gas from the galactic centre. The inclusion of these gas-rich mergers in simulations can reproduce several observations of quasars, including the quasar luminosity density out to z = 6 and the quasar luminosity function.

Observationally, the role of mergers in triggering AGN is more complicated, with strong variations across populations of high- and low- luminosity systems at different redshifts. Several independent studies of the last decade find little evidence that major mergers trigger quasars at low redshift. Cisternas et al. (2010) for example, find no difference in the merger fraction of moderate luminosity AGN at $0.3 < z < 1.0$ compared to inactive galaxies at similar redshifts. Furthermore, recent population synthesis modelling indicates that non-merger processes are likely to be the dominant trigger of AGN at $z < 1.5$ (Cisternas et al., 2010; Treister et al., 2012). At higher redshifts ($1.5 < z < 2.5$), this trend appears to continue among populations of low- and moderate- luminosity quasars, with Kocevski et al. (2011) also finding no difference between the merger rates of moderate-luminosity AGN and their galaxy control sample. Such studies suggest low- to moderate- luminosity AGN are no more likely to have undergone a recent major merger than an inactive galaxy at the same epoch.

The AGN merger fraction has however been shown to increase rapidly with AGN luminosity. Treister et al. (2011), for example, suggest major mergers trigger only the most luminous $\sim$10 per cent of AGN (or quasars), finding $\sim$90 per cent of AGN to show signs of merger activity at $L_{bol,AGN} \sim 10^{47} ergs^{-1}$ compared to $\sim$4 per cent at $L_{bol,AGN} \sim 10^{43} ergs^{-1}$. Whilst the need for major mergers in triggering the most luminous AGN has generally been accepted (e.g. Kocevski et al., 2011; Treister et al., 2012), there is conflicting evidence (e.g. Villforth et al., 2016). Morphological studies of AGN at z$\sim$0.7 by Villforth et al. (2014)

show no evidence for additional merger signatures (e.g. dynamical disruptions, asymmetries etc.) amongst their AGN sample. Instead, they find mergers to account only for a small fraction of AGN, even at the highest luminosities in their sample ($L_X \sim 10^{43.5}$ergs^{-1}).

1.4 DUST OBSCURATION

Another topic of debate over recent decades has been the cause of reddening in AGN. Reddening occurs when dust preferentially attenuates blue light from an astronomical object, causing it to appear redder in colour. In the case of AGN observations, several factors can contribute to this dust including the Milky Way galaxy, intervening galaxies along the line-of-sight, the AGN host galaxy and dust from the nuclear region (the obscuring medium within the central few kpc of the galaxy). The amount of reddening in a given system is often given as a colour excess, $E(B-V)$, but is also commonly quoted in terms of either the total V-band extinction, A_v, or the total extinction at a given wavelength, A_λ, where

$$A_v = R_v E(B-V) \tag{1.4}$$

and

$$A_\lambda = \frac{k(\lambda)A_v}{R_v}. \tag{1.5}$$

Observationally, the value of R_v has been shown to lie in the range $2 < R_v < 6$ with denser regions having a larger value of R_v (Cardelli et al., 1989), but conventionally a value of either R_v=3.1 or R_v=5.0 is selected (based on the diffuse ISM and dense molecular clouds respectively). The choice of extinction curve, $k(\lambda)$, for both the galaxy and the AGN makes little difference to the inferred extinction at long wavelengths ($\lambda_{\rm rest} \gtrsim 4000$Å), but can vary significantly at shorter wavelengths (Fig. 1.4). When modelling the extinction effects of interstellar dust (i.e. the galactic extinction) either an SMC, an LMC or a Milky Way extinction curve is typically assumed, the forms of which are shown in Fig. 1.4. Modelling the effects of circumnuclear dust obscuring the AGN however is somewhat less constrained

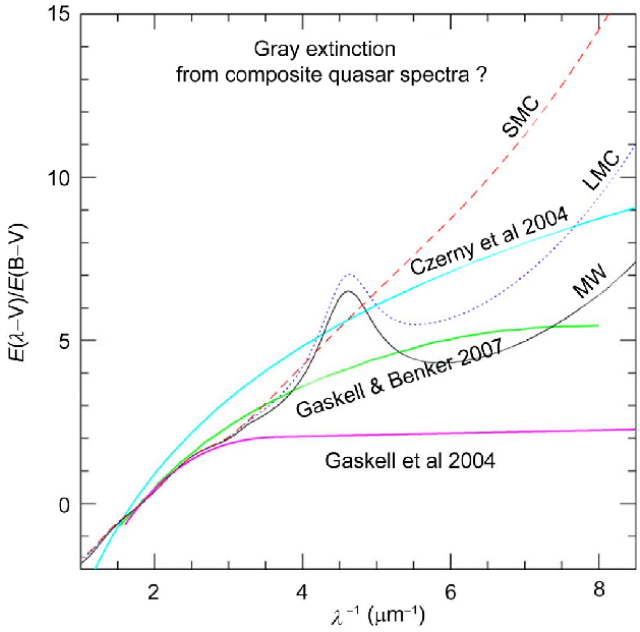

Fig. 1.4 Comparison of AGN extinction curves (Czerny et al., 2004; Gaskell et al., 2004) with SMC, LMC and MW extinctions. *Image credit:* Wang et al. (2014).

in terms of standard models. AGN extinction curves are typically derived empirically from either individual reddened AGN (e.g. Gaskell et al., 2004) or composite quasar spectra (e.g. Czerny et al., 2004; Gaskell et al., 2004). Two such examples are shown in Fig. 1.4 (Czerny et al., 2004; Gaskell et al., 2004), although many more are commonly used (e.g. Gallerani et al., 2010).

1.4.1 THE UNIFIED MODEL OF AGN

Generally speaking, AGN can be classified into two groups - Type I, in which both broad and narrow emission features are present (Seyfert 1s) and Type II, containing only narrow lines in their spectra (Seyfert 2s). Two scenarios intuitively explain the lack of observed broad emission features in Seyfert 2 galaxies; (i) Seyfert 2s do not contain broad emission features or (ii) their broad-line emission is being obscured by some medium. An early study from Rowan-Robinson (1977) finds that Seyfert 2 galaxies have excess dust extinction compared to Seyfert 1s, suggesting that dust surrounding the AGN core may be responsible for the observed differences between Type I and Type II AGN. Studies in the radio (e.g. Barthel, 1989) further reveal there to be very little difference between quasars and radio galaxies, both

morphologically and evolutionarily, with the vast majority of quasar models invoking radio beaming in some form, implying quasars and radio galaxies may also be linked, differing only in orientation with respect to the observer.

The idea of a unified model linking radio and Seyfert galaxies with the general AGN and quasar population has since been elaborated upon to produce the current paradigm (Fig. 1.5), in which the dust obscuration of AGN can be explained solely in terms of the orientation with regards to our line of sight (Antonucci, 1993). In this regime, AGN are surrounded by an optically-thick accretion disc. The emission arising from the infall of material onto this accretion disc can be characterised as a blackbody spectrum peaking at optical/ UV wavelengths (see Section. 1.5). Above and below the plane of the accretion disc exist optically-thick clouds, which give rise to the broad emission features observed in AGN spectra, leading to this inner region being referred to as the 'broad line region' (BLR). A so-called 'torus' - a region of clumpy, obscuring dust and gas - is thought to surround the BLR, lying co-planar to the accretion disc. Whilst the structure of this 'torus' remains an active area of research (e.g. Elitzur and Shlosman, 2006; Konigl and Kartje, 1994; Krolik and Begelman, 1988), it is generally modelled as a static doughnut-like structure, as illustrated in Fig. 1.5. Gas clouds further out from the AGN are thought to give rise to narrow line emission, forming the so-called narrow line region (NLR).

From Fig. 1.5, it can be seen that when an AGN is viewed completely edge-on (i.e. the line of sight passes directly through the torus structure), the dust from the torus completely obscures the broad emission lines arising from the inner regions closest to the AGN. Systems in this orientation - often referred to as Type-II AGN - therefore appear to contain only narrow line emission in their spectra arising from the more extended NLRs. If instead the AGN is viewed face-on (i.e. the plane of the torus lies perpendicular to the line of sight) - as in the case of Type I AGN - both the broad and narrow line emission are clearly visible along the line of sight. Intermediate AGN dust obscuration is then thought to arise when the system is orientated at an angle between these two extremes, where some fraction of the inner broad line region remains visible. Some of the most compelling evidence in favour of this model comes from spectropolarimetric observations of Type-II AGN, which reveal hidden

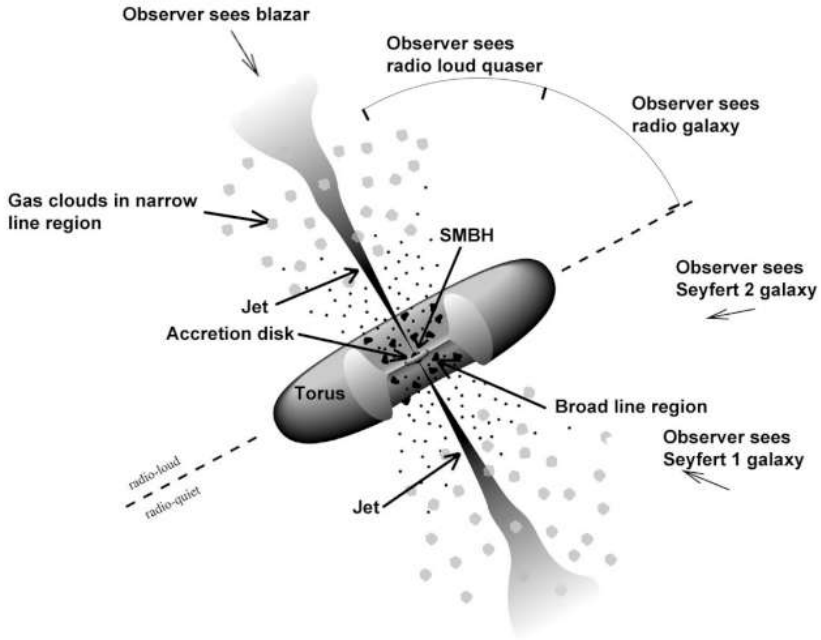

Fig. 1.5 Cartoon depiction of the unified AGN model postulated by Antonucci (1993). *Image credit:* Brian Koberlein

broad line emission in these systems (e.g. Tran, 2001). Through such observations, polarised (hidden) broad line regions (HBLRs) have been confirmed in a number of Seyfert 2 galaxies, with Tran (2001) finding HBLR galaxies to exhibit higher radio power relative to their IR emission than non-HBLR galaxies in the study. Despite these differences however, Tran (2001) find no difference in the level of dust obscuration in either class of galaxies, indicating that the orientation model of AGN cannot be applied to all Seyfert galaxies. Instead, a more complicated picture of AGN may be required to explain observations.

1.4.2 DUST AS A TRACER OF QUASAR EVOLUTION

For several decades, it has been suggested that the AGN paradigm is rather more complicated than the unified model postulated by Antonucci (1993). Along with the effects of orientation, dust reddening may also indicate the evolutionary phase of the AGN. Sanders et al. (1988) were among the first to put forward this idea, postulating that unlike moderate to low luminosity and low redshift systems, in which secular processes appear sufficient in fuelling the AGN, the most massive and luminous AGN are triggered by major mergers. Such mergers can drive vast amounts of gas towards the central regions of the merging galaxy and fuel both

the AGN and star formation, leading to starburst activity in the galaxy. As this star formation begins to decay, Sanders et al. (1988) suggest that the AGN expels the remnant dust and gas from the galaxy in a short-lived *blowout* phase, during which the AGN is thought to appear heavily obscured. Once the obscuring dust has been cleared from the central regions of the galaxy, the AGN is then thought to appear bright in the UV.

Studying the transitional phase between a starburst galaxy and UV-luminous AGN is therefore important in constraining the link (or lack thereof) between dust obscuration and AGN evolution. One way in which the above evolutionary picture can be tested is by looking at the connection between star formation and AGN luminosity. Sanders et al. (1988) suggest that AGN undergoing a *blowout* phase came about via massive mergers, meaning the same gas supply is likely fuelling both the AGN and the star formation in these transitional systems. If this is indeed the case, one would therefore expect to find more luminous AGN to reside in more actively star-forming galaxies. Whilst no such connection is found in either low-redshift or low- to moderate- luminosity AGN (e.g. Urrutia et al., 2012), several studies indicate the emergence of a trend among high-luminosity, high-redshift AGN (Chen et al., 2013; Rodighiero et al., 2010). Furthermore, this trend appears most prominent among populations of obscured AGN, supporting the evolutionary picture put forth by Sanders et al. (1988).

Another test of this evolutionary model is to search for evidence of a recent starburst in heavily obscured AGN. If, as Sanders et al. (1988) suggest, obscured AGN have recently undergone a starburst phase, one would expect to find heavily obscured AGN to reside in actively star forming hosts. Indeed, a recent study by Alaghband-Zadeh et al. (2016a) demonstrates the majority of luminous, obscured AGN are found in prodigiously star-forming galaxies at z$\sim$2, based on observations of their narrow Hα emission. If these system are very dusty however, it is likely that much of the star formation will appear obscured and therefore will not be fully accounted for in the Hα emission. Accurately measuring both the unobscured and obscured SFRs and their connection with AGN luminosity in luminous, reddened AGN hosts therefore remains an important test of evolutionary AGN models.

1.5 AGN SEDs

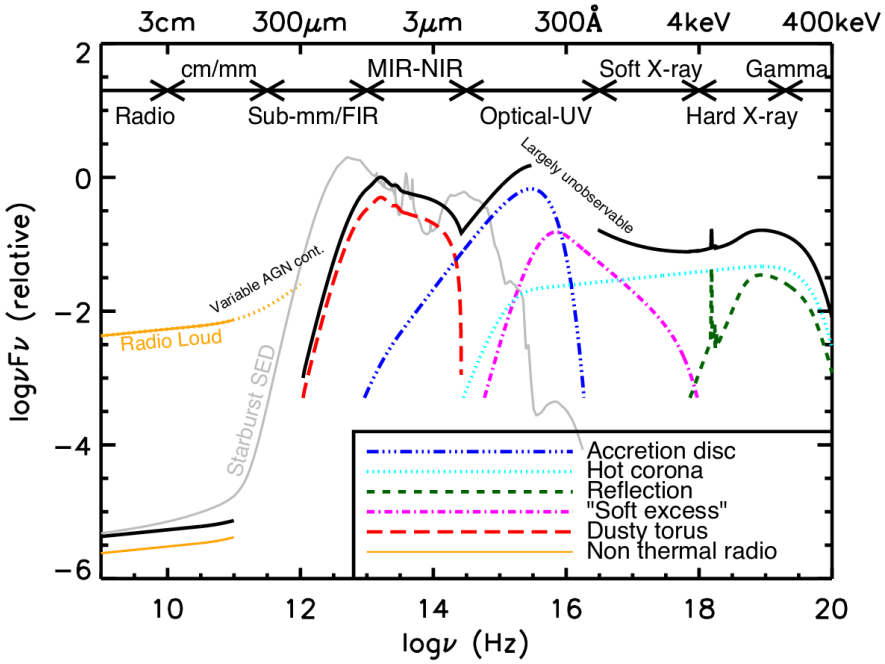

Fig. 1.6 AGN SED showing the predominant source of emission at in each region of the spectrum. *Image credit:* Christopher Harrison

A key property of AGN - one which has severely hindered AGN host galaxy studies - is their strong continuum emission across many regions of the electromagnetic spectrum (Fig. 1.6). The brightest AGN, or quasars, typically dominate the spectrum by several orders of magnitude compared to the light emitted from their host galaxies, particularly at UV/ optical wavelengths, where AGN emission peaks. Assuming the accretion disc plasma to be optically thick and thermal, one would expect it to appear as a superposition of blackbody emission with a range of temperatures. If the BH is accreting close to L_{EDD} (see Eqn. 1.2), the temperature of the blackbody emission from the disc will result in the radiation peaking in the UV when considering the size scales of SMBHs. Indeed, this peak in continuum emission forms a key feature in AGN spectra (Fig. 1.6) and is often referred to as the 'big blue bump'. Many studies have studied this feature in great depth (e.g. Kolykhalov and Sunyaev, 1984; Shields, 1978) and conclude the 'big blue bump' to arise from the thermal emission of gas in the accretion disc.

A secondary peak in the AGN spectrum occurs in the IR (Fig. 1.6). Emission in this region is dominated by thermal emission from dust heated by the AGN, with the location of the peak depending on the temperature of the dust. This thermal emission process arises from the absorption and re-emission of high-energy photons by dust in the torus. Whilst the geometry of the torus remains an active area of research, it is generally believed to be clumpy in structure and contain clouds of dust rather than a smooth disc. These clouds of dust absorb photons from the accretion disc, causing the dust to heat up. The absorbed photons consequently loose energy and are thermally re-emmited at longer wavelengths, giving rise to IR emission. Although the exact form of the resultant IR emission varies for each source, it is typically characterised by a broken power law $\lesssim 40$ μm with a steep drop off $\gtrsim 40$ μm (e.g. Mullaney et al., 2011), peaking at $\lambda \sim$ 20-50 μm.

At sub-mm wavelengths, thermal emission from dust heated by the AGN continues to contribute at $<100\mu$m. At longer wavelengths, thermal emission from cooler dust begins to contribute, with dust further from the AGN and dust heated by star formation dominating the sub-mm emission at $>100\mu$m. Dust heated by star formation peaks at $\sim$1mm (shown by the starburst SED in Fig. 1.6), meaning several studies have relied on sub-mm observations to characterise the star formation in quasar host galaxies (e.g. Jones et al., 2015, 2014; Priddey et al., 2003).

Many studies of the last decade have made use of *Herschel* observations at these longer wavelengths to explore the connection between AGN and their hosts. Stanley et al. (2015) for example calculate the SFRs for a sample of luminous ($L_{bol} \sim 10^{48} ergs^{-1}$) AGN at $0.2 < z < 2.5$, finding a weak trend between AGN luminosity and SFR. Another study by Harris et al. (2016) finds a similar trend between SFR and both AGN luminosity and black hole mass out to SFR$\sim 600 M_{\odot} yr^{-1}$ at $2 < z < 3$ - a limit which Harris et al. (2016) suggest may be due to the saturation of the starburst by supernova winds. Pitchford et al. (2016) however, find no such relation in their sample of $2.15 < z < 3.5$ AGN, although the derived SFRs generally lie above the $600 M_{\odot} yr^{-1}$ limit above which Harris et al. (2016) also find no correlation. Studies at FIR/ sub-mm such as these rely heavily on separating the dust heating via star formation from that of AGN - something which can often prove problematic.

A common assumption is that sub-mm emission is dominated by heating via star formation, with very little contribution from the AGN, but this has been widely debated in the literature. Symeonidis et al. (2016) for example find that AGN heating alone can account for the FIR/ sub-mm emission. Furthermore, Symeonidis and Page (2018) conclude that the fraction of of AGN dominated sources increases with the total FIR luminosity, suggesting the majority of bright IR galaxies are shaped by the AGN rather than star formation. Among galaxies with $L_{IR} > 10^{13.5}$ at $1 < z < 2$, Symeonidis and Page (2018) find that the AGN can account for the entire IR emission. This contamination by AGN heating can lead to the overestimate of the SFR in AGN hosts, particularly among very luminous systems. At longer sub-mm wavelengths, synchrotron radiation from the AGN can also contribute to the emission, again leading to the overestimate of the star formation in the host if this feature is not properly accounted for.

1.6 THESIS OUTLINE

This thesis aims to characterise the host galaxies of luminous, reddened quasars at $z\sim2$ across multiple wavelengths. Particular focus is placed on the star formation, morphologies and environments of these systems in the context of galaxy evolution. The thesis is structured as follows:

Chapter 2 investigates the UV star-forming properties of luminous, reddened quasar host galaxies in DES. Here we perform the first population study of luminous quasar hosts at $1.4 < z < 2.7$ in the rest-frame UV, exploiting the dust reddening of the quasar to directly study emission from the galaxy. Through SED fitting, we derive star formation rate estimates for the host galaxy sample and study the link between these rates and the intrinsic luminosity of the quasar.

Chapter 3 makes use of the third year of DES observations to map the star-forming regions of our quasar host sample in 2D, based on their emission in the rest-frame UV. This chapter predominantly tests our ability to do this mapping with the existing data, outlining the limitations of the fitting method on current observations. From the results, we infer basic

structural properties for luminous quasar host galaxies at $1.4 < z < 2.7$, placing constraints on the spatial extent of the star formation measured in Chapter 2.

Chapter 4 explores the sub-mm properties of reddened quasars at $1.4 < z < 2.7$. Using brand new 850μm targeted observations from SCUBA-2, we analyse the SFRs and environments of 19 reddened quasars lying in the Northern hemisphere. The sub-mm properties of our sample are directly compared to those of quasars with higher and lower dust content, allowing us to place our sample in the broad context of the general quasar population.

Throughout this thesis, we assume a flat ΛCDM cosmology with $H_0 = 70 \mathrm{kms}^{-1}\mathrm{Mpc}^{-1}$, $\Omega_M = 0.3$ and $\Omega_\Lambda = 0.7$. All quoted magnitudes are based on the AB system, which is the native magnitude system for the optical data used in this work. In cases where these magnitudes have been converted from the Vega system (e.g. in IR surveys), the conversion is specified.

CHAPTER 2

REDDENED QUASAR HOSTS IN THE UV

2.1 INTRODUCTION

Quasars typically outshine their host galaxies by several orders of magnitude, particularly in the rest-frame UV where the quasar continuum peaks. This has significantly limited studies of quasar host galaxies at these wavelengths, requiring high spatial resolution to separate the point-like quasar light from the more extended host galaxy emission. Such a limitation has largely confined studies of quasar hosts to relatively low redshift ($z < 1$), where good spatial resolution is much easier to achieve (e.g. Dunlop et al., 2003; Matsuoka et al., 2015). At these low redshifts, host galaxy emission has been separated from that of the quasar via both image (e.g. Jahnke et al., 2004; Sánchez et al., 2014) and spectral decomposition (e.g. Matsuoka et al., 2015; Vanden Berk et al., 2006), with these studies finding a strong correlation between M_{BH} and M_{bulge}. However there appears to be no correlation between the quasar accretion rate and star formation rate (SFR) of the host at these low redshifts (e.g. Urrutia et al., 2012).

At higher redshifts ($z \sim 2$) - the epoch at which BH activity peaks - a handful of studies have used high-resolution spaced-based imaging from the *Hubble Space Telescope (HST)* to spatially isolate the host galaxy emission, although these studies have largely targeted

moderate-luminosity quasars ($L_{bol,QSO} \sim 10^{43-44} ergs^{-1}$), where emission from the galaxy makes up a significant fraction of the flux in the rest-frame UV/ optical (e.g. Jahnke et al., 2004). In these moderate-luminosity quasars, Jahnke et al. (2004) find no dependence of the SFR on the quasar luminosity, deriving SFRs $\sim 6\,M_{\odot} yr^{-1}$ (prior to dust correction) across their entire quasar sample. To analyse the hosts of more luminous quasars, studies have primarily relied on observations at longer wavelengths in the far infra-red (FIR) to millimetre regime, where the host galaxy emission peaks (e.g. Harris et al., 2016; Priddey et al., 2003). Unlike their low-redshift and lower-luminosity counterparts, the SFRs of high-luminosity quasars at $z \gtrsim 2$ have been shown to correlate with $L_{bol,QSO}$, with several studies finding more luminous quasars to reside in more actively star-forming hosts (e.g. Coppin et al., 2008; Delvecchio et al., 2015; Harris et al., 2016; Hatziminaoglou et al., 2010; Rosario et al., 2013; Xu et al., 2015).

Several studies have also attempted to probe these luminous, high-redshift quasar hosts in the rest-frame optical to near infra-red (NIR), making use of emission at rest-frame wavelengths of $\sim 1 \mu m$, where the fraction of galaxy-to-quasar emission is larger than in the rest-frame UV (e.g. Kukula et al., 2001; Ridgway et al., 2001). Even in this wavelength regime, however, these studies have typically required high-resolution space-based imaging from *HST* in order to accurately subtract the quasar point spread function (PSF) from the galaxy emission - a problem which remains challenging (e.g. Mechtley et al., 2016). The majority of these studies find an enhanced merger fraction in populations of high-luminosity quasars, although this conclusion remains disputed (e.g. Villforth et al., 2016).

An alternative approach to observing quasar hosts at optical/ NIR wavelengths is to exploit dust obscuration along the quasar line-of-sight, which can heavily redden the quasar continuum and enhance the fractional flux contribution of the galaxy at these wavelengths (e.g. Fan et al., 2016; Glikman et al., 2015; Urrutia et al., 2008, 2012). This approach has also been used to study quasar hosts in the rest-frame UV, but the rare nature of these heavily-reddened quasars has limited high-redshift studies to individual objects (e.g. Cai et al., 2014). These high-redshift, dust-obscured quasars may provide key insights into the connection between quasars and their hosts, with Sanders et al. (1988) suggesting that a

connection between $L_{bol,QSO}$ and SFR may be more prominent among these dusty systems than among un-obscured quasars.

In this chapter, we explore the star-forming properties of luminous, yet heavily reddened (A_v ∼2-6) quasars at z∼2, exploiting dust obscuration to directly study the host galaxies in the rest-frame UV. Using an SED fitting routine, we separate galaxy emission from that of the quasar, allowing the SFR of the host to be inferred. Our derived SFRs are compared to rates measured from independent studies of these quasars and investigate the potential link between these rates and quasar luminosity. Throughout this chapter, the following conversions have been applied to convert the Vega magnitudes of UKIDSS and VISTA to the AB system;

$J_{UKIDSS,AB}=J_{UKIDSS,Vega}+0.938$; $J_{VISTA,AB}=J_{VISTA,Vega}+0.937$;

$H_{UKIDSS,AB}=H_{UKIDSS,Vega}+1.379$; $H_{VISTA,AB}=H_{VISTA,Vega}+1.384$;

$K_{UKIDSS,AB}=K_{UKIDSS,Vega}+1.900$; $K_{SVISTA,AB}=K_{SVISTA,Vega}+1.839$.

2.2 DATA

The reddened quasars considered throughout this chapter lie at redshifts $1.5 < z < 2.7$. The sample selection criteria is outlined in detail in Banerji et al. (2015a, 2012), but the basic criteria and the new imaging data are described below.

2.2.1 NIR SELECTION OF LUMINOUS REDDENED QUASARS

Red quasar candidates were identified using NIR imaging from wide-field surveys such as the UKIDSS Large Area Survey (ULAS) and VISTA Hemisphere Survey (VHS), as detailed in Banerji et al. (2015a, 2012). Objects that appeared as point-sources in the *K*-band, with $K_{AB} < 18.4$[1], formed the flux-limited base sample. This point-source restriction was applied to ensure that the *K*-band light is dominated by an unresolved object, therefore excluding galaxies and isolating high-redshift, NIR-luminous quasars. Targets were further required to possess extremely red NIR colours, $(J\text{-}K)_{AB} > 1.5$ (corresponding to an $E(B\text{-}V) \gtrsim 0.5$ at $z \sim 2$,

[1]Magnitudes were calculated within a 2 arcsecond diameter aperture (*apermag3*) and include an aperture correction appropriate for point sources.

for a typical quasar SED). The morphological cut applied to the *K*-band ensures the host galaxy emission is subdominant in the NIR, meaning these red NIR colours can be attributed to dust reddening rather than starlight in the galaxy. Finally, a WISE colour cut (W1-W2 $>$ $0.85_{\rm Vega}$) was applied to separate quasars from stars. Of the 66 targets selected in this manner, 61 were successfully followed up with either SINFONI VLT or Gemini-GNIRS observations (Banerji et al., 2015a, 2012, 2013). 38 of these were spectroscopically-confirmed to be Type-1 broad-line (BL) quasars at $1.5 < z < 2.7$ and form the parent spectroscopic sample of heavily reddened quasars in this thesis. With extinction-corrected bolometric luminosities of $L_{\rm bol,QSO} \sim 10^{47} {\rm ergs}^{-1}$ and $M_{\rm BH} \sim 10^{9-10}$ $M_{\odot}$ (Banerji et al., 2015a), these quasars are among the most luminous and massive accreting SMBHs known at this epoch.

Detecting even the most luminous, star-forming quasar host galaxies at z $\sim$ 2 requires deep optical imaging data. The most UV-luminous, star-forming galaxies at $z \sim 2$ currently known have typical *r*-band magnitudes fainter than $\sim$22 (AB) (e.g. Reddy et al. 2008). These magnitudes lie below the flux limit of wide-field optical imaging surveys such as the Sloan Digital Sky Survey (SDSS), which, until recently was the deepest optical imaging survey available over the $>$ 1000 deg^2 area overlapping the VHS and ULAS survey footprints.

2.2.2 REDDENED QUASARS IN THE DARK ENERGY SURVEY (DES)

We make use of new deep optical photometry for the reddened quasars from observations conducted as part of the Dark Energy Survey (DES). DES is a wide-field survey, imaging 5000 deg^2 of the southern celestial hemisphere in the *grizY*-bands (Abbott et al., 2016; Flaugher et al., 2015; Frieman et al., 2013). The 5-year survey began in 2013 and uses the 570 Megapixel DECam on the 4m Blanco telescope at the Cerro Tololo Inter-American Observatory (CTIO). DES is among the deepest wide-field surveys currently in operation and will eventually reach depths of $i \lesssim 24.0$ (10σ; AB) for extended sources.

The work detailed in this chapter is based on observations conducted during the first year of DES operations (2013 Aug - 2014 Feb) corresponding to the Year 1 Annual 1 (Y1A1) internal data release (Diehl et al., 2014). Sixteen of the 38 reddened quasars in our spectroscopic sample overlap with the DES Y1A1 footprint, which covers $\sim$1800 deg^2.

Table 2.1 The effective wavelengths ($\lambda_{\rm eff}$) and 10σ limiting magnitudes reached by the Y1A1 data in a 2 arcsec diameter aperture.

Filter	$\lambda_{\rm eff}$ (Å)	Magnitude Limit (10σ; AB)
g	4824	23.4
r	6432	23.2
i	7806	22.5
z	9179	21.8
Y	9883	20.1

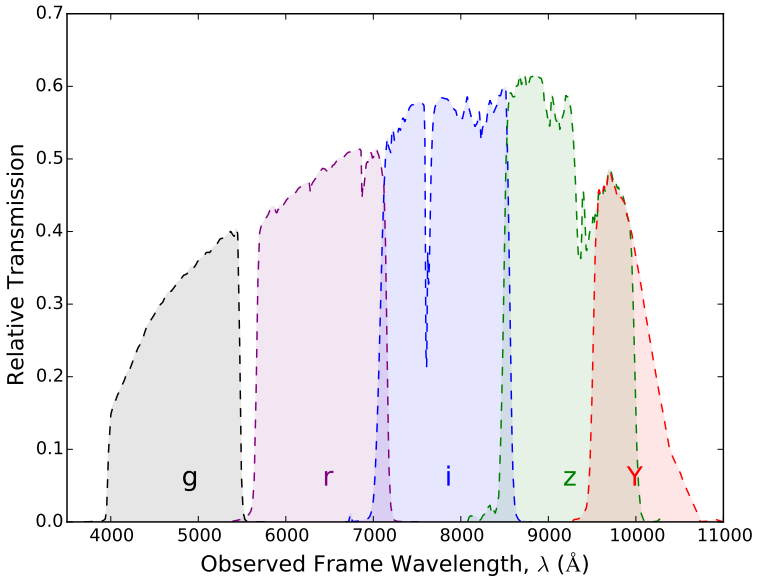

Fig. 2.1 Transmission curves fo each of the DES *grizY* filters.

The 10σ limiting magnitudes reached by the Y1A1 data in a 2 arcsec diameter aperture are summarised in Table 2.1, where the effective wavelength, $\lambda_{\rm eff}$ each passband is given by Equation 2.1 (Tokunaga and Vacca, 2005). The transmission of each of the DES filters is given in Fig. 2.1.

$$\lambda_{\rm eff} = \sqrt{\frac{\int \lambda S(\lambda) d\lambda}{\int S(\lambda) \frac{d\lambda}{\lambda}}}, \tag{2.1}$$

where $S(\lambda)$ denotes the filter transmission function.

For a single quasar, ULASJ1002+0137, in the COSMOS field, we also make use of DECam observations conducted as part of the Science Verification. This data goes considerably deeper than the Y1A1 data, reaching an i-band magnitude limit of 25.1 in a 2 arcsec aperture

Table 2.2 Summary of the reddened quasar sample considered in this work. M_{BH} and z are derived from the VLT spectral follow-up observations presented in Banerji et al. (2015a, 2012). Values of $L_{bol,QSO}$ have been calculated based on the results of this paper.

Name	RA	DEC	z	$\log_{10}(L_{bol,QSO})$ (erg s^{-1} ($L_\odot$))	$\log_{10}$ ($M_{BH}/M_\odot$)
ULASJ0016-0038	4.0025	-0.6498	2.194	46.54 (12.95)	9.3
ULASJ1002+0137	150.5470	1.6185	1.595	46.51 (12.92)	10.1
VHSJ2024-5623	306.1074	-56.3898	2.282	46.63 (13.05)	9.8
VHSJ2028-5740	307.2092	-57.6681	2.121	47.66 (14.08)	10.1
VHSJ2100-5820	315.1403	-58.3354	2.360	47.08 (13.50)	9.1
VHSJ2115-5913	318.8817	-59.2188	2.115	47.49 (13.91)	9.3
ULASJ2200+0056	330.1036	0.9346	2.541	47.34 (13.76)	9.2
VHSJ2220-5618	335.1398	-56.3106	2.220	47.87 (14.28)	9.9
ULASJ2224-0015	336.0392	-0.2566	2.223	46.87 (13.28)	8.9
VHSJ2227-5203	336.9491	-52.0582	2.656	46.87 (13.29)	10.0
VHSJ2235-5750	338.9331	-57.8371	2.246	47.13 (13.55)	10.1
VHSJ2256-4800	344.1443	-48.0088	2.250	47.43 (13.85)	10.1
VHSJ2257-4700	344.2589	-47.0156	2.156	46.60 (13.02)	9.5
VHSJ2306-5447	346.5010	-54.7882	2.372	46.90 (13.32)	10.0
ULASJ2315+0143	348.9842	1.7307	2.560	48.06 (14.48)	8.8
VHSJ2332-5240	353.0387	-52.6780	2.450	46.78 (13.19)	9.5
VHSJ2355-0011	358.9394	-0.1893	2.531	47.34 (13.75)	10.1

(10σ; AB). We note however, that the optical magnitudes of ULASJ1002+0137 are such that it would also be detected with the Y1A1 depths, had this region been part of the Y1A1 footprint. The sample considered in this work therefore consists of 17 spectroscopically-confirmed reddened quasars at $1.5 < z < 2.7$, with an average black hole mass, $M_{BH} \sim 10^{9.8} M_\odot yr^{-1}$ and bolometric luminosity, $L_{bol} \sim 10^{47} ergs^{-1}$ - representative of the parent sample of 38 reddened quasars in Banerji et al. (2015a, 2012) in terms of redshift, BH mass and luminosity ($M_{BH} \sim 10^9$-$10^9 M_\odot yr^{-1}$; $L_{bol} \sim 10^{47} ergs^{-1}$). The DECam *grizY* band observations for the sample are summarised in Table 2.2, with the corresponding *gri*-band colour composite images given in Fig. 2.2.

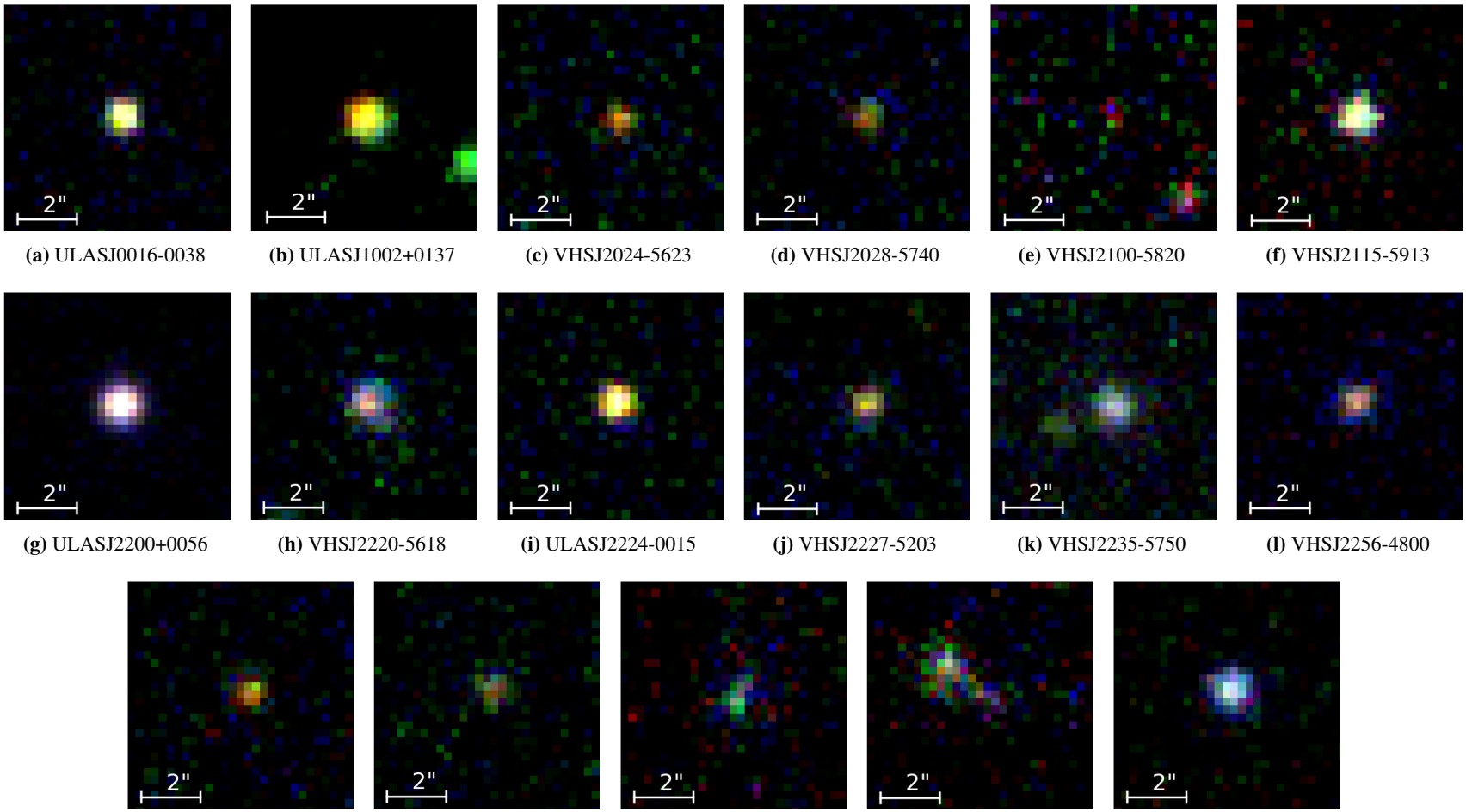

(a) ULASJ0016-0038 **(b)** ULASJ1002+0137 **(c)** VHSJ2024-5623 **(d)** VHSJ2028-5740 **(e)** VHSJ2100-5820 **(f)** VHSJ2115-5913

(g) ULASJ2200+0056 **(h)** VHSJ2220-5618 **(i)** ULASJ2224-0015 **(j)** VHSJ2227-5203 **(k)** VHSJ2235-5750 **(l)** VHSJ2256-4800

(m) VHSJ2257-4700 **(n)** VHSJ2306-5447 **(o)** ULASJ2315+0143 **(p)** VHSJ2332-5240 **(q)** VHSJ2355-0011

Fig. 2.2 Composite DES colour images, *g* (blue), *r* (green), *i* (red), for the quasar sample.

At redshifts $1.5 < z < 2.7$, the DES filters trace emission at rest-frame UV wavelengths ($\lambda_{\rm rest}$ ∼1300 - 3800 Å). We use the DES MAG_AUTO SExtractor magnitudes for our sources, which have been shown to perform best in SED-fitting of galaxies with the DES data (e.g. Sánchez et al. 2014). The MAG_AUTO magnitudes are preferred to the DES model magnitudes as the model magnitudes assume an exponential disk model, which may not be appropriate for our high-redshift galaxies. We note however, that differences between the model and MAG_AUTO magnitudes are typically small and our choice of magnitudes therefore does not affect the main conclusions of this study. The MAG_AUTO magnitudes do however underestimate the fluxes of point sources, as no aperture correction is applied. Indeed, Reed et al. (2017) find that for point sources in DES Y1A1, the MAG_AUTO values are systematically fainter by ∼0.1 mag compared to the MAG_PSF values. Although our quasars are mostly extended in the DES *griz*-bands, they are often unresolved in the DES *Y*-band, where the MAG_AUTO values are ∼0.1 mags fainter than the MAG_PSF values. Once again, we find these magnitude variations to have a negligible effect on the results of this study. The DES MAG_AUTO magnitudes for all 17 sources are presented in Table 2.3. All photometry has been corrected for any spatial non-uniformity in the global calibration and for the effects of Galactic extinction using the stellar locus regression technique described in Drlica-Wagner et al. (2017). Sixteen of the 17 quasars in our sample are detected at $\geq 10\sigma$ in at least one of the *gri* DES bands.

The DES MAG_AUTO values in the *g*-band presented in Table 2.3 are typically one magnitude brighter than predicted from the SED fitting in Banerji et al. (2015a, 2012) ($g_{\rm QSO,SED}$). Assuming the reddening towards the quasar sight line calculated from modelling the NIR photometry (Banerji et al., 2015a, 2012), we derive *g*-band magnitudes >1.0 mag fainter than the DES MAG_AUTO magnitudes for 15 of the 17 quasars. This suggests that the DECam images are detecting some source of excess emission in the rest-frame UV that cannot be accounted for by a reddened quasar template.

Table 2.3 DES MAG_AUTO magnitudes for the reddened quasar sample. All magnitudes are on the AB system and have been corrected for the Stellar Locus Regression (SLR) offsets in the *g,r,i* and *z*-bands. $g_{\rm QSO,SED}$ denotes the predicted *g*-band magnitude, based on the SED fits to the NIR photometry alone (Banerji et al., 2015a, 2012).

Name	$g_{\rm QSO,SED}$	$g_{\rm auto}$	$g_{\rm QSO,SED} - g_{\rm auto}$	$r_{\rm auto}$	$i_{\rm auto}$	$z_{\rm auto}$	$Y_{\rm auto}$
ULASJ0016-0038	24.36	23.16 ±0.08	1.20	21.80 ±0.04	21.19 ±0.04	-	20.43 ±0.10
ULASJ1002+0137	28.14	23.55 ±0.05	4.59	23.01 ±0.03	22.14 ±0.02	21.36 ±0.02	21.06 ±0.04
VHSJ2024-5623	25.34	24.81 ±0.37	0.53	23.68 ±0.16	22.34 ±0.07	21.63 ±0.07	21.69 ±0.23
VHSJ2028-5740	29.19	24.15 ±0.24	5.04	23.32 ±0.12	22.45 ±0.08	21.61 ±0.08	21.37 ±0.26
VHSJ2100-5820	26.95	25.37 ±0.49	1.58	24.51 ±0.39	23.56 ±0.21	22.17 ±0.13	22.37 ±0.68
VHSJ2115-5913	27.61	22.52 ±0.05	5.09	22.28 ±0.08	21.90 ±0.09	21.14 ±0.11	21.37 ±0.50
ULASJ2200+0056	23.70	22.03 ±0.03	1.67	21.36 ±0.02	20.71 ±0.02	19.90 ±0.01	19.60 ±0.04
VHSJ2220-5618	24.99	23.24 ±0.06	1.75	22.63 ±0.06	21.72 ±0.04	20.53 ±0.03	20.04 ±0.05
ULASJ2224-0015	24.78	23.65 ±0.10	1.13	22.82 ±0.06	21.77 ±0.04	20.89 ±0.03	21.03 ±0.11
VHSJ2227-5203	28.59	23.88 ±0.16	4.71	23.22 ±0.08	22.45 ±0.05	21.35 ±0.05	21.56 ±0.18
VHSJ2235-5750	24.44	23.20 ±0.09	1.24	22.71 ±0.07	21.82 ±0.05	21.05 ±0.04	20.74 ±0.09
VHSJ2256-4800	24.27	22.76 ±0.07	1.51	22.55 ±0.05	22.20 ±0.08	21.32 ±0.05	20.90 ±0.15
VHSJ2257-4700	25.88	25.57 ±0.46	0.31	23.83 ±0.14	22.48 ±0.07	21.57 ±0.07	21.43 ±0.26
VHSJ2306-5447	25.87	24.07 ±0.12	1.80	23.90 ±0.16	22.66 ±0.08	21.69 ±0.06	21.75 ±0.34
ULASJ2315+0143	30.55	22.70 ±0.08	7.85	22.46 ±0.10	22.47 ±0.20	21.94 ±0.19	-
VHSJ2332-5240	25.78	23.49 ±0.10	2.29	23.49 ±0.14	23.01 ±0.15	22.27 ±0.14	22.54 ±0.82
VHSJ2355-0011	25.98	22.43 ±0.03	3.55	22.51 ±0.06	22.18 ±0.06	21.64 ±0.06	21.41 ±0.19

To quantify whether the excess emission in the g-band photometry (Table 2.3) extends beyond the local PSF, we use the MODEST star-galaxy classifier (Drlica-Wagner et al., 2017), based on the SPREAD_MODEL quantity from SExtractor. SPREAD_MODEL is defined to be a normalised linear discriminant between the best-fit local PSF-model and a more extended, exponential disk model convolved with the PSF (Desai et al., 2012). The MODEST classifier takes account of the value of SPREAD_MODEL and its associated error in each band. MODEST has been optimised for the selection of a high-purity galaxy sample in DES by comparing to classifications from both deep space-based (*HST*) and high-quality ground-based (CFHTLens) surveys. The contamination rate from stars is estimated to be < 5 per cent for $i < 22.5$ (Drlica-Wagner et al., 2017). MODEST classifications for the full sample are given in Table 2.4, where a MODEST classification of 0 denotes an unphysical PSF fit (likely star) while 1 indicates a high-confidence galaxy, 2 indicates a high-confidence star and 3 denotes an ambiguous classification. A detailed morphological analysis is beyond the scope of the investigation presented in this chapter. Instead, we simply seek to discriminate between point-like sources and extended images, which could indicate the detection of the host galaxy.

Ten of the 17 reddened quasars in our sample are morphologically classified as high-confidence galaxies in the DES g-band, with a further two having an ambiguous classification and therefore also consistent with being spatially extended. This number of high-confidence galaxies increases to 12 in the r-band, representing 70 per cent of our sample. Even in the redder DES bands, 9 (7) of the quasars are classified as being extended beyond the local PSF in the i- (z-)bands. Quasar emission is spatially unresolved, yet the MODEST classifications in Table 2.4 indicate a significant fraction of our quasar sample to be spatially resolved in the DES ground-based imaging. Moreover, this fraction of extended sources increases at bluer wavelengths. Investigating the reason for the spatial extension and the excess rest-frame UV emission seen from these quasars in the DES data forms the central aim of this chapter.

Table 2.4 MODEST star-galaxy classifiers for the quasar sample, where 0 = unphysical PSF fit (likely star), 1 = high confidence galaxy, 2 = high confidence star and 3 = ambiguous.

Name	$\texttt{MODEST}_g$	$\texttt{MODEST}_r$	$\texttt{MODEST}_i$	$\texttt{MODEST}_z$
ULASJ0016-0038	2	2	2	1
ULASJ1002+0137	1	1	1	3
VHSJ2024-5623	1	1	3	3
VHSJ2028-5740	1	1	1	3
VHSJ2100-5820	1	1	1	1
VHSJ2115-5913	1	1	1	3
ULASJ2200+0056	2	2	2	2
VHSJ2220-5618	1	1	1	1
ULASJ2224-0015	0	2	2	2
VHSJ2227-5203	3	2	3	0
VHSJ2235-5750	2	1	1	3
VHSJ2256-4800	1	1	3	3
VHSJ2257-4700	0	3	3	2
VHSJ2306-5447	1	1	1	3
ULASJ2315+0143	1	1	1	1
VHSJ2332-5240	1	1	0	2
VHSJ2355-0011	3	1	1	2

2.3 SPECTRAL ENERGY DISTRIBUTION (SED) FITTING

To characterise the nature of the rest-frame UV emission seen in the DECam images, we fit SED models to the DES *grizY* and the ULAS/VHS NIR *JHK* photometry for each source. We thus determine a model SED spanning rest-frame UV through optical wavelengths (approximately 1400-7000 Å) for each of the reddened quasars in our sample. In cases where the photometric errors are $<$ 10 per cent of the observed flux, an error floor of 10 per cent is applied prior to the SED-fitting to mitigate against the effect of any systematic uncertainties in the photometry and quasar variability (Section 2.4.3). This floor has been selected to represent the scatter in unreddened quasar SEDs over the rest-frame wavelength interval $1200-10\,000$ Å . Although the parametric quasar model used in this work (Section 2.3.1) is found empirically to reproduce the broad-band colours (*ugrizYJHK*) of unreddened quasars [2] (Schneider et al., 2010), not all quasar SEDs look exactly the same, rather there appears to be a scatter $\sim$ 10 per cent. The effectiveness of the parametric model at reproducing the

[2]The quasar model reproduces broad-band quasar colours to $\sigma \simeq 0.1$ mag, based on quasars at $0.2 < z < 4.0$ with $m_i < 19.1$ from the SDSS DR7 quasar catalogue

broad-band quasar colours is not expected to improve among reddened populations and so we apply this scatter as a floor on the photometric errors to avoid large contributions to the χ^2 values (Section 2.3.3).

2.3.1 QUASAR MODEL

We make use of a refined version of the quasar model described in Maddox et al. (2008), which has been used in a number of studies including Hewett et al. (2006) and Maddox et al. (2012). The continuum in the rest-frame UV is represented by two power-laws, $f(\nu) \propto \nu^{\alpha}$, where $\alpha = -0.424$ at $\lambda \leq 2340$ Å and $\alpha = -0.167$ at $\lambda > 2340$ Å. To account for the reddening of the quasar, we apply an extinction curve (Eqn. 2.2), which has been determined empirically using quasars in the seventh data release of the Sloan Digital Sky Survey (SDSS DR7) and is very similar in form to that presented by Gallerani et al. (2010). Whilst there is no 2200 Å feature in the extinction curve, the amount of extinction at wavelengths < 2500 Å is somewhat less than that derived from the Small Magellanic Cloud (SMC) (Pei, 1992). We note, however, that due to the significant reddening of the quasars in our sample ($E(B-V) > 0.5$), the extinction of the quasar light in the rest-frame UV is so great that the exact form of the extinction curve is not important. The results presented in this paper would be essentially identical if an SMC-like extinction curve were used.

$$k_{\rm AGN}(\lambda) = 1.39\lambda_{\mu m}^{-1.2} \tag{2.2}$$

When applying the extinction curve in Eqn. 2.2, the flux changes by some factor such that

$$F_{\rm obs}(\lambda) = F_{\rm int} \times 10^{-0.4A_{\lambda}}, \tag{2.3}$$

where $A_{\lambda} = k(\lambda)E(B-V)$ and $F_{\rm obs}$ and $F_{\rm int}$ denote the the observed and intrinsic flux, respectively.

The above quasar model also incorporates UV and optical emission lines and FeII multiplets based on the Large Bright Quasar Survey (LBQS) composite of Francis et al.

(1991). In general the strengths of the emission lines do not significantly affect the quasar broad-band colours except in the case of Hα, which has a higher equivalent width relative to the other lines. We therefore adjust the Hα equivalent width in the quasar model for each reddened quasar to match that measured from the NIR spectra in Banerji et al. (2015a, 2012). Hence, all reddening estimates for the quasars presented in this paper account for the effect of the Hα emission line on the observed colours.

2.3.2 HOST GALAXY MODEL

A key aim of this study is to investigate whether the emission observed in the rest-frame UV is consistent with that of a star-forming host. Given the limited photometry tracing the rest-frame UV emission, we are unable to solve for all properties of the galaxy in the fitting. Instead, we consider a single star-forming galaxy SED template from Bruzual and Charlot (2003) with a constant star formation history (SFH) to model the host galaxy emission. The galaxy model is attenuated using a two-component Charlot and Fall (2000) dust model, with $\tau_V = 1.0$ (corresponding to an $E(B-V)_{\rm gal} \simeq 0.35$) affecting the young stellar populations, which is consistent with the level of dust extinction seen in local star-forming galaxies. In cases where we see a significant deviation of the rest-frame UV-slope as traced by our g and r-band photometry, from that in the default host galaxy model, we also consider galaxy models with $\tau_V = 0.2$ and $\tau_V = 5.0$, representing bluer and redder rest-frame UV colours respectively (Bruzual and Charlot, 2003). We note however, that the rest-frame UV slope in the host galaxy model is sensitive to both the dust content (τ_V) and the SFH. Due to the limited photometry tracing the rest-frame UV and the degenerate nature of these two parameters, we cannot derive meaningful estimates for both τ_V and the SFH, so we are limited to these discrete scenarios. In all cases, we assume a Chabrier (2003) initial mass function (IMF) and solar metallicity.

2.3.3 FITTING METHOD

We fit the combined optical+NIR photometry of the individual quasars using combinations of the models described above, in order to investigate the source of the excess rest-frame

UV emission. In particular, we consider three scenarios: (i) the rest-frame UV flux arises from resonantly scattered Lyman-α emission, (ii) the excess emission is scattered continuum light from the central quasar, and (iii) we are seeing UV emission due to star formation in the quasar host galaxy. Although in reality, the rest-frame UV emission is likely due to some combination of the above, the limited DES photometry means we are unable to simultaneously solve for a mix of multiple scenarios. Instead, we seek only to determine the dominant source in each case. To quantify the likelihood of each scenario, we make use of χ^2 statistics, calculating the reduced χ^2 for each quasar in the sample, i.e.

$$\chi^2_{\rm red} = \sum_i \left(\frac{F_{\rm phot,i} - F_{\rm mod,i}}{\sigma_{\rm i}} \right)^2 \Big/ N, \tag{2.4}$$

where a $\chi^2_{\rm red} \sim 1$ indicates a good fit. $F_{\rm phot}$ and $F_{\rm mod}$ denote the photometric and model fluxes respectively. N is the number of degrees of freedom (with $N = N_{\rm data} - N_{\rm param}$) and σ denotes the photometric errors, floored at 10 per cent. In order to obtain full posterior distributions for all free parameters and marginalise over nuisance parameters, we employ a Markov Chain Monte-Carlo (MCMC) method (Foreman-Mackey et al., 2013; Hastings, 1970; Metropolis et al., 1953) to explore the parameter space. Throughout the fitting we assume flat priors across the entire parameter space.

2.4 RESULTS

This section presents the results of fitting different combinations of the above models to the combined optical+NIR photometry. We initially consider only a reddened quasar template, but later consider three possible sources of the rest-frame UV emission - (i) resonantly-scattered Lyman-α, (ii) scattered quasar continuum and (iii) a relatively un-obscured star-forming host galaxy.

2.4.1 QUASAR ONLY SED-FITS

Whilst the majority of objects in our are poorly fit by this model, returning a $\chi^2_{\rm red,QSO} \gtrsim 10$, Four quasars - VHSJ2024-5623, VHSJ2100-5820, VHSJ2257-4700 and ULASJ0016-0038

- return a much lower $\chi^2_{\rm red,QSO} \lesssim 2.5$, which we consider to be a good fit. Given the lack of photometric data available and the number of assumptions made about the SED models in this chapter, we would not expect a $\chi^2_{\rm red,QSO} = 1$, even if another component were to be introduced into the model. We therefore suggest that we cannot distinguish any additional component of UV flux from the quasar-only scenario and therefore We begin by modelling the photometry with a reddened quasar template, setting the only free parameter - the quasar dust reddening ($E(B-V)_{\rm QSO}$) - to lie in the range $0.3 \leq E(B-V)_{\rm QSO} \leq 5.0$. Four quasars are found to be well-fit by this model - VHSJ2024-5623, VHSJ2100-5820, VHSJ2257-4700 and ULASJ0016-0038, returning a $\chi^2_{\rm red,QSO} \lesssim 2.5$ and residuals $(F_{\rm mod} - F_{\rm phot}) < 2\sigma$ across all bands. The fitted templates for each of these four quasars, along with their associated residuals, are presented in Fig. 2.3. A full list of $\chi^2_{\rm red,QSO}$ values, as well as χ^2 results for all models presented in this chapter are given in Table A.1 (*appendix*).

The derived values of $E(B-V)_{\rm QSO}$ for each of the four quasars in Fig. 2.3 are presented in Table 2.5, with all four quasars returning an $E(B-V)_{\rm QSO}$ consistent to within 0.1 of those presented in Banerji et al. (2015a, 2012) (hereafter denoted $E(B-V)_{\rm QSO,B}$). Although values of $E(B-V)_{\rm QSO,B}$ were derived using only the NIR JHK-band photometry, our fitting provides little evidence for additional rest-frame UV emission in the DES Y1A1 photometry of these quasars. Despite the MODEST classifier characterising two of these sources (VHSJ2024-5623 and VHSJ2100-5820) as high-confidence galaxies in the DES g and r-bands, we find that a reddened quasar SED is sufficient to fit the photometric data in both cases. Any extended emission in these galaxies is therefore faint and difficult to disentangle from the quasar emission via SED modelling. As such, we find these four quasars to be well characterised by a reddened-quasar template alone and therefore exclude them from the remainder of our analysis. Conversely, the remaining 13 quasars in the sample return $\chi^2_{\rm red,QSO} > 5$ when fitted in the above manner, indicating that some additional component is required in the model to account for the observed rest-frame UV flux.

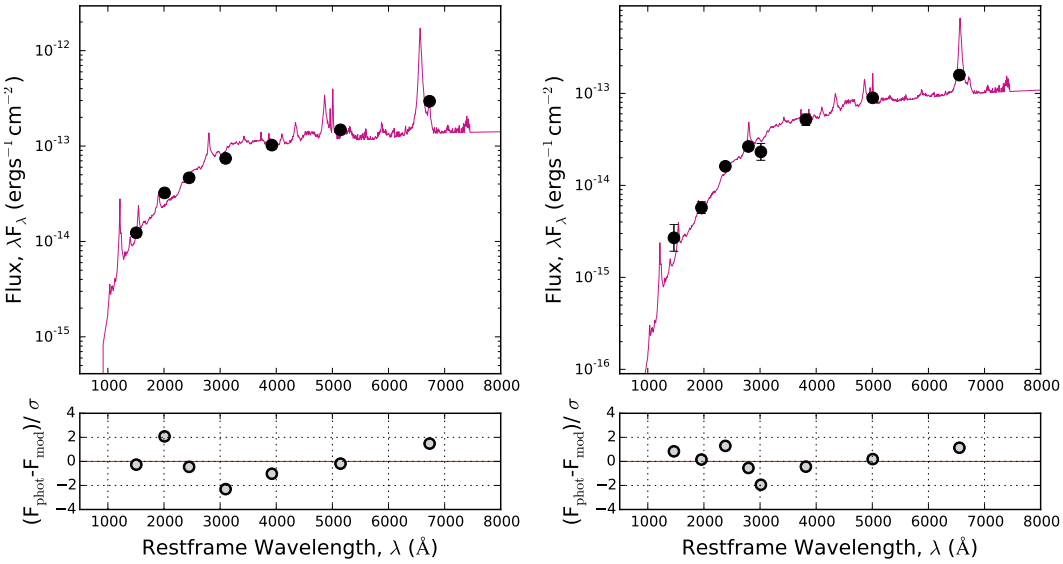

(a) ULASJ0016-0038

(b) VHSJ2024-5623

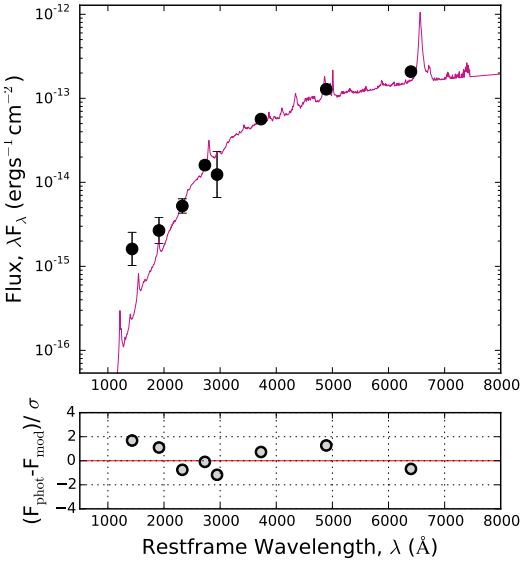

(c) VHSJ2100-5820

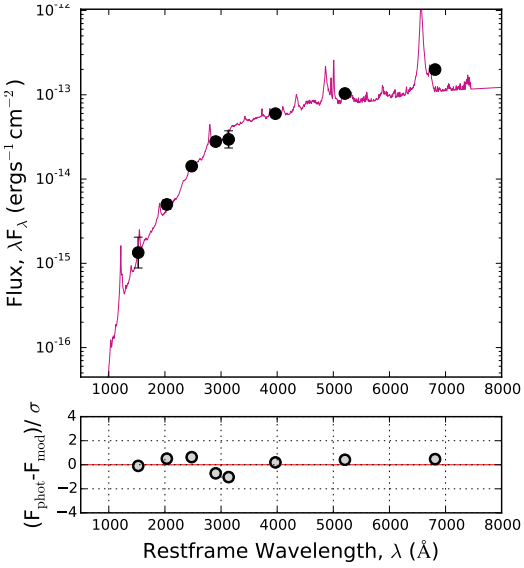

(d) VHSJ2257-4700

Fig. 2.3 *Upper panels:* Best-fit quasar SEDs for ULASJ0016-0038 (a), VHSJ2024-5623 (b), VHSJ2100-5820 (c), VHSJ2257-4700 (d) for which $\chi^2_{\rm red,QSO} \lesssim 2.5$. Black points show the *grizY* DES and *JHK* VHS/ULAS photometry. *Lower panels:* The error-weighted residuals for each fit.

Table 2.5 $E(B-V)_{\rm QSO}$ values for the four quasars returning $\chi^2_{\rm red,QSO} \lesssim 2.5$. Dust extinction values derived by fitting the NIR photometry (Banerji et al., 2015a, 2012) ($E(B-V)_{\rm QSO,B}$) are given for reference.

Name	$E(B-V)_{\rm QSO}$	$E(B-V)_{\rm QSO,B}$
ULASJ0016-0038	0.43	0.5
VHSJ2024-5623	0.58	0.6
VHSJ2100-5820	0.81	0.8
VHSJ2257-4700	0.67	0.7

2.4.2 SCATTERED LIGHT

SCATTERED LYMAN-ALPHA EMISSION

One possible explanation for the rest-frame UV flux in the 13 remaining quasars is Lyman-α emission, which can appear spatially extended due to resonant scattering by the surrounding material. We immediately rule out this possibility for seven of the quasars in our sample, as the Lyman-α emission falls outside the wavelength range of the DES g-band[3]. We model the remaining six quasars - ULASJ2200+0056, VHSJ2227-5203, VHSJ2306-5447, ULASJ2315+0143, VHSJ2332-5240 and VHSJ2355-0011 - with a two-component model consisting of a reddened quasar template and a Lyman-α emission line. As in the quasar-only fitting (Section 2.4.1), $E(B-V)_{\rm QSO}$ is set to lie in the range $0.3 \leq E(B-V)_{\rm QSO} \leq 5.0$, while the fraction of scattered Lyman-α can take values $0 \leq f_{\rm ly\alpha} \leq 1$, where $f_{\rm ly\alpha} = 1$ represents the complete scattering of Lyman-α photons.

Fitting this model returns $\chi^2_{\rm red,ly\alpha} > 2.5$ for four of the six quasars listed above, indicating that scattered Lyman-α emission cannot accurately reproduce the rest-frame UV flux observed in these systems. Although both ULASJ2200+0056 and VHSJ2306-5447 return $\chi^2_{\rm red,ly\alpha} \sim 2$, we note that excess rest-frame UV emission relative to the reddened quasar model is detected in multiple bands in ULASJ2200+0056, further ruling out the scattered Lyman-α scenario for this quasar. From this, we conclude VHSJ2306-5447 to be the only quasar for which the rest-frame UV flux may arise solely from Lyman-α emission. The best fit SED of this scenario for VHSJ2306-5447 in shown in Fig. 2.4. For the remaining 12 quasars, we require some other mechanism to characterise the observed emission in the rest-frame UV.

SCATTERED QUASAR CONTINUUM LIGHT

It is also possible that some fraction of the rest-frame UV quasar continuum light is being scattered into our line of sight by the surrounding dust. The extent of this scattering is

[3]Lyman-α lies at 1216 Å in the rest-frame, which corresponds to 3155-4446Å in the observed frame over the full redshift range of our sample. Thus the Lyman-α line can only affect the DES g-band fluxes in our SED fits for all the quasars.

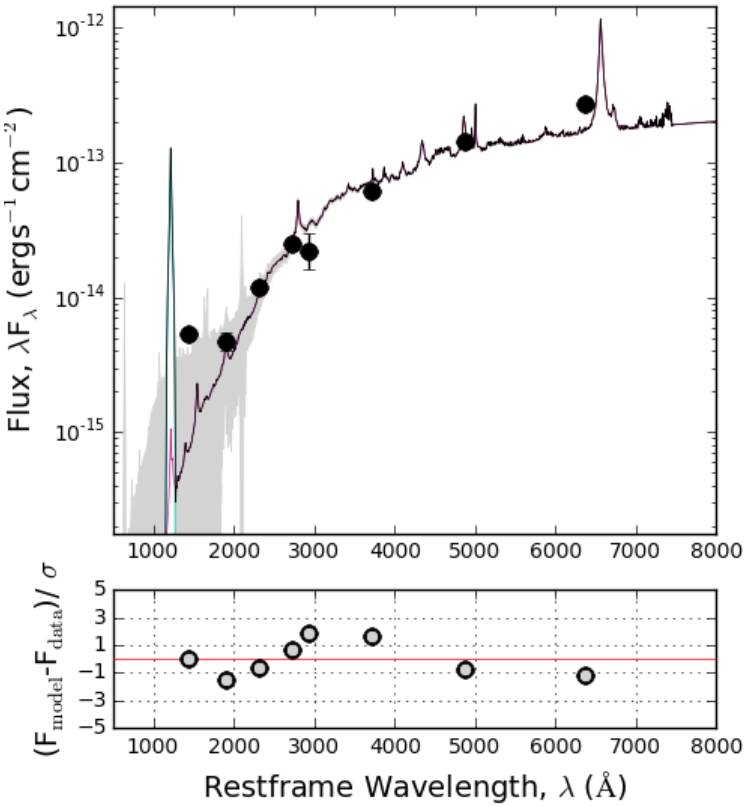

Fig. 2.4 Best-fit model (black) for VHSJ2306-5447 with individual Lyman-α (blue) and reddened quasar (pink) components overlaid.

assumed to be wavelength-independent and is modelled with two quasar templates, one of which is completely un-obscured to represent the scattered continuum. The dust reddening of the obscured quasar and the fraction of scattered continuum form the two free parameters in the fitting, taking values $0.3 \leq E(B-V)_{\rm QSO} \leq 5.0$ and $0 \leq f_{\rm QSO} \leq 1$ respectively, where an $f_{\rm QSO} = 1$ represents the complete scattering of the quasar continuum. This model generally appears to provide a good fit to the photometry, finding a scattering fraction $\sim$0.2 per cent across all sources and returning a $\chi^2_{\rm red,cont} < 2.5$ in 10 of the 13 quasars, with only three quasars - VHSJ2028-5740, VHSJ2227-5203 and VHSJ2256-4800 - returning $\chi^2_{\rm red,cont} > 2.5$.

The MODEST classifier shows evidence for spatially extended emission in all but two (ULASJ2200+0056 and ULASJ2224-0015) of the quasars well-fit by this model (Section 2.2). Obied et al. (2016) show that giant 'scattering cones' of free electrons and dust can scatter the quasar continuum out to $\sim$ 10kpc, resulting in extended regions with narrow line emission and indeed integral field spectroscopy of luminous, obscured quasars have shown narrow-line

regions extended over scales of ∼20-30 kpc (Liu et al., 2013). The NIR spectra of our reddened quasar sample (Banerji et al., 2015a, 2012) however, show emission from narrow line regions to be weak, thus ruling out the presence of such a scattering cone. Considering the small fraction of quasar light being scattered in our sample (∼0.2 per cent), it is also possible that extended emission arises from scattering within the interstellar medium (ISM) (e.g. Young et al., 2009). We note however, that in an ionised ISM with a conventional dust-to-gas ratio, scattering by dust has been shown to dominate over free-electron scattering by a factor ∼10 in the UV (Draine, 2003; Weingartner and Draine, 2001). Draine (2003) have shown this dust scattering to be strongly biased towards forward scattering, meaning the single scattering of the quasar continuum is unlikely to scatter out from the dust in the plane of the galaxy and into our line of sight. Furthermore, if a small fraction of this emission were to be scattered into our line of sight, we would expect a much bluer quasar spectrum than the fitted unobscured quasar SED, as the scattering efficiency rapidly increases at shorter wavelengths. We find no evidence to suggest a bluer quasar template would better fit the *gri* DES photometry of our sample and hence conclude this scenario to be unlikely. Although we cannot rule out the scattered light scenario in explaining the UV excess in ULASJ2200+0056 or ULASJ2224-0015, where we see no evidence for extended emission, we likely require an alternative explanation for the remainder of our quasar sample.

The above SED model, used to test for the scattered quasar continuum, could also result from a system with a close binary AGN (e.g. following a merger event) in which only one is significantly obscured by dust. If our systems were to contain two quasars they would be at small physical separations, but have very different line-of-sight extinctions. Based on our fitting results, the second quasar would also need to have $L_{bol,QSO} \sim 500$ times (∼7 magnitudes) fainter that the primary (reddened) quasar and although there are very few constraints on the number densities of such low-luminosity AGN, the combination of properties required for this explanation to hold makes the scenario somewhat implausible.

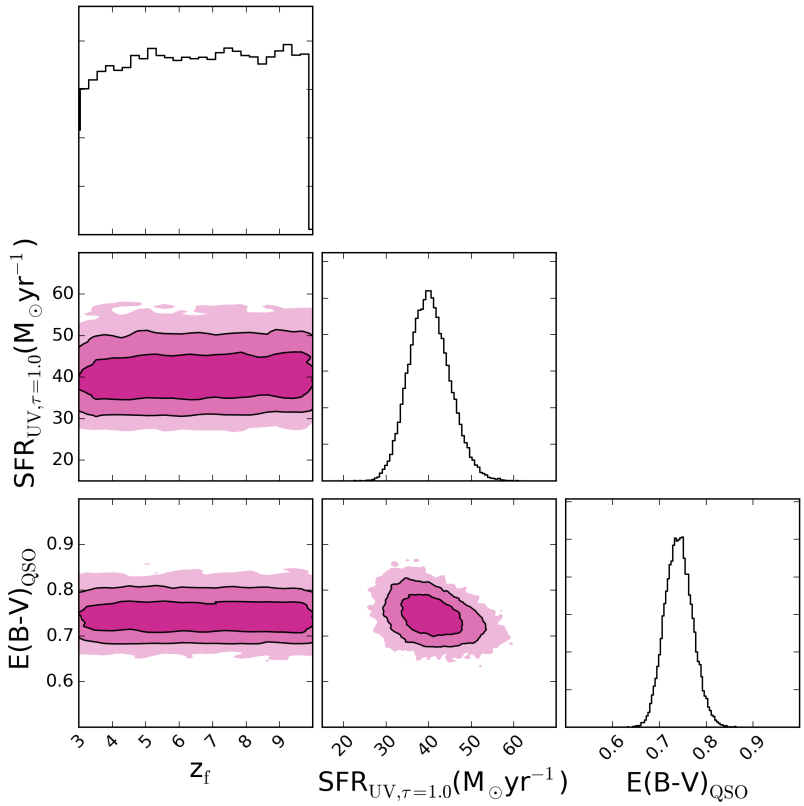

Fig. 2.5 1D and 2D posterior distributions from the MCMC fitting for VHSJ2235-5750 - a representative quasar from the sample. Shaded regions in the 2D distributions denote 1,2 and 3σ parameter uncertainties in the fitting. The SFR and associated uncertainties (prior to dust corrections) are based on a galaxy template with τ_V = 1.0 and have been converted from the normalisation of the galaxy template (f_{gal}) in the fitting. Histograms illustrate the relative 1D probability distributions of each parameter.

2.4.3 HOST GALAXY EMISSION

Finally, we explore the possibility of the rest-frame UV flux arising from a relatively unobscured star-forming host galaxy modelled by the galaxy templates outlined in Section 2.3, assuming a constant SFH. Although the real SFH of the galaxy is likely to consist of bursts of star formation, alongside phases of quiescence and steady formation, we later demonstrate this assumption of a constant SFH to provide a good description of the rest-frame UV photometry for the vast majority of our sample.

Throughout the fitting we consider three free parameters - $E(B-V)_{QSO}$, the formation redshift, z_f, and the normalisation of the galaxy template, f_{gal} - set to take values 0.3 $\leq E(B-V)_{QSO} \leq$ 5.0, 3 $\leq z_f \leq$ 10 and 0 $\leq f_{gal} \leq$ 1 respectively, where an f_{gal} = 1 denotes a galaxy flux equal to that of the quasar template in the rest-frame UV ($\sim$ 900-3000Å) prior

to any quasar dust reddening. We note that the value of $f_{\rm gal}$ is primarily constrained by the DES photometry tracing the rest-frame UV emission and therefore directly traces the UV flux from young stars. Although we are unable to constrain the total mass of the host galaxy, we use the mass of the fitted galaxy template[4], assuming a constant SFH and a normalisation, $f_{\rm gal}$, to derive *instantaneous* SFRs based on the rest-frame UV flux. In this way, $f_{\rm gal}$ can be directly converted to an instantaneous SFR ($\rm SFR_{UV,\tau_v=1.0}$). Figure 2.5 illustrates parameter solutions derived from the MCMC fitting routine for a typical quasar - VHSJ2235-5750 - where this conversion from $f_{\rm gal}$ to $\rm SFR_{UV,\tau_v=1.0}$ has been made (solutions for all 17 quasars can be found in Fig. A.1).

For every quasar in our sample, we recover well-constrained solutions for both $E(B-V)_{\rm QSO}$ and $\rm SFR_{UV,\tau_v=1.0}$, despite being unable to constrain the age of the system. The lack of constraint on z_f in the fitting is unsurprising, given the Gyr timescales between z and z_f - much longer than the $\sim$ a few Myr lifetime of O and B stars. Over Gyr timescales, stars contributing to the UV at z_f therefore no longer contribute to the UV emission at z meaning the inferred $\rm SFR_{UV,\tau_v=1.0}$ at z is effectively independent from the choice of z_f in the fitting. Indeed, we observe this to be the case in Fig. A.1. We therefore remove z_f as a free parameter in the fitting, choosing instead to adopt a fixed value of z_f = 6 and solve for the two remaining parameters. The resulting SED fits are presented in the upper panels of Fig. 2.6. The lower panels of Fig. 2.6 show the residuals of the fit, which are found to be small in all bands, typically returning $(F_{\rm phot} - F_{\rm mod}) < 2\sigma$. For nine of the 13 quasars in Fig. 2.6 we derive $\chi^2_{\rm red,GAL+QSO} < 2.5$, indicating the rest-frame UV flux in these objects is well fit by a galaxy template with $\tau_{\rm V}$ = 1.0. Even in the remaining four quasars for which we derive $\chi^2_{\rm red,GAL+QSO} > 2.5$, we recover a much better fit than with a reddened quasar template alone (Section 2.4.1), finding ($\chi^2_{\rm red,QSO}$ - $\chi^2_{\rm red,GAL+QSO}$) > 9 for 11 quasars and ($\chi^2_{\rm red,QSO}$ - $\chi^2_{\rm red,GAL+QSO}$) > 3 for the remaining two. This shows that the addition of a host galaxy component to the model significantly improves the goodness of fit for all 13 quasars.

Table 2.6 presents instantaneous SFRs derived from the UV flux of the fitted galaxy SEDs in Fig. 2.6, where we have assumed $\tau_{\rm V} = 1.0$ and z_f = 6.0. SFRs are given both before

[4]Masses are calculated using EzGal (www.baryons.org)

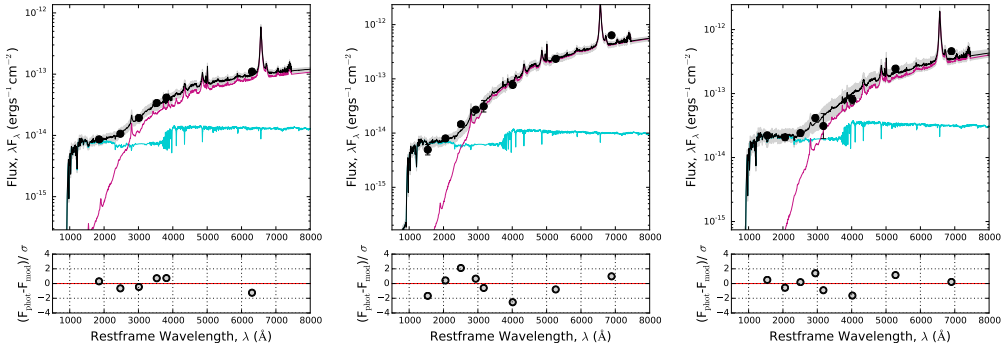

(a) ULASJ1002+0137 **(b)** VHSJ2028-5740 **(c)** VHSJ2115-5913

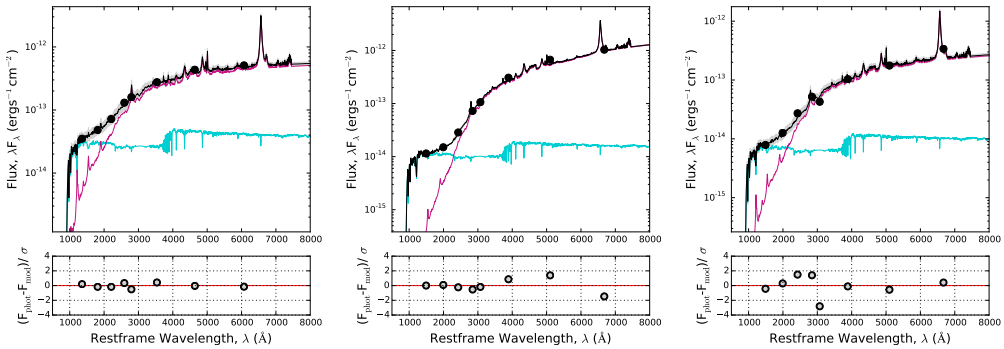

(d) ULASJ2200+0056 **(e)** VHSJ2220-5618 **(f)** ULASJ2224-0015

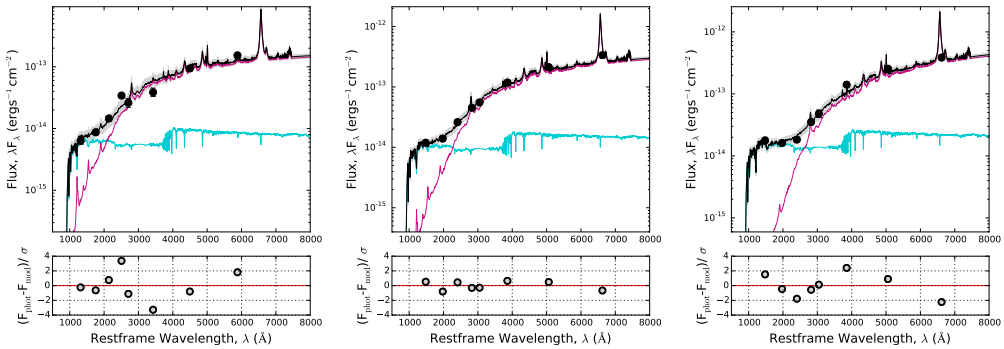

(g) VHSJ2227-5203 **(h)** VHSJ2235-5750 **(i)** VHSJ2256-4800

Fig. 2.6 *Upper panels:* Best fit models (black) for the 13 reddened quasars with individual galaxy (blue) and quasar (pink) components overlaid. Black points show the *grizY* DES and *JHK* VHS/ULAS photometry. Grey shaded regions illustrate 1σ uncertainty about the best-fit model solution. *Lower panels:* Residuals for all photometric bands, scaled to the photometric errors (floored at 10 per cent).

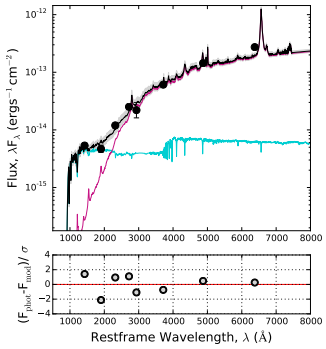

(j) VHSJ2306-5447

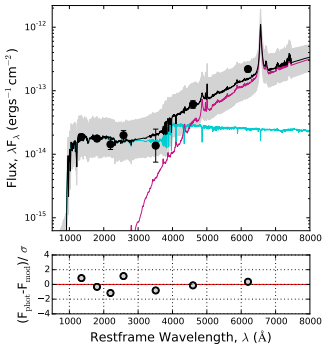

(k) ULASJ2315

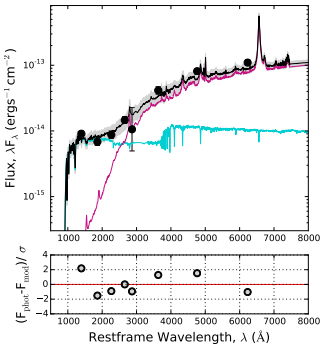

(l) VHSJ2332-5240

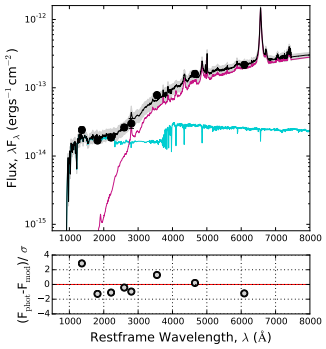

(m) VHSJ2355-0011

Fig. 2.7 *continued from Fig.2.5*

($SFR_{UV,\tau_V=1.0}$) and after (SFR_{UV}) dust correction has been applied to the galaxy template. We note that although the Charlot and Fall (2000) extinction curve used to correct for the dust is age-dependent, the assumptions made about z_f have a minimal effect on the resulting SFRs, changing the SFR by $\pm$ 5-10 per cent for a change in $z_f \pm 1.0$. These variations lie below the 1σ parameter uncertainties derived from the MCMC fitting, also given in Table 2.6, and so we do not discuss them further. For the four quasars that were well-fit by a single reddened-quasar SED (Section 2.4.1), we derive upper limits on their SFRs by repeating the above host galaxy fitting for these objects.

We also present the $E(B-V)_{QSO}$ values calculated in the fitting in Table 2.6, together with those from Banerji et al. (2015a, 2012) ($E(B-V)_{QSO,B}$), who fit the *JHK* photometry with a reddened quasar model and an Sb galaxy template to model the quasar host. The introduction of the DES photometry in our study allows both the SED and luminosity of the host galaxy to be better constrained. With the addition of this *grizy* photometry, we

Table 2.6 UV-derived SFRs prior to dust correction ($SFR_{UV,\tau_v=1.0}$) and corrected for a τ_v = 1.0 (SFR_{UV}). $E(B-V)_{QSO}$ (assuming z_f = 6) and $E(B-V)_{QSO,B}$ (Banerji et al., 2015a, 2012) are also presented. Quoted errors denote the 1σ uncertainties on the best-fit model, found by sampling the SEDs fitted during the MCMC routine. Upper limits on the SFR are given to a 68.27 per cent confidence (1σ).

Name	$SFR_{UV,\tau=1.0}$ ($M_\odot yr^{-1}$)	SFR_{UV} ($M_\odot yr^{-1}$)	$E(B-V)_{QSO}$	$E(B-V)_{QSO,B}$
ULASJ0016-0038	≤ 25	≤ 55	0.48 ± 0.03	0.5
ULASJ1002+0137	10 ± 5	25 ± 5	0.83 ± 0.04	1.0
VHSJ2024-5623	≤ 10	≤ 20	0.61 ± 0.03	0.6
VHSJ2028-5740	25 ± 5	50 ± 10	$1.12^{+0.04}_{-0.06}$	1.2
VHSJ2100-5820	≤ 10	≤ 20	0.84 ± 0.03	0.8
VHSJ2115-5913	70^{+15}_{-10}	160 ± 30	$1.08^{+0.07}_{-0.08}$	1.0
ULASJ2200+0056	160 ± 20	375 ± 50	0.58 ± 0.03	0.5
VHSJ2220-5618	40 ± 5	95 ± 10	0.94 ± 0.02	0.8
ULASJ2224-0015	25 ± 5	60 ± 5	0.72 ± 0.03	0.6
VHSJ2227-5203	35 ± 5	85^{+15}_{-10}	0.63 ± 0.04	0.9
VHSJ2235-5750	40 ± 5	95 ± 10	0.74 ± 0.03	0.6
VHSJ2256-4800	60 ± 5	135 ± 15	$0.93^{+0.03}_{-0.04}$	0.6
VHSJ2257-4700	≤ 5	≤ 10	$0.69^{+0.02}_{-0.03}$	0.7
VHSJ2306-5447	20 ± 5	45 ± 5	0.81 ± 0.03	0.7
ULASJ2315+0143	100^{+85}_{-50}	230^{+200}_{-115}	$1.78^{+0.24}_{-0.28}$	1.1
VHSJ2332-5240	35 ± 5	$85 \pm ^{+15}_{-10}$	0.79 ± 0.05	0.6
VHSJ2355-0011	95 ± 15	225 ± 35	0.90 ± 0.05	0.7

expect to derive higher values of $E(B-V)_{\rm QSO}$ than $E(B-V)_{\rm QSO,B}$ for objects in which we see prominent galaxy emission, as this emission is likely to contribute to the J-band ($\sim$ 3800Å) and therefore reduce the relative fraction of quasar flux in this band. We show this to be true for eight of the 13 quasars in the sample, typically finding $E(B-V)_{\rm QSO}$ to be $\sim$ 0.1 - 0.3 larger than $E(B-V)_{\rm QSO,B}$. The reddest quasar in our sample - ULASJ2315+0143 - returns an $E(B-V)_{\rm QSO} \sim 0.7$ larger than $E(B-V)_{\rm QSO,B}$, although the uncertainty on this value is much larger than for the rest of the sample. A further three quasars - VHSJ-2028-5740, VHSJ2115-5913 and ULASJ2200+0056 - return an $E(B-V)_{\rm QSO}$ consistent with $E(B-V)_{\rm QSO,B}$ to within 0.1, with the remaining two quasars - ULASJ1002+0137 and VHSJ2227-5203 - returning an $E(B-V)_{\rm QSO} \sim 0.2$ - 0.3 lower than $E(B-V)_{\rm QSO,B}$. We note that the J-band photometry is not available for ULASJ1002+0137 (Fig. 2.6a), meaning $E(B-V)_{\rm QSO,B}$ has been constrained from only the H and K-band photometry. From Fig. 2.6a, we find that these two bands indicate a steeper rest-frame NIR slope than is implied when the DES photometry is included in the fit, meaning a model based on just the H and K-band data would likely overestimate the quasar reddening. Similarly, the J-band photometry in VHSJ2227-5203 lies below our fitted SED model (Fig. 2.6g), indicating that a higher reddening would be derived without the inclusion of the *grizY* photometry. We therefore find no direct conflict between the results of Banerji et al. (2015a, 2012) and the results in ths chapter.

UV SLOPE OF THE GALAXY SED

In general, the galaxy model with a constant-SFH and $\tau_{\rm V}$ = 1.0 provides a good fit to our reddened quasar sample. This is demonstrated in Fig. 2.8, where we present the median average fitting residuals ($m_{\rm data}$ - $m_{\rm model}$) for each band. Four quasars however - VHSJ2028-5740, VHSJ2227-5203, VHSJ2256-4800 and VHSJ2355-0011 - return $\chi^2_{\rm red,GAL+QSO} \lesssim 2.5$ when this default host galaxy model is assumed. We consider VHSJ2227-5203 further in Section 2.4.3, but for the remaining three objects we find the g-band photometry to lie below the fitted SED in VHSJ2028-5740 (Fig. 2.6b) and above the fitted SED in VHSJ2256-4800 (Fig. 2.6i) and VHSJ2355-0011 (Fig. 2.7m), indicating that a galaxy model with

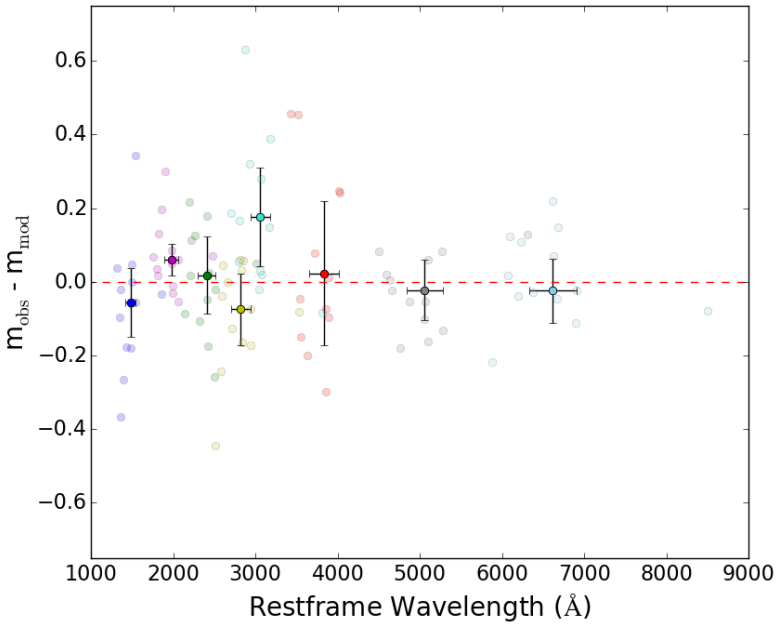

Fig. 2.8 Magnitude differences between the fitted SED and the DES *grizY* photometry, assuming a galaxy template with τ_V = 1.0. Dark points denote the median average in each filter with error bars showing the median absolute deviation of the data points in each passband.

τ_V=1.0 cannot reproduce the slope of the rest-frame UV flux in these systems. We find that significantly improved $\chi^2_{red,GAL+QSO}$ values (∼1-2) can be obtained by adopting a galaxy model with τ_V = 5.0 for VHSJ2028-5740 and τ_V = 0.2 for VHSJ2256-4800 and VHSJ2355-0011. We note however, that the effect of this dust extinction on the rest-frame UV slope is highly degenerate with that caused by changes in the SFH, meaning a similar improvement in $\chi^2_{red,GAL+QSO}$ may also be obtained by adjusting the SFH. The exact SFRs derived from the SED-fitting are therefore dependent on both the adopted SFH and dust content of the host galaxies, the constraints of which lie beyond the scope of this work given the limited DES photometry. Nevertheless, the detection of rest-frame UV emission consistent with star formation in the sample is robust.

QUASAR VARIABILITY

In addition to the assumed SFH and dust content of the host galaxy, quasar variability may also contribute to the large $\chi^2_{red,GAL+QSO}$ values. The observations from DES and VHS/ULAS were taken about three years apart, corresponding to approximately a year in the rest-frame of

our quasars. Over such time scales, luminous quasars have been shown to vary by $\lesssim 0.1$ mag in the rest-frame optical (e.g. De Vries et al., 2005; MacLeod et al., 2012; Vanden Berk et al., 2004). Even accounting for the small amplitude of this variability, systematic offsets between the DES and VHS/ULAS photometry are not evident for the sample as a whole. We consider the possibility however, that individual quasars in our sample may exhibit variability with larger amplitudes and for VHSJ2227-5203 ($\chi^2_{\rm red,GAL+QSO} \lesssim 2.5$), we find the JHK-band photometry to appear several tenths of a magnitude fainter than that extrapolated from the $grizY$ photometry. To test whether variability could explain the poor fit of VHSJ2227-5203, the fitting routine is re-run, having increased the JHK magnitudes by 0.2 mag - the magnitude offset required to align the DES and VHS photometry. However, the fit of this adjusted photometry returned $\chi^2_{\rm red,GAL+QSO} \simeq 5$, meaning that an offset between the DES and VHS photometry due to quasar variability, cannot account for the large $\chi^2_{\rm red,GAL+QSO}$ in VHSJ2227-5203. We therefore conclude that photometric quasar variability does not play a significant role in our sample of reddened quasars and therefore does not affect the conclusions.

2.5 DISCUSSION

We have found evidence for an excess of rest-frame UV emission, relative to a reddened quasar SED, in 13 of the 17 quasars considered in this paper. For each quasar in our sample, we have explored three possible sources of this emission - resonantly scattered Lyman-α emission, scattered light from the quasar continuum and a relatively un-obscured star forming host, demonstrating the rest-frame UV emission to be consistent with star formation in at least 11 quasars. Furthermore, we have found two quasars - VHSJ2306-5447 and ULASJ2224-0015 - to exhibit rest-frame UV emission consistent with either star formation or scattered light and have derived instantaneous SFRs across the entire quasar sample, based upon their rest-frame UV flux. The following section compares our results to a range of independent studies and outlines connections between the properties of these luminous, high-redshift, reddened quasars and their host galaxies.

2.5.1 COMPARISON TO OTHER SFR ESTIMATES FOR HEAVILY REDDENED QUASARS

Hα SFRs

Fifteen of the reddened quasars in our sample overlap with those in Alaghband-Zadeh et al. (2016a), who look for narrow Hα emission that could be associated with star formation in the NIR spectra. Narrow Hα emission is detected in nine of the 15 quasars in their sample, from which Alaghband-Zadeh et al. (2016a) derive extinction-corrected SFRs assuming a Calzetti dust extinction law (Calzetti et al., 2000) and a dust attenuation towards the star-forming regions equal to that towards the quasar continuum. In our analysis, one of these nine quasars - VHSJ2100-5820 - does not show an excess of rest-frame UV emission relative to that expected from a reddened quasar and so is not considered further in our comparisons to Hα-derived SFRs. Similarly, we do not include the six quasars with no evidence of narrow Hα emission, for which Alaghband-Zadeh et al. (2016a) derive only upper limits on the SFR, assuming the star-forming regions to be located within the PSF of the SINFONI data (FWHM $\sim$0.5-0.8 arcsec). As we clearly see evidence for rest-frame UV emission on larger scales than this across our sample, the Hα SFR limits for these six quasars are not directly comparable to our work. We therefore only compare our UV-derived SFRs with the Hα SFRs for the eight quasars outlined in Table 2.7, where the Hα SFRs have been re-derived, correcting for τ_V = 1.0, as has been assumed for our galaxy template. Fig. 2.9 shows the comparison between these two measures of SFR.

Fig. 2.9 indicates the two measures of star formation to be broadly correlated, although values of SFR_{UV} appear systematically higher than $SFR_{H\alpha}$ by a factor of $\sim$1.1-4. This lack of a one-to-one correspondence between the two SFR measures is expected however, as several assumptions have been made regarding the quasar host galaxy and the dust attenuation affecting both the UV- and Hα-emitting regions. We also note that Alaghband-Zadeh et al. (2016a) restrict their search for narrow Hα emission to $\sim$0.5-0.8 arcsec regions (corresponding to the size of the PSF in their observations), meaning their study is not sensitive to extended emission on larger scales. Given that the rest-frame UV emission in

Table 2.7 $SFR_{H\alpha}$ for the eight quasars overlapping our host galaxy sample, for which Alaghband-Zadeh et al. (2016a) detect narrow Hα emission. SFRs have been corrected for dust, assuming an $E(B-V)$ = 0.35 to be consistent with the level of dust used in our galaxy template ($\tau_V \sim$1.0).

Name	$SFR_{H\alpha}$ ($M_\odot yr^{-1}$)
ULASJ1002+0137	10 $\pm$5
VHSJ2028-5740	110 $\pm$10
VHSJ2115-5913	45 $\pm$5
ULASJ2200+0056	350 $\pm$15
ULASJ2224-0015	45 $\pm$5
VHSJ2235-5750	85 $\pm$10
VHSJ2332-5240	70 $\pm$10
VHSJ2355-0011	130 $\pm$15

our sample typically extends $\gtrsim$1 arcsec, we expect the SFRs we derive from the spatially-integrated UV flux to generally be higher than those measured from Hα by Alaghband-Zadeh et al. (2016a), which is exactly what we see in Fig. 2.9

Herschel AND ALMA SFRS

Several of the reddened quasars in our sample have also been detected in the far infra-red and millimetre wavelengths, suggesting significant levels of dust-obscured star formation in these sources (Banerji et al., 2017, 2014) exceeding 1000 $M_\odot$ yr^{-1}. Recently, Banerji et al. (2017) studied four reddened quasars with ALMA, finding ubiquitous evidence for large reservoirs of molecular gas and star formation in all four systems. One of these four quasars - ULASJ2315+0143 - overlaps with our sample, and shows resolved CO(3-2) emission elongated in the same direction as the rest-frame UV emission seen in Fig. 2.2o. The ALMA-derived SFR for this source is 6100$\pm$400 $M_\odot yr^{-1}$ and whilst this is significantly larger than the 230 $M_\odot yr^{-1}$ UV-derived SFR inferred from the DES observations, we note that the ALMA SFR is derived from a single photometric data point at ν=103 GHz tracing the Rayleigh-Jeans tail of the dust SED, and could be over-estimated for a number of reasons. Specifically, Banerji et al. (2017) assume no significant contribution from radio synchrotron emission to the millimetre continuum emission, and the dust heating is assumed to be entirely dominated by the star-forming host, without any contribution from the quasar itself.

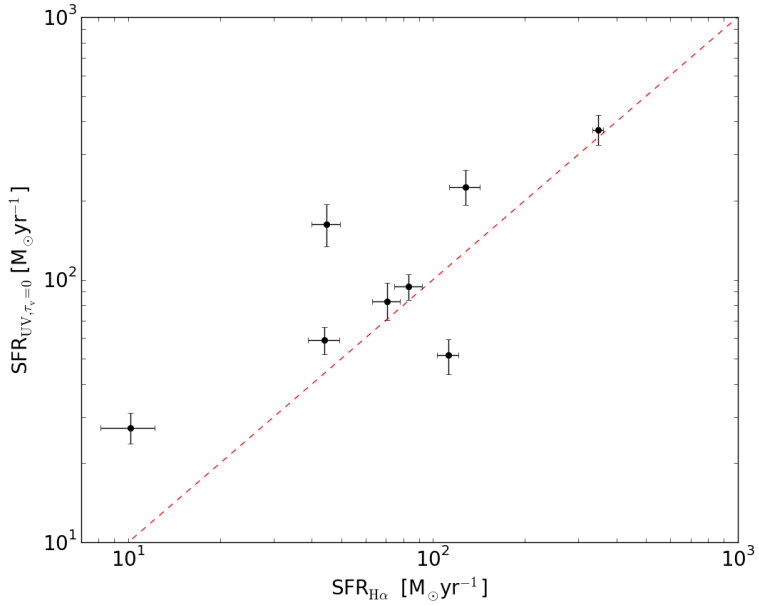

Fig. 2.9 Comparison of SFR_{UV} to $SFR_{H\alpha}$ (Alaghband-Zadeh et al., 2016a). Error bars show the 1σ uncertainties on the calculated SFRs in each case.

Nevertheless, given the significant amount of dust emission seen by ALMA, it is plausible that the rest-frame UV emission in the DES *grizY* bands is only tracing a small fraction of the total star formation in this galaxy.

2.5.2 COMPARISON TO HOT DUST-OBSCURED GALAXIES (HOTDOGS)

Hot Dust Obscured Galaxies (HotDOGs) are a related class of heavily obscured AGN selected using data from the Wide-Field Infra-red Survey Explorer (WISE). They have similar intrinsic AGN luminosities to our reddened quasars but much higher levels of dust obscuration towards the quasar sight-line (Eisenhardt et al., 2012). Assef et al. (2015) recently presented evidence for excess rest-frame UV emission in several HotDOGs and conducted a detailed multi-wavelength investigation of one particular source - W0204-0506 - at $z = 2.1$. In their investigation, Assef et al. (2015) consider scattered AGN light, a second AGN and a star-forming host galaxy as possible sources of the UV emission seen in W0204-0506, concluding scattered light from the AGN to be the most plausible scenario. One reason Assef et al. (2015) give for this conclusion is the unprecedented level of un-obscured star formation required to reproduce the UV flux observed in W0204-0506.

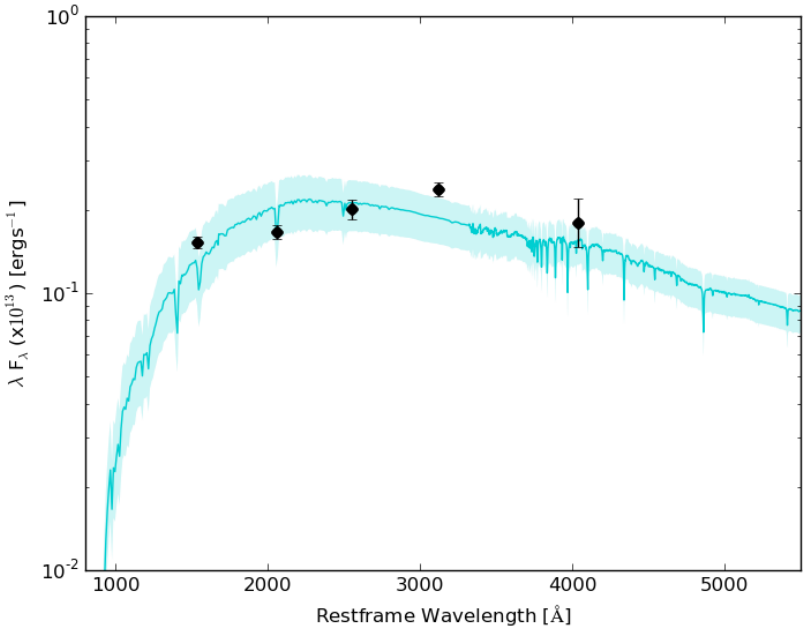

Fig. 2.10 Best fit galaxy template for W0204-0506, assuming τ_V and z_f=6, from which we derive a dust-corrected SFR$\sim$5200 $M_\odot yr^{-1}$. Shaded region illustrates the 1 σ uncertainty about the best-fit solution. Photometry and associated 1σ errors are taken from the work of Assef et al. (2015).

To compare W0204-0506 with the reddened quasars in our sample, we fit the photometry for this source with our constant SFH host galaxy template using the SED- fitting method outlined in Section 2.3 (Fig. 2.10). From Fig. 2.10, we derive a dust-corrected SFR$\sim$5200 $M_\odot yr^{-1}$ for W0204-0506, consistent with the $\sim$5500 $M_\odot yr^{-1}$ derived by Assef et al. (2015). This SFR > 5000 $M_\odot yr^{-1}$ is extreme compared to the moderate SFRs we derive from the rest-frame UV flux of our reddened quasars ($\sim$130 $M_\odot yr^{-1}$), although as discussed in Section 4.4.1, this does not preclude a much higher level of obscured star formation in our sources. Nevertheless, the blue excess *WISE* HotDOGs appear clearly distinct in terms of their properties from the reddened quasar sample considered in this work and hence likely have different mechanisms responsible for the emission in the rest-frame UV.

2.5.3 IS SFR CORRELATED WITH QUASAR LUMINOSITY?

We now explore whether the instantaneous SFRs we derive for the reddened quasar sample are correlated with the bolometric quasar luminosity, $L_{bol,QSO}$. $L_{bol,QSO}$ is calculated from the extinction-corrected rest-frame flux at 5100Å, using a bolometric correction factor of

seven (Vestergaard and Peterson, 2006). The values of $L_{bol,QSO}$ we derive are consistent with those presented in Banerji et al. (2015a, 2012), with only small variations due to the inclusion of the DES photometry in our fitting. SFR_{UV} is plotted as a function of $L_{bol,QSO}$ in Fig. 2.11, where we see a positive correlation between these two quantities. From Fig. 2.11 we find a Spearman's correlation coefficient of $r \simeq 0.6$ with a p-value, $\alpha = 0.03$, i.e. we detect a positive correlation to a 97 per cent confidence level. Although SFR_{UV} and $L_{bol,QSO}$ have both been corrected for dust extinction, we note that the apparent correlation in Fig. 2.11 is not due to this correction, as different corrections have been applied to the quasar and the galaxy individually ($E(B\text{-}V)_{GAL}$=0.35, while $E(B\text{-}V)_{QSO}$ $\sim$0.5-2.0, as solved for in the fitting). We also note that the observed correlation in Fig. 2.11 is not caused by the simultaneous fitting of the galaxy and quasar components in the model, as each of these components is constrained by different photometry. The galaxy SED for example, is primarily constrained by the *gri* DES photometry, whilst the *JHK* VISTA/ ULAS photometry is used to constrain the quasar SED, meaning the two components are essentially decoupled.

The correlation we observe between SFR_{UV} and $L_{bol,QSO}$ in our reddened quasars (Fig. 2.11) is consistent with the work of Harris et al. (2016), who find the SFRs of type-1 quasar host galaxies at $2 < z < 3$ to increase with AGN luminosity up to some limiting rate. Shao et al. (2010) and Netzer (2009) find a similar trend among high luminosity AGN (L_{bol} > 10^{44}ergs^{-1}), but find no such dependency in lower luminosity systems - a result confirmed by independent studies of moderate-luminosity AGN (e.g. Jahnke et al., 2004). Furthermore, Urrutia et al. (2012) find no correlation between SFR and AGN-accretion among reddened quasars at low redshift ($0.4 < z < 1$), suggesting that the trend in Fig. 2.11 may only appear for the most luminous quasars at high redshift.

Although we find some evidence for a relationship between $L_{bol,QSO}$ and SFR_{UV} in our sample, we highlight that this chapter only accounts for the un-obscured, instantaneous star formation rate, based upon the rest-frame UV emission observed in a relatively small sample of 13 reddened quasars and that a number of assumptions have been made regarding the host galaxy properties. Assembling larger samples of such measurements as well as measuring the total, rather than un-obscured, SFRs from SCUBA-2 and ALMA observations will help

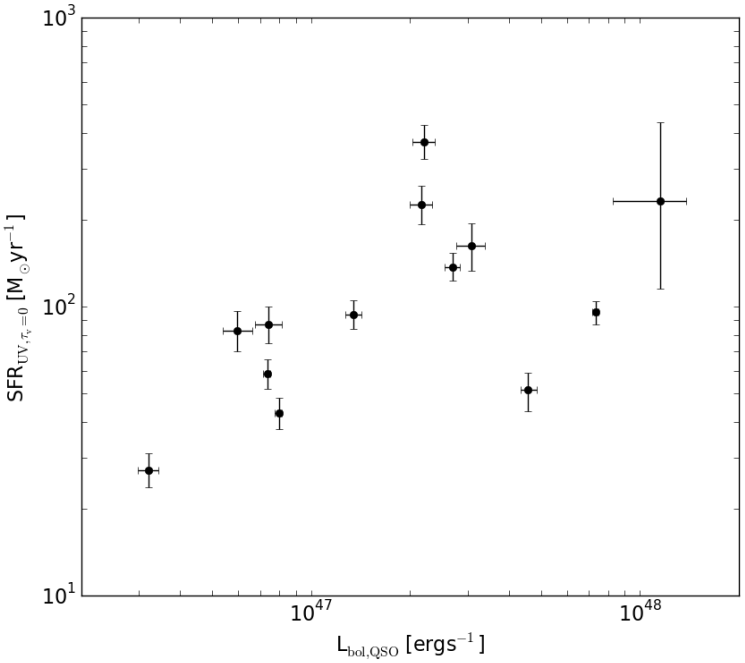

Fig. 2.11 SFR_{UV} as a function of the dust-corrected $L_{bol,QSO}$. Error bars denote 1σ uncertainties on SFR_{UV}.

corroborate whether there is indeed a correlation between star formation rate and quasar luminosity in reddened quasars.

2.6 CONCLUSIONS

We have presented the first rest-frame UV observations for a population of 17 luminous, heavily dust-reddened ($L_{bol,QSO} > 10^{46} ergs^{-1}$, $E(B-V)_{QSO} \sim 0.8$) broad-line quasars at $1.5 < z < 2.7$, making use of DES Year 1 optical photometry along with NIR observations from VHS and ULAS. Our main conclusions can be summarised as follows:

i) We detected an excess of rest-frame UV emission relative to that expected from a reddened quasar template alone in 13 of the 17 sources in our sample. Via SED fitting, we modelled three potential sources of this excess rest-frame UV emission in the reddened quasar sample - resonantly-scattered Lyman-α, scattered light from the quasar continuum and a star-forming host galaxy. In at least ten quasars, we found the rest-frame UV emission to be consistent with the detection of a relatively un-obscured, star forming host galaxy, with

a further three quasars showing emission that could be consistent with either star formation or scattered light.

ii) We estimated the instantaneous SFRs for the quasar host galaxies in the sample based on their rest-frame UV emission, deriving extinction-corrected star formation rates of 25 $\lesssim$ SFR$_{\rm UV}$ $\lesssim$ 365 M$_{\odot}$yr^{-1}, with a mean average SFR$_{\rm UV}$ = 130 $\pm$ 95 M$_{\odot}$yr^{-1}. We note, however, that the SFRs presented in this paper account only for the relatively unobscured component of star formation and therefore do not preclude much higher rates of obscured star formation in these systems. In fact, we see evidence for a much higher obscured SFR in ULASJ2315+0143 based on recent ALMA observations and cannot rule out a similar trend in the remainder of our sample. The unobscured SFRs presented in this paper are found to be broadly consistent with those derived independently from Hα observations using Integral Field Spectroscopy.

iii) We have found evidence for a correlation between the rest-frame UV-derived, dust-corrected star formation rates and the bolometric luminosity of the quasar at the high quasar luminosities probed by our sample. This is consistent with similar trends observed for high-luminosity populations of unobscured quasars.

Overall, we have demonstrated that quasar emission can be disentangled from its host galaxy, even in the most luminous systems, by exploiting dust obscuration towards the quasar. For the first time, populations of these intrinsically-luminous, dusty quasars can now be studied in the rest-frame UV at high redshift thanks to deep, wide-field observations from large imaging surveys like DES. Our analysis has shown that several of the hosts of these reddened quasars are spatially resolved in the DES imaging tracing rest-frame UV wavelengths. This paves the way for future high-resolution imaging and detailed morphological studies of these quasar host galaxies.

CHAPTER 3

A MORPHOLOGICAL STUDY OF REDDENED QUASAR HOSTS AT Z∼2

3.1 INTRODUCTION

Mapping regions of active star formation in galaxies can provide valuable information about the mechanisms by which galaxies form and therefore place constraints on models of their evolution. In particular, understanding star formation in quasar host galaxies can shape our understanding of quasar-galaxy coevolution. At rest-frame UV and optical wavelengths, where unobscured star formation is often traced, the quasar can outshine the galaxy by several orders of magnitude, making the two components in the image difficult to disentangle. For this reason, morphological studies of quasar hosts have largely been confined to low-redshifts, where high spatial resolution is easier to achieve. Whilst a handful of studies have modelled low redshift quasars hosts using ground-based observations (e.g. Hunt and Malkan, 1999; Jahnke et al., 2004; Smith et al., 1986), these tend to be limited to low-luminosity AGN. Jahnke et al. (2004), for example, analyse 19 quasar hosts at $z<0.2$, finding their sample to reside in very symmetric, undisturbed disc-like and elliptical hosts. From this study, they conclude low to intermediate luminosity quasars to be predominantly driven by secular processes such as gas accretion and minor mergers.

At higher quasar luminosities, morphological host galaxy studies have typically depended on space-based *HST* imaging (e.g. Bahcall et al., 1997; Boyce et al., 1998; Dunlop et al., 2003; Hooper et al., 1997; McLeod and McLeod, 2001). At low redshifts ($z \lesssim 0.5$), luminous quasars appear to reside in a wide variety of galaxies, with Boyce et al. (1998) finding five of the seven quasars in their sample (*radio loud*) to reside in luminous elliptical galaxies, with the remaining two (*radio quiet*) having disc-like hosts. The conclusions of this work appear broadly consistent with that of Bahcall et al. (1997), who also find luminous quasars to reside in both luminous ellipticals and spiral or elliptical hosts depending on whether or not the quasar is radio loud.

More recently, Bennert et al. (2011) successfully modelled a sample of 11 quasar hosts at higher redshifts ($1 < z < 2$), making use of very deep, multi-band *HST* imaging from GOODS. Their work utilises the Surface Photometry and Structural Modelling of Imaging Data (SPASMOID) code, which unlike other astronomical image fitting software (e.g. GALFIT; Peng et al. (2002)) allows for the multi-band analysis of surface brightness models, which has been shown to greatly improve the modelling of these quasar hosts. From the modelling, Bennert et al. (2011) find approximately a third of their quasar sample to reside in spiral systems with no evidence for significant interactions or recent merger activity in any of the galaxies studied. This work therefore concludes that secular evolution and minor mergers play a significant role in growing black holes at $1 < z < 2$.

At higher redshifts and among populations of reddened quasars, several studies suggest the most luminous quasars to require major mergers (e.g. Urrutia et al., 2008) although this remains disputed (Villforth et al., 2016). Already in Chapter 2, we have modelled a population of reddened quasar hosts using a range of SED templates, concluding prodigious rates of star formation in these systems, consistent with them being in a star-forming phase. Here, we now seek to model a subset of the z∼2 reddened quasar sample outlined in Chapter 2 in 2D, exploiting both dust obscuration and multi-band modelling techniques (e.g. Bennert et al., 2011) to infer properties of the host galaxies in our sample. The primary aim of this study is to test whether 2D surface photometry can be successfully applied to current ground-based observations of high-luminosity quasar hosts at z∼2.

The aim of this chapter is to model (in 2D) the restframe UV emission tracing ongoing star formation in a sample of 14 reddened quasars imaged with DES. These systems have been selected to lie at at z$\sim$2 - a peak epoch of star formation and black hole accretion - and therefore trace an interesting phase in quasar-galaxy coevolution. The chapter is structured as follows; Section 3.2 outlines the sample of quasars considered in the study, with the functionality of the modelling code and the methods implemented outlined in Section 3.3. Results are presented in Section 3.4 and compared with the results of Chapter 2. In Section 3.5 we discuss the reliability of the results in Section 3.4, with our final conclusions presented in Section 3.5.4.

3.2 DATA

The reddened quasars considered in this chapter are a subsample of the 38 NIR-selected, spectroscopically confirmed quasars outlined in Chapter 2. Details of their initial selection and spectroscopic follow-up can be found in Chapter 2 and in the work of Banerji et al. (2015a, 2012). Here, we consider observations from the first three years of DES operations (August 2013 to February 2016) corresponding to the Year 3 Annual 1 (Y3A1) internal data release and the first public data release (DR1) (Abbott et al., 2017). Fourteen of the reddened quasars outlined in Chapter 2 fall within the DES Y3A1 footprint, covering $\sim$5000deg^2 of the southern sky. The Y3A1 observations considered in this chapter are typically deeper than Y1A1, making these observations more suitable for probing the 2D structure of the faint galaxy emission in our sample, thought to arise from star formation in the host (see Chapter 2 for details). Table 3.1 details the 14 sources forming the sample of reddened quasars considered throughout this chapter. Table 3.2 denotes the effective wavelength of each passband, $\lambda_{\rm eff}$, along with the 10σ limiting magnitudes reached by the Y3A1 data in a 2 arcsec diameter aperture. The typical seeing in each band is also shown in Table 3.2, where the quoted seeing is taken to be the mean across our sample, with uncertainties given by the standard deviation of these values. All DES Y3A1 observations considered here have a pixel scale of 0.263 arcsec per pixel, corresponding to physical scales $\sim$2kpc per pixel at z = 2.

Table 3.1 Summary of the quasar sample considered in this chapter, with z derived from the VLT spectral follow-up observations presented in Banerji et al. (2015a, 2012).

Name	RA	Dec	z
ULASJ0016-0038	4.0025	-0.6498	2.194
VHSJ2024-5623	306.1074	-56.3898	2.282
VHSJ2028-5740	307.2092	-57.6681	2.121
VHSJ2115-5913	318.8817	-59.2188	2.115
ULASJ2200+0056	330.1036	0.9346	2.541
VHSJ2220-5618	335.1398	-56.3106	2.220
ULASJ2224-0015	336.0392	-0.2566	2.223
VHSJ2227-5203	336.9491	-52.0582	2.656
VHSJ2235-5750	338.9331	-57.8371	2.246
VHSJ2257-4700	344.2589	-47.0156	2.156
VHSJ2306-5447	346.5010	-54.7882	2.372
ULASJ2315+0143	348.9842	1.7307	2.560
VHSJ2332-5240	353.0387	-52.6780	2.45
VHSJ2355-0011	358.9394	-0.1893	2.531

Table 3.2 The effective wavelengths ($\lambda_{\rm eff}$) and 10σ limiting magnitudes reached by the Y3A1 data in a 1.95 arcsec diameter aperture.

Filter	$\lambda_{\rm eff}$ (Å)	Magnitude Limit (10σ; AB)	Average Seeing (arcsec)
g	4824	24.33	1.25±0.11
r	6432	24.08	0.92±0.04
i	7806	23.44	0.86±0.04
z	9179	22.69	0.84±0.10

3.3 METHODS

Throughout this chapter, we seek to perform 2D surface photometry on the 14 reddened quasars outlined in Section 3.2 with an aim to separate the galaxy emission from that of the quasar in the image. Ultimately, we strive to measure properties of reddened quasar hosts in 2D based on ground-based observations from DES Y3A1. Due to the large dynamic range in flux across the DES *griz* bands in our images, we opt to use a multi-band fitting method to model the galaxy and quasar components of the images, similar to that of the SPASMOID code used in Bennert et al. (2011). The primary advantage of this method over using other modelling software such as GALFIT (Peng et al., 2002), is the ability to simultaneously model each band of the image, allowing the galaxy and quasar components of the image to be constrained by the bands in which they dominate. The galaxy, for example, is largely constrained by the *g*-band emission in our heavily reddened quasar population, where the contrast of the galaxy to the quasar emission is highest. It makes sense therefore to use this band to constrain the galaxy in the fitting, whilst constraining the quasar emission in the redder bands where it begins to dominate the emission. In theory, this should improve our ability to disentangle the galaxy and quasar components in the image, potentially overcoming some of the hurdles relating to galaxy and quasar separation outlined by McLeod and Rieke (1995).

The modelling code used throughout this chapter implements a Parallel-Tempering Ensemble Markov Chain Monte-Carlo (PTMCMC) method (Foreman-Mackey et al., 2013; Hastings, 1970; Metropolis et al., 1953) to explore the parameter space. The primary advantage to using this method over the standard MCMC sampling used in Chapter 2 is its handling of multi-model posteriors. Instead of a single likelihood function, PTMCMC creates multiple realisations of the likelihood at different 'temperatures'. At hotter 'temperatures' the likelihood is flatter and broader, allowing the walkers to move easily across the entire parameter space and thus locate the global maximum of the function. At the same time, the colder 'temperatures' allow the peaks of the likelihood function to be explored in detail, finding local solutions. In this way, PTMCMC sampling can dramatically improve the

convergence of the fitting. As with the MCMC fitting routine implemented in Chapter 2, PTMCMC also returns full posterior distributions for all free parameters and marginalises over nuisance parameters in the fitting. Flat priors are invoked throughout.

Each of the models created for our sample consist of two components: a galaxy and a quasar. The galaxy component is modelled by a Sérsic profile with a given index, n. Typically, $n = 1$ is used to parametrise a diffuse-type galaxy such as a dwarf elliptical or discy galaxy, whilst $n = 4$ (often refered to as *de Vacouleurs* profile) is typical of a more compact elliptical galaxy. The quasar component is modelled with a PSF, given by a nearby star in the image, selected to be unsaturated across all bands in the image. The free parameters in the fitting are set as follows;

- (X,Y) - The position of the centre of the galaxy and the quasar given as (x,y) pixel co-ordinates, each ranging from 0 to the size of the image
- R_{eff} - The effective radius of the galaxy, ranging from 0.3 to 20 pixels in the fitting
- q_{GAL} - The axis ratio (b/a) of the galaxy, where a and b denote the semi-major and semi-minor axes respectively, ranging from 0.2 to 1.
- θ - The angle of orientation relative to the image plane, ranging from -100 to 100°
- n - The Sérsic index of the galaxy, ranging from 0.5 to 6 in the fitting

The magnitudes of the galaxy and quasar components are also free to vary in the fitting, providing another two free parameters in each of the *griz* bands for a total of 14 parameters. In order for an object to be detected, we expect a minimum of 4 pixels detected at $>1\sigma$ significance and thus we place lower (fainter) limits on the magnitude of 4σ, where σ is the noise level in the image. Upper (brighter) limits on the magnitudes are selected as to not restrict the model and as such are fixed at 16 mags in each band - far brighter than expected from either the quasar or galaxy component in any object in our sample.

3.4 RESULTS

3.4.1 MODELLING DUSTY QUASAR HOSTS

Each of the 14 dusty quasars in our DES Y3A1 sample are modelled with the code described in Section 3.3. We check for convergence in the fitting, finding well-converged solutions for all 14 galaxies in our sample. To test the goodness of fit of the resulting models, we plot the (data-model) residuals, found by subtracting the best-fit model from the original DES image in each of the *griz* bands. Fig 3.1 shows the *giz* colour residuals for the brightest galaxy in our sample - ULASJ2200+0056 [1]. Small residuals indicate the model is a good fit to the data and indeed the residuals in 13 of the 14 quasars in our sample lie within the noise expected from the image. In the DES image of the remaining object (VHSJ2332-5240), we see two galaxies (Fig. 3.2). For this system we do not return residuals consistent with the noise of the image, as only one of the galaxies is modelled in the fitting. Although fitting multiple systems in a single image lies beyond the scope of this chapter, we note that introducing this feature could potentially resolve the issue seen in the modelling of VHSJ2332-5240 and would therefore be an interesting extension to this study. For now however, we opt to exclude VHSJ2332-5240 from the remainder of our analysis, reducing our full DES Y3A1 sample to 13 reddened quasars at z$\sim$2.

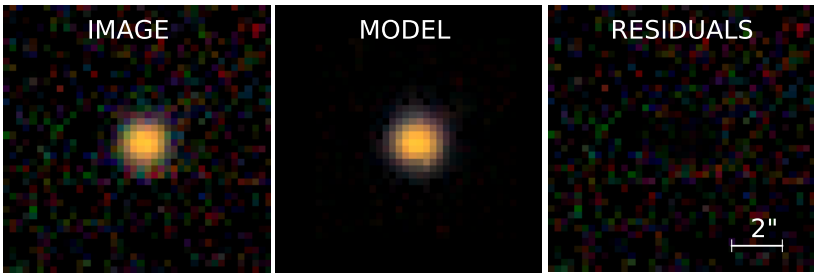

Fig. 3.1 Example of (data-model) residual plot for one object in our sample - ULASJ2200+0056 - shown as a *g* (*blue*), *i* (*green*), *z* (*red*) colour image. Residuals appear consistent with the noise level of the image in 13 objects in our sample.

Having derived best-fit galaxy + quasar models for 13 of the 14 quasars in our sample, we now infer properties of each galaxy. Specifically, we infer the position of the galaxy and

[1] The full set of residual plots for the sample are given in Fig. B.1 (*appendix*)

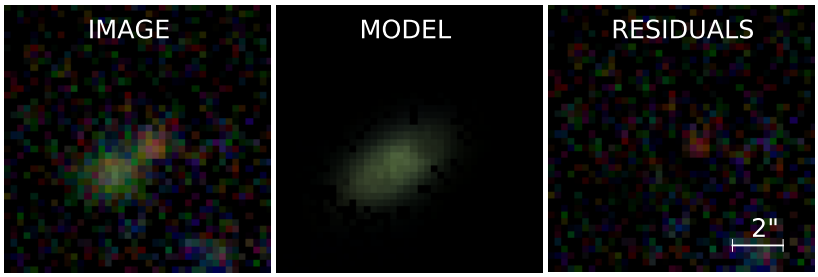

Fig. 3.2 Example of (data-model) residual plot for one object in our sample - VHSJ2332-5240 - shown as a *g* (*blue*), *i* (*green*), *z* (*red*) colour image. *Left panel*: Two galaxies are seen in the image. *Right panel*: Residuals are inconsistent with the noise in the image, indicating the model is a poor fit to the data.

quasar components (X,Y), the effective radius of the host (R_{eff}), the axis ratio of the galaxy (q), its orientation angle (θ), the Sérsic index (n) and the magnitudes of the individual galaxy and quasar components in each band (m_{qso}, m_{gal}). Across the full sample, the modelling code generally places constraints on these parameters, shown by well-defined contour regions in the returned 1D and 2D parameter solutions. An example of the returned parameter constraints is given for the brightest galaxy in our sample (ULASJ2200+056) in Fig. 3.3, with the full set of results given in Fig. B.2 (*appendix*). Along with the well-converged parameter solutions, Fig. 3.3 also illustrates the strong degeneracy between the quasar and galaxy magnitudes returned in each band, showing that a brighter inference on the galaxy typically results in a fainter inference on the quasar and vice versa. We note that this degeneracy appears strongest in systems with a low inferred galaxy radius, perhaps indicating that our ability to separate the galaxy and quasar components in these images decreases as we approach small radii ($\lesssim$2 pixels).

Whilst the returned quasar magnitudes for ULASJ2200+0056 are well-constrained across all bands in Fig. 3.3, the *z*-band magnitude of the galaxy component hits the upper bound of the prior in the fitting. Although this is perhaps expected, given that light from the quasar dominates the *z*-band emission, it means we are unable to constrain the *z*-band galaxy magnitude for ULASJ2200+0056 from the fitting. In cases such as this, we instead derive statistical 95 per cent confidence limits on the magnitude. We further note that the galaxy magnitude inferred from the model of ULASJ2200+0056 (Fig. 3.3) results in an unrealistic (*i*-*z*) colour for the galaxy. This potentially indicates that the 2D modelling is inferring some

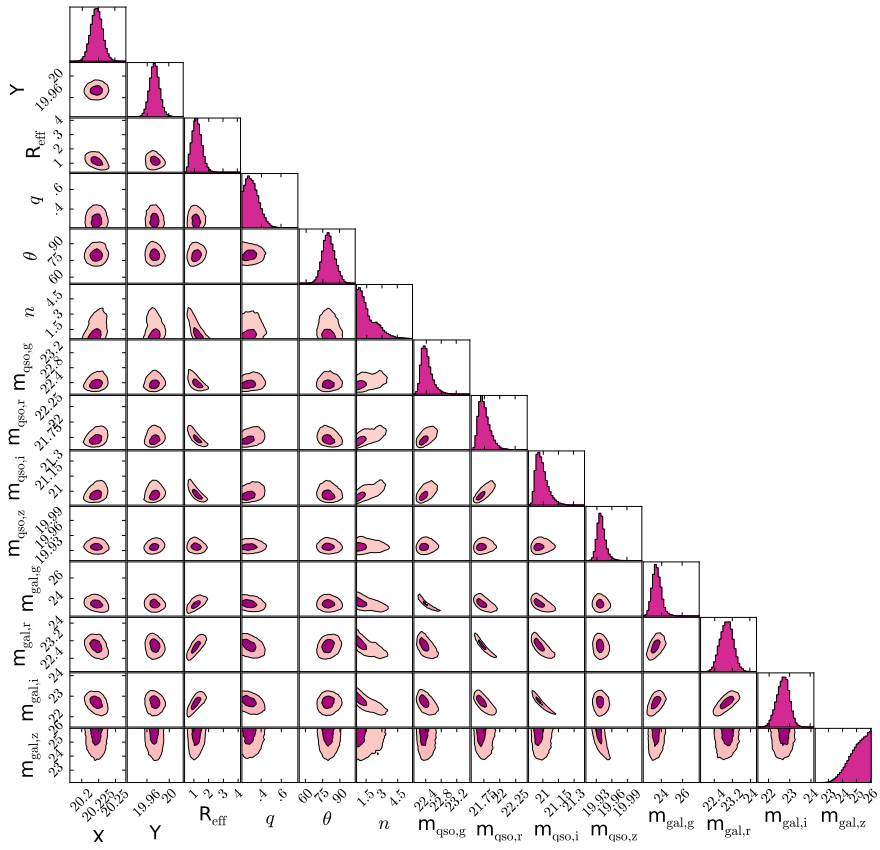

Fig. 3.3 1D and 2D parameter solutions for ULASJ2200+0056. Shaded contours denote the 68 and 95 per cent confidence limits on the returned parameter solutions.

fraction of the galaxy light to belong to the quasar component in the image and thus may indicate that the PSF used in the fitting is imperfect, causing the modelling to 'correct' for this by incorporating additional flux from the galaxy. This may also explain the reason why R_{eff} is effectively unconstrained by the fitting for several quasars in the sample (Fig. B.2 - *appendix*). Again, the lack of constraint on R_{eff} likely indicates the underlying difficulty in separating the quasar and galaxy emission, particularly if the galaxy model is indeed being used to correct for an imperfect PSF in the model as suggested. Similarly, Fig. 3.3 shows n, to hit the lower bound of the fitting in ULASJ2200+0056, meaning this value is also unconstrained by the data and may also be an idication that the galaxy and quasar components in the image are not being robustly separated in the fitting.

Another possible reason for the poor constraints on R_{eff} and n may be that the quasar is slightly offset from the centre of the galaxy. In the fitting, we have assumed the the position of both the quasar and galaxy are the same (a common assumption made by numerous other morphological studies (e.g. Bennert et al., 2011), but this may not be the case in reality. On the one hand, if the quasar were to be offset from the centre of the galaxy in the image, the model could potentially try and correct for this in the fitting by altering the galaxy profile. On the other hand, the galaxy and quasar components may prove easier to disentangle, as there would be less degeneracy between the bright centre of the Sérsic profile and the quasar itself. Whilst introducing this extra degree of freedom into the modelling is beyond the scope of this chapter, particularly with the limited data available, we note that the introduction of this extra parameter may improve our ability to model the more spatially resolved data in the future. Despite the lack of constraint on the value of n and, in some case R_{eff}, our ability to recover these parameters does not appear to affect our ability to recover other galaxy parameters from the model. Later, In Section 3.5.4 we discuss the benefits of incoporating priors based on the SED fitting in Chapter 2

3.4.2 RECOVERING GALAXY AND QUASAR MAGNITUDES

A key goal of this chapter is to compare the inferences of the 2D surface photometry to the results of Chapter 2, where the magnitude of the host galaxy is constrained by a 'best-fit' SED template. The following section directly compares the galaxy and quasar magnitudes in each of the *griz* bands, inferred from each fitting method. We begin by deriving magnitudes based on the galaxy SED templates for the 13 objects for which we also fit 2D models (Section 3.4.1). These magnitudes are calculated by integrating the 'best-fit' galaxy SED template from Chapter 2 over a given passband and are given in Table 3.3. Similarly, the quasar magnitudes are calculated from the 'best-fit' quasar SED, integrated over each of the *griz* bands (Table 3.4). Tables 3.5 and 3.9 detail the corresponding galaxy and quasar magnitudes derived from the 2D surface photometry, calculated to be the median converged model solution, with the uncertainties denoting the 68 per cent confidence bounds on these magnitudes.

Table 3.3 Galaxy magnitudes in each of the DES *griz* bands derived from the results of the SED fitting (Chapter 2). Quoted errors denote the 1σ uncertainties on the normalisation of the galaxy SED template in the fitting.

Name	$g_{\rm GAL}$	$r_{\rm GAL}$	$i_{\rm GAL}$	$z_{\rm GAL}$
ULASJ0016-0038	$24.33^{+0.36}_{-0.43}$	$24.00^{+0.36}_{-0.43}$	> 23.06	> 22.69
VHSJ2024-5623	> 24.33	> 24.08	> 23.44	> 22.69
VHSJ2028-5740	$23.83^{+0.14}_{-0.16}$	$23.51^{+0.14}_{-0.16}$	$23.43^{+0.14}_{-0.16}$	> 22.69
VHSJ2115-5913	$22.58^{+0.20}_{-0.18}$	$22.26^{+0.20}_{-0.18}$	$22.18^{+0.20}_{-0.18}$	> 21.63
ULASJ2200+0056	$22.27^{+0.14}_{-0.13}$	$21.89^{+0.14}_{-0.13}$	$21.73^{+0.14}_{-0.13}$	$21.66^{+0.14}_{-0.13}$
VHSJ2220-5618	$23.54^{+0.10}_{-0.09}$	$23.21^{+0.10}_{-0.09}$	$23.12^{+0.10}_{-0.09}$	> 22.69
ULASJ2224-0015	$23.82^{+0.12}_{-0.12}$	$23.49^{+0.12}_{-0.12}$	$23.41^{+0.12}_{-0.12}$	> 22.69
VHSJ2227-5203	$23.98^{+0.15}_{-0.14}$	$23.61^{+0.15}_{-0.14}$	$23.40^{+0.15}_{-0.14}$	> 22.69
VHSJ2235-5750	$23.36^{+0.12}_{-0.11}$	$23.03^{+0.12}_{-0.11}$	$22.94^{+0.12}_{-0.11}$	> 22.56
VHSJ2257-4700	> 24.33	> 24.08	> 23.44	> 22.69
VHSJ2306-5447	> 24.15	$24.02^{+0.13}_{-0.12}$	> 23.44	> 22.69
ULASJ2315+0143	$22.80^{+0.87}_{-0.50}$	$22.42^{+0.87}_{-0.50}$	$22.25^{+0.87}_{-0.50}$	$22.19^{+0.87}_{-0.50}$
VHSJ2355-0011	$22.80^{+0.16}_{-0.15}$	$22.42^{+0.16}_{-0.15}$	$22.26^{+0.16}_{-0.15}$	$22.20^{+0.16}_{-0.15}$

Table 3.4 Quasar magnitudes in each of the DES *griz* bands derived from the results of the SED fitting (Chapter 2). Quoted errors denote the statistical 68 per cent confidence bounds on the normalisation of the galaxy SED template in the fitting.

Name	$g_{\rm QSO}$	$r_{\rm QSO}$	$i_{\rm QSO}$	$z_{\rm QSO}$
ULASJ0016-0038	$23.47^{+0.36}_{-0.43}$	$22.30^{+0.36}_{-0.43}$	$21.32^{+0.36}_{-0.43}$	$20.51^{+0.36}_{-0.43}$
VHSJ2024-5623	> 24.33	$23.92^{+0.57}_{-0.55}$	$22.65^{+0.57}_{-0.55}$	$21.69^{+0.57}_{-0.55}$
VHSJ2028-5740	> 24.33	> 24.08	> 23.17	$21.98^{+0.14}_{-0.16}$
VHSJ2115-5913	> 24.33	> 24.08	> 23.24	$22.14^{+0.20}_{-0.18}$
ULASJ2200+0056	$23.87^{+0.14}_{-0.13}$	$22.35^{+0.14}_{-0.13}$	$21.23^{+0.14}_{-0.13}$	$20.18^{+0.14}_{-0.13}$
VHSJ2220-5618	> 24.33	> 24.08	$22.39^{+0.10}_{-0.09}$	$20.87^{+0.10}_{-0.09}$
ULASJ2224-0015	> 24.33	$23.71^{+0.12}_{-0.12}$	$22.31^{+0.12}_{-0.12}$	$21.19^{+0.12}_{-0.12}$
VHSJ2227-5203	> 24.33	> 24.05	$23.19^{+0.15}_{-0.14}$	$22.09^{+0.15}_{-0.14}$
VHSJ2235-5750	> 24.33	$23.90^{+0.12}_{-0.11}$	$22.37^{+0.12}_{-0.11}$	$21.26^{+0.12}_{-0.11}$
VHSJ2257-4700	> 24.33	$24.01^{+0.78}_{-0.65}$	$22.62^{+0.78}_{-0.65}$	$21.55^{+0.78}_{-0.65}$
VHSJ2306-5447	> 24.33	> 24.08	$23.28^{+0.13}_{-0.12}$	$21.98^{+0.13}_{-0.12}$
ULASJ2315+0143	> 24.33	> 24.08	> 23.44	> 22.69
VHSJ2355-0011	> 24.33	> 24.08	> 23.44	$22.52^{+0.16}_{-0.15}$

The galaxy and quasar magnitudes returned from each modelling method are directly compared in Figs. 3.4 and 3.5 respectively. In cases where either the 2D surface photometry or the SED fitting does not return a well-constrained magnitude (e.g. the magnitude returned from the SED fitting lies below the survey depths in Table 3.2 or the 2D modelling hits the upper bound of the prior), returned magnitudes are instead given as 95 per cent confidence limits, denoted as arrows in Figs. 3.4 and 3.5. Fig. 3.4 shows the *g*-band galaxy magnitudes are constrained for ten of the 13 galaxies in the sample, with just three objects returning

Table 3.5 Galaxy magnitudes and associated 68 per cent confidence bounds returned in each band from the 2D modelling. Where magnitudes are not constrained by the model, 95 per cent confidence limits are instead presented.

Name	g_{GAL}	r_{GAL}	i_{GAL}	z_{GAL}
ULASJ0016-0038	$23.17^{+0.06}_{-0.05}$	$23.26^{+0.65}_{-0.38}$	> 24.78	> 23.67
VHSJ2024-5623	$21.38^{+0.09}_{-0.14}$	$23.35^{+1.59}_{-0.71}$	> 24.07	> 23.96
VHSJ2028-5740	$23.52^{+0.34}_{-0.41}$	$24.33^{+1.20}_{-0.73}$	>22.89	> 23.99
VHSJ2115-5913	$24.03^{+1.52}_{-0.67}$	> 22.68	$23.03^{+1.18}_{-0.76}$	$21.77^{+0.51}_{-0.29}$
ULASJ2200+0056	$23.47^{+0.38}_{-0.34}$	$22.92^{+0.29}_{-0.27}$	$22.66^{+0.28}_{-0.27}$	> 23.92
VHSJ2220-5618	$23.50^{+0.20}_{-0.22}$	$22.91^{+0.14}_{-0.16}$	$22.34^{+0.12}_{-0.13}$	$22.20^{+0.23}_{-0.22}$
ULASJ2224-0015	> 23.81	> 24.06	> 23.91	> 23.86
VHSJ2227-5203	$23.72^{+0.57}_{-0.41}$	$24.83^{+1.76}_{-0.95}$	$22.43^{+0.29}_{-0.31}$	> 22.83
VHSJ2235-5750	$21.24^{+0.13}_{-0.08}$	$21.27^{+0.13}_{-0.12}$	$21.51^{+0.21}_{-0.15}$	$21.84^{+0.34}_{-0.29}$
VHSJ2257-4700	$22.46^{+0.11}_{-0.13}$	$21.44^{+0.08}_{-0.07}$	$21.02^{+0.10}_{-0.09}$	$20.94^{+0.13}_{-0.11}$
VHSJ2306-5447	$23.26^{+0.28}_{-0.28}$	> 24.70	> 24.50	> 23.94
ULASJ2315+0143	$21.67^{+0.21}_{-0.16}$	$21.92^{+0.25}_{-0.23}$	$22.62^{+1.10}_{-0.52}$	> 21.89
VHSJ2355-0011	$22.73^{+0.30}_{-0.20}$	$22.21^{+0.18}_{-0.21}$	$21.94^{+0.28}_{-0.28}$	$21.90^{+0.56}_{-0.40}$

Table 3.6 Returned quasar magnitudes and associated 68 per cent confidence bounds returned in each band from the 2D modelling. Where magnitudes are not constrained by the model, 95 per cent confidence limits are instead presented.

Name	g_{QSO}	r_{QSO}	i_{QSO}	z_{QSO}
ULASJ0016-0038	> 25.90	$22.15^{+0.16}_{-0.16}$	$21.24^{+0.02}_{-0.01}$	$20.46^{+0.02}_{-0.02}$
VHSJ2024-5623	$24.80^{+0.54}_{-0.36}$	$23.53^{+0.10}_{-0.10}$	$22.37^{+0.02}_{-0.03}$	$21.39^{+0.03}_{-0.03}$
VHSJ2028-5740	> 24.93	$23.74^{+0.24}_{-0.14}$	$22.70^{+0.07}_{-0.06}$	$21.69^{+0.04}_{-0.03}$
VHSJ2115-5913	$22.84^{+0.29}_{-0.13}$	$22.45^{+0.15}_{-0.07}$	$22.35^{+0.66}_{-0.22}$	$22.00^{+0.72}_{-0.35}$
ULASJ2200+0056	$22.39^{+0.17}_{-0.09}$	$21.74^{+0.10}_{-0.07}$	$20.98^{+0.06}_{-0.05}$	$19.94^{+0.01}_{-0.01}$
VHSJ2220-5618	$24.34^{+0.51}_{-0.27}$	$23.82^{+0.41}_{-0.18}$	$22.32^{+0.13}_{-0.09}$	$20.76^{+0.04}_{-0.03}$
ULASJ2224-0015	$23.62^{+0.17}_{-0.09}$	$22.91^{+0.07}_{-0.04}$	$21.76^{+0.03}_{-0.02}$	$20.87^{+0.01}_{-0.01}$
VHSJ2227-5203	$24.07^{+0.09}_{-0.08}$	$23.16^{+0.04}_{-0.03}$	$22.41^{+0.03}_{-0.02}$	$21.27^{+0.02}_{-0.02}$
VHSJ2235-5750	$23.34^{+0.08}_{-0.07}$	$22.96^{+0.05}_{-0.06}$	$22.10^{+0.03}_{-0.03}$	$21.06^{+0.02}_{-0.01}$
VHSJ2257-4700	> 26.43	$24.42^{+0.12}_{-0.10}$	$22.60^{+0.04}_{-0.04}$	$21.51^{+0.03}_{-0.02}$
VHSJ2306-5447	$24.82^{+0.65}_{-0.31}$	$24.02^{+0.08}_{-0.07}$	$22.65^{+0.04}_{-0.02}$	$21.61^{+0.02}_{-0.02}$
ULASJ2315+0143	> 24.92	$23.75^{+0.25}_{-0.20}$	$23.73^{+0.43}_{-0.30}$	$22.43^{+0.19}_{-0.15}$
VHSJ2355-0011	$22.54^{+0.02}_{-0.02}$	$22.70^{+0.03}_{-0.03}$	$22.41^{+0.03}_{-0.03}$	$21.72^{+0.03}_{-0.02}$

upper limits on the magnitude from either the 2D modelling or SED fitting in this band. In the z-band however, the rate of returned galaxy magnitudes drops to just three, with ten galaxies returning upper limits on the magnitude from either the 2D modelling or the SED fitting, six of which return limits from both methods. The lack of returned galaxy magnitudes in the redder bands implies the galaxy component is largely constrained at bluer wavelengths (i.e. in the g- and r-bands), consistent with the conclusions of the SED fitting in Chapter 2

where galaxy emission is seen to dominate in the bluer bands. The opposite trend is observed for the quasar magnitudes in Fig. 3.5, with all but one source (ULASJ2315+0143) returning constrained quasar magnitudes in the z-band via both fitting methods. In the g-band, quasar magnitudes are returned only for a single object (VHSJ2200+0056) with the remaining 12 models returning limits on the quasar magnitudes from one or both of the fitting methods. Again, this is consistent with our expectation from the SED fitting in Chapter 2, where emission from the quasar is largely constrained by the z-band photometry.

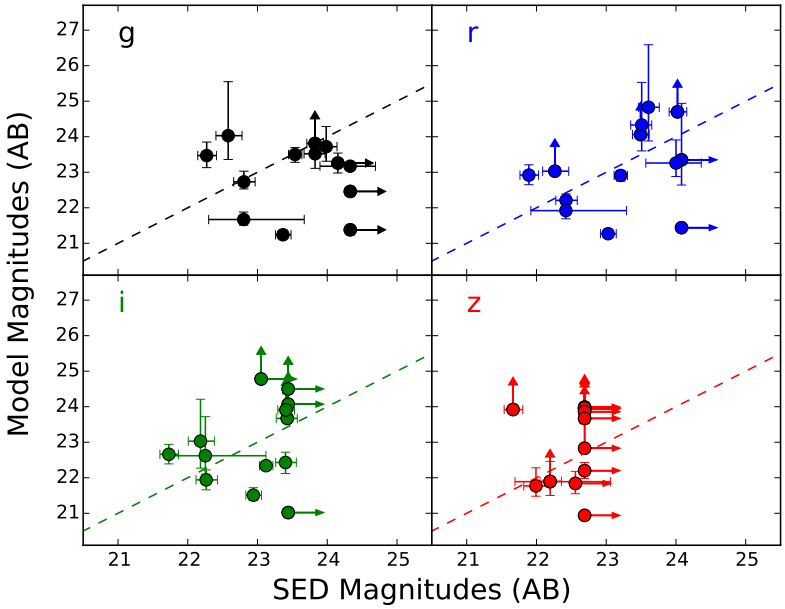

Fig. 3.4 Returned galaxy magnitudes in each band from the 2D surface photometry compared to those returned from the SED fitting in Chapter 2. Arrows denote the 95 per cent upper limits on the galaxy magnitudes.

Overall, we see a similar trend between the galaxy and quasar magnitudes returned via each method, with brighter galaxies and quasars generally appearing bright in both sets of models. In some cases however, Figs. 3.4 and 3.5 show magnitudes to be derived from one method but return limits from the other. When considering the galaxy magnitudes for example (Fig. 3.4), VHSJ2257-4700 appears consistent with having no galaxy component in the SED fitting, returning an upper limit on its galaxy magnitude fainter than the survey limit of DES in every band. The 2D modelling however, suggests a galaxy magnitude for VHSJ2257-4700 brighter than 22.5 mags in all bands, with small uncertainties on this value.

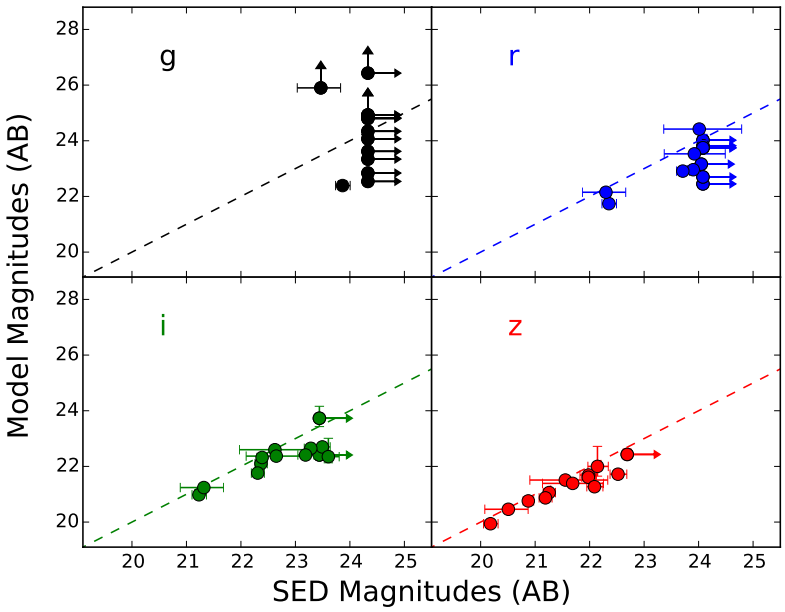

Fig. 3.5 Returned quasar magnitudes in each band from the 2D surface photometry compared to those returned from the SED fitting in Chapter 2. Arrows denote the 95 per cent upper limits on the quasar magnitudes.

Similarly, the quasar magnitudes derived from the SED-fitting of ULASJ2315+0143 - the reddest quasar in our sample - lie below the survey limit in all bands, but are well constrained by the 2D modelling in the *r*-,*i*- and *z*-bands. In both cases, this could indicate that the spatial modelling of the 2D surface photometry provides an extra constraint when separating the galaxy and quasar emission, allowing us to better disentangle the two components in the data. Alternatively, in ULASJ2315+0143 the 2D modelling may be inferring a quasar component that isn't there. If the galaxy is bright enough, the contribution from a faint quasar component will appear negligible in comparison to the overall flux in the image. It is therefore possible that the model may infer a 'quasar' component in order to account for a more compact component of the galaxy, which is not accounted for in the galaxy profile fitted in the model. Later, in Section 3.5.1, we test this idea when modelling local galaxies in DES. It is possible that this effect may be more prominent among galaxies with small R_{eff}.

Although a small fraction of models return galaxy and quasar magnitudes consistent to the SED-derived magnitudes within the quoted 68 per cent confidence bounds, an exact one-to-one correlation is not necessarily expected between the results of the two methods.

Due to the limited photometry available for the sample of reddened quasars in Chapter 2, we are forced to make several assumptions about the shape of the galaxy SED, including the slope (or dust reddening) of the template. The only parameter determining the *griz* magnitudes in the SED fitting is therefore the normalisation of the galaxy model, with the colours of both the galaxy and quasar fixed throughout the fitting. In the 2D modelling however, the colours of each component are not fixed, but rather the magnitudes are free to vary independently in each band, allowing for the galaxy and quasar magnitudes to be solved individually in every band. In some respects, this extra freedom in the fitting may be advantageous, allowing for greater flexibility in the model. On the other hand, the lack of colour constraint in the model means that there is nothing in place to ensure the colours of the fitted galaxy and quasar components are realistic and thus we may infer well-fitting, yet unphysical models. In Section 3.5.4 we discuss how these two methods may be combined to improve the model fitting in future.

Table 3.7 Returned quasar magnitudes and associated 68 per cent confidence bounds returned in each band from the 2D modelling. Where magnitudes are not constrained by the model, 95 per cent confidence limits are instead presented.

Name	X	Y	R_{eff}	q	θ	n
ULASJ0016-0038	$20.89^{+0.02}_{-0.01}$	$19.87^{+0.02}_{-0.01}$	$1.18^{+0.13}_{-0.10}$	$0.73^{+0.17}_{-0.16}$	$-24.66^{+19.94}_{-13.54}$	$0.53^{+0.05}_{-0.02}$
VHSJ2024-5623	$19.92^{+0.03}_{-0.05}$	$20.65^{+0.04}_{-0.04}$	$19.23^{+0.54}_{-1.26}$	$0.55^{+0.22}_{-0.13}$	$69.06^{+14.28}_{-156.46}$	$0.62^{+0.22}_{-0.08}$
VHSJ2028-5740	$21.24^{+0.06}_{-0.04}$	$21.21^{+0.04}_{-0.04}$	$4.96^{+4.34}_{-1.90}$	$0.70^{+0.22}_{-0.25}$	$23.68^{+30.78}_{-50.94}$	$2.62^{+2.01}_{-1.46}$
VHSJ2115-5913	$21.39^{+0.03}_{-0.04}$	$21.05^{+0.05}_{-0.04}$	$2.05^{+3.93}_{-1.18}$	$0.70^{+0.18}_{-0.24}$	$46.62^{+31.71}_{-90.63}$	$4.14^{+1.27}_{-1.88}$
ULASJ2200+0056	$20.22^{+0.01}_{-0.01}$	$19.97^{+0.01}_{-0.01}$	$1.16^{+0.29}_{-0.33}$	$0.29^{+0.08}_{-0.05}$	$78.67^{+5.95}_{-5.76}$	$1.40^{+1.31}_{-0.60}$
VHSJ2220-5618	$19.96^{+0.02}_{-0.03}$	$21.25^{+0.02}_{-0.02}$	$2.76^{+0.31}_{-0.32}$	$0.44^{+0.05}_{-0.06}$	$-40.52^{+3.25}_{-3.42}$	$0.64^{+0.32}_{-0.10}$
ULASJ2224-0015	$20.62^{+0.02}_{-0.02}$	$20.21^{+0.02}_{-0.02}$	$8.64^{+9.16}_{-8.23}$	$0.61^{+0.25}_{-0.31}$	$2.04^{+68.30}_{-64.20}$	$2.55^{+2.44}_{-1.67}$
VHSJ2227-5203	$20.24^{+0.03}_{-0.03}$	$20.28^{+0.02}_{-0.03}$	$16.49^{+2.04}_{-2.68}$	$0.23^{+0.04}_{-0.02}$	$38.33^{+5.41}_{-4.87}$	$0.60^{+0.17}_{-0.07}$
VHSJ2235-5750	$20.25^{+0.02}_{-0.02}$	$20.47^{+0.02}_{-0.02}$	$18.51^{+1.18}_{-1.68}$	$0.30^{+0.06}_{-0.05}$	$-17.85^{+2.67}_{-2.49}$	$1.20^{+0.30}_{-0.28}$
VHSJ2257-4700	$20.05^{+0.04}_{-0.03}$	$20.19^{+0.04}_{-0.04}$	$15.53^{+0.63}_{-0.59}$	$0.20^{+0.00}_{-0.00}$	$38.55^{+0.85}_{-0.62}$	$0.50^{+0.01}_{-0.00}$
VHSJ2306-5447	$20.88^{+0.03}_{-0.03}$	$20.26^{+0.03}_{-0.04}$	$13.49^{+4.46}_{-6.59}$	$0.75^{+0.20}_{-0.28}$	$9.73^{+64.16}_{-78.07}$	$4.02^{+1.36}_{-1.60}$
ULASJ2315+0143	$19.44^{+0.08}_{-0.10}$	$19.68^{+0.12}_{-0.11}$	$13.52^{+3.65}_{-3.93}$	$0.33^{+0.05}_{-0.05}$	$75.64^{+3.63}_{-4.36}$	$4.26^{+1.06}_{-1.11}$
VHSJ2355-0011	$20.76^{+0.03}_{-0.03}$	$21.17^{+0.02}_{-0.03}$	$18.27^{+1.08}_{-1.86}$	$0.21^{+0.02}_{-0.01}$	$46.85^{+2.65}_{-2.96}$	$0.54^{+0.07}_{-0.03}$

Table 3.8

Name	$m_{g,\mathrm{qso}}$	$m_{r,\mathrm{qso}}$	$m_{i,\mathrm{qso}}$	$m_{z,\mathrm{qso}}$
ULASJ0016-0038	26.99 ± 0.52	22.13 ± 0.16	21.24 ± 0.02	20.46 ± 0.02
VHSJ2024-5623	24.91 ± 0.58	23.53 ± 0.10	22.37 ± 0.03	21.39 ± 0.03
VHSJ2028-5740	26.22 ± 0.75	23.79 ± 0.28	22.71 ± 0.08	21.69 ± 0.03
VHSJ2115-5913	22.87 ± 0.18	22.47 ± 0.11	22.40 ± 0.40	22.00 ± 0.40
ULASJ2200+0056	22.42 ± 0.15	21.75 ± 0.09	20.99 ± 0.06	19.94 ± 0.01
VHSJ2220-5618	24.54 ± 0.65	23.96 ± 0.55	22.35 ± 0.14	20.77 ± 0.04
ULASJ2224-0015	23.70 ± 0.30	22.94 ± 0.10	21.77 ± 0.04	20.88 ± 0.03
VHSJ2227-5203	24.07 ± 0.09	23.16 ± 0.04	22.41 ± 0.03	21.27 ± 0.02
VHSJ2235-5750	23.35 ± 0.08	22.97 ± 0.06	22.11 ± 0.03	21.06 ± 0.02
VHSJ2257-4700	27.24 ± 0.49	24.42 ± 0.11	22.60 ± 0.04	21.51 ± 0.02
VHSJ2306-5447	24.99 ± 0.68	24.03 ± 0.08	22.66 ± 0.04	21.61 ± 0.02
ULASJ2315+0143	26.24 ± 0.85	23.79 ± 0.25	23.80 ± 0.40	22.45 ± 0.19
VHSJ2355-0011	22.54 ± 0.02	22.70 ± 0.03	22.41 ± 0.03	21.72 ± 0.03

Table 3.9 Returned quasar magnitudes and associated 68 per cent confidence bounds returned in each band from the 2D modelling. Where magnitudes are not constrained by the model, 95 per cent confidence limits are instead presented.

Name	$m_{g,\mathrm{gal}}$	$m_{r,\mathrm{gal}}$	$m_{i,\mathrm{gal}}$	$m_{z,\mathrm{gal}}$
ULASJ0016-0038	23.17 ± 0.05	23.49 ± 0.69	25.89 ± 0.61	24.87 ± 0.69
VHSJ2024-5623	21.38 ± 0.13	23.66 ± 1.13	25.41 ± 0.84	25.08 ± 0.66
VHSJ2028-5740	23.45 ± 0.41	24.55 ± 1.00	25.05 ± 0.95	25.25 ± 0.70
VHSJ2115-5913	24.35 ± 1.09	24.64 ± 1.07	23.42 ± 1.05	21.90 ± 0.46
ULASJ2200+0056	23.54 ± 0.49	22.94 ± 0.29	22.68 ± 0.30	25.11 ± 0.66
VHSJ2220-5618	23.47 ± 0.20	22.90 ± 0.15	22.34 ± 0.14	22.18 ± 0.20
ULASJ2224-0015	26.06 ± 1.09	25.97 ± 0.89	25.63 ± 0.83	25.23 ± 0.75
VHSJ2227-5203	23.89 ± 0.70	25.02 ± 1.15	22.44 ± 0.35	24.55 ± 1.07
VHSJ2235-5750	21.25 ± 0.11	21.27 ± 0.12	21.52 ± 0.17	21.90 ± 0.41
VHSJ2257-4700	22.47 ± 0.12	21.44 ± 0.08	21.01 ± 0.09	20.95 ± 0.13
VHSJ2306-5447	23.27 ± 0.32	26.30 ± 0.91	25.89 ± 0.81	25.36 ± 0.71
ULASJ2315+0143	21.66 ± 0.18	21.90 ± 0.24	22.81 ± 0.87	23.52 ± 1.13
VHSJ2355-0011	22.75 ± 0.22	22.22 ± 0.21	21.95 ± 0.26	22.05 ± 0.59

3.5 DISCUSSION

The following section aims to test the extent to which we can rely on the results of the 2D model fitting described in Section 3.4. In particular, we seek to test our ability to return properties of the system at a given galaxy and quasar magnitude, allowing us to place constraints on the validity of using the multi-band modelling code with ground-based observations of z $\sim$ 2 quasars

3.5.1 FITTING DES ANALOGUE GALAXIES

We select two local galaxies from the DES Y3A1 catalogues that have optical magnitudes and colours that are broadly representative of the galaxy components in our reddened quasar sample (inferred from the SED-fits in Chapter 2). Specifically, we find a 'bright' galaxy in the DES Y3A1 data with optical magnitudes and colours that are very similar to the brightest host galaxy in our quasar sample - ULASJ2200+0056 - as inferred from the SED fitting. We also select a 'typical' galaxy with magnitudes and colours that match the galaxy properties of VHSJ2235-5750, which is representative of the average properties of the host galaxies in our quasar sample. The selected 'bright' and 'typical' galaxies shall hereafter be referred to as G_{bright} and $G_{typical}$ respectively. Whilst neither galaxy has been selected to contain a quasar, we continue to allow for a quasar component when modelling G_{bright} and $G_{typical}$ in order to directly compare the output with that of our quasar sample. Figs. 3.6 and 3.7 show the *giz* colour residuals for the models fit to G_{bright} and $G_{typical}$. In both cases, we find small (data-model) residuals consistent with the noise in the image, indicating that the model is a good fit to the data.

Furthermore, the 1D and 2D parameter solutions for both the bright and the typical models show good constraints on the position (X,Y), the effective radius (R_{eff}), and the *griz* magnitudes of the galaxy (Figs. 3.8 and 3.9). In both cases, the quasar component of the fitted model appears >2 mags fainter than the galaxy component in the equivalent band, with all inferred quasar magnitudes lying below the 10σ magnitude limit of DES (Table 3.2). Although there is no quasar component in the image, the fact we infer a faint

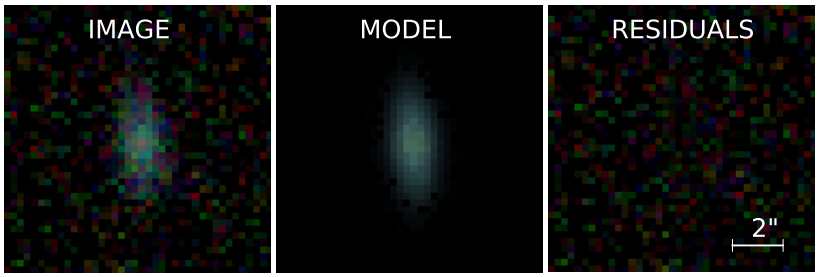

Fig. 3.6 (Data-Model) residuals for the 'bright', low-z analogue galaxy from DES Y3A1 (G_{bright}) shown as a *g* (*blue*), *i* (*green*), *z* (*red*) colour image.

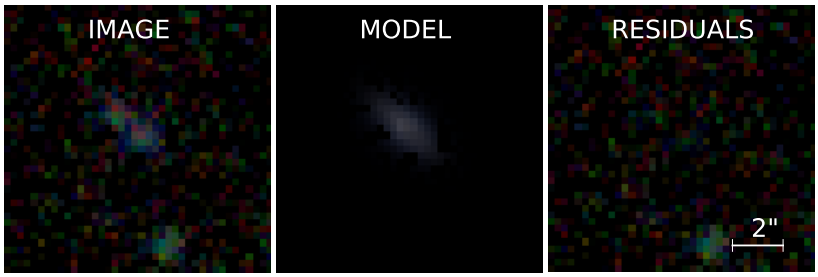

Fig. 3.7 (Data-model) residuals for the 'typical', low-z analogue galaxy from DES Y3A1 $G_{typical}$ shown as a *g* (*blue*), *i* (*green*), *z* (*red*) colour image.

quasar component supports the idea that a small fraction of the galaxy flux is being falsely attributed to a quasar component in the image, as discussed in Section 3.4. We now seek to use the results from this section as a basis to test the impact of including a quasar component on our ability to return certain properties of the galaxy. In this way, we aim to place limits on the effectiveness of the modelling software on parameterising z $\sim$ 2 quasar hosts in ground-based data.

3.5.2 FITTING DES ANALOGUE GALAXIES WITH QUASAR COMPONENT

Having established the 2D modelling to return well-constrained parameters for local galaxies in DES, we now test whether the fitting can return the same parameter values when a quasar component is introduced in the image. As in Section 3.5.1, we consider the two galaxies with colours similar to a 'bright' and a 'typical' example from our sample, hereafter denoted as G_{bright} and $G_{typical}$ respectively. For each of these galaxies, we create a quasar component from the PSF, selected to be a nearby star in the image. As outlined in Section 3.3, stars

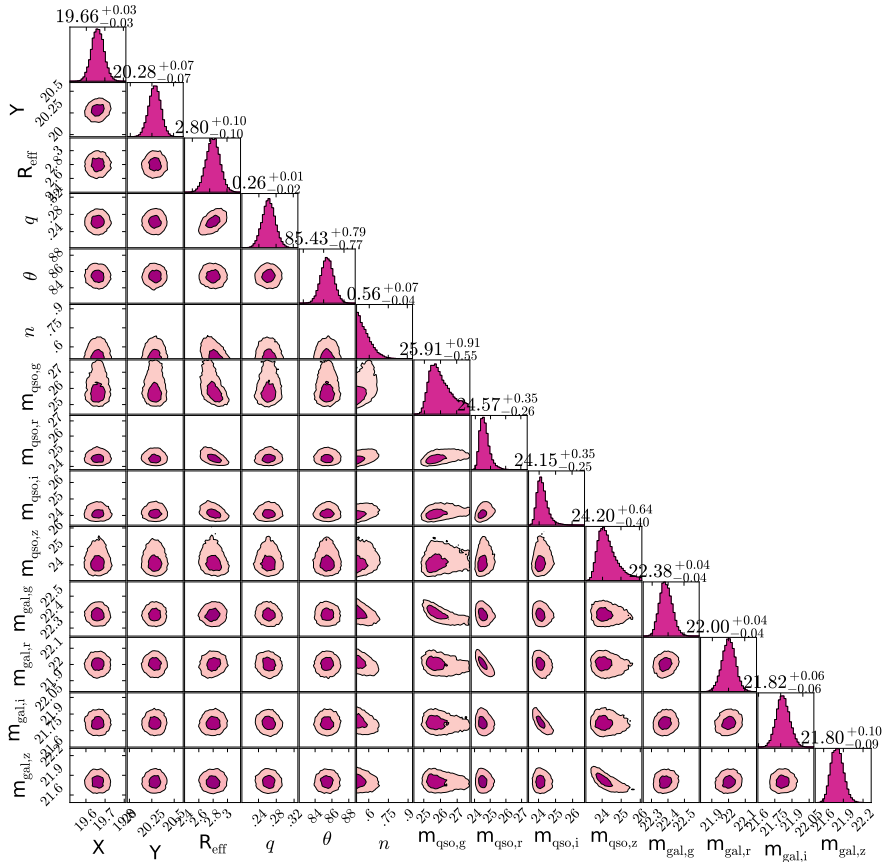

Fig. 3.8 1D and 2D parameter solutions for the 'bright', low-z analogue galaxy in DES Y3A1.

are selected to be unsaturated across all bands of the image. The PSF for each galaxy is normalised and scaled by a factor

$$f_{scale} = 10^{\frac{30-m_{\rm AB}}{2.5}}, \tag{3.1}$$

where m_{AB} is the desired quasar magnitude in each band and 30.0 is the zeropoint of the DES images used in this work. In this way, we create seven distinct quasars with magnitudes spanning the full range of our sample (Table 3.10) and colours chosen to be representative of those derived from the SED-fitting. CASE 4 represents a quasar of 'typical' brightness from our sample. In each of the images, the quasar is set to lie directly atop the galaxy and thus its position is fixed to match the inferences on X and Y from the galaxy modelling (Section 3.5.1). To create the composite images, each of the simulated quasars are summed

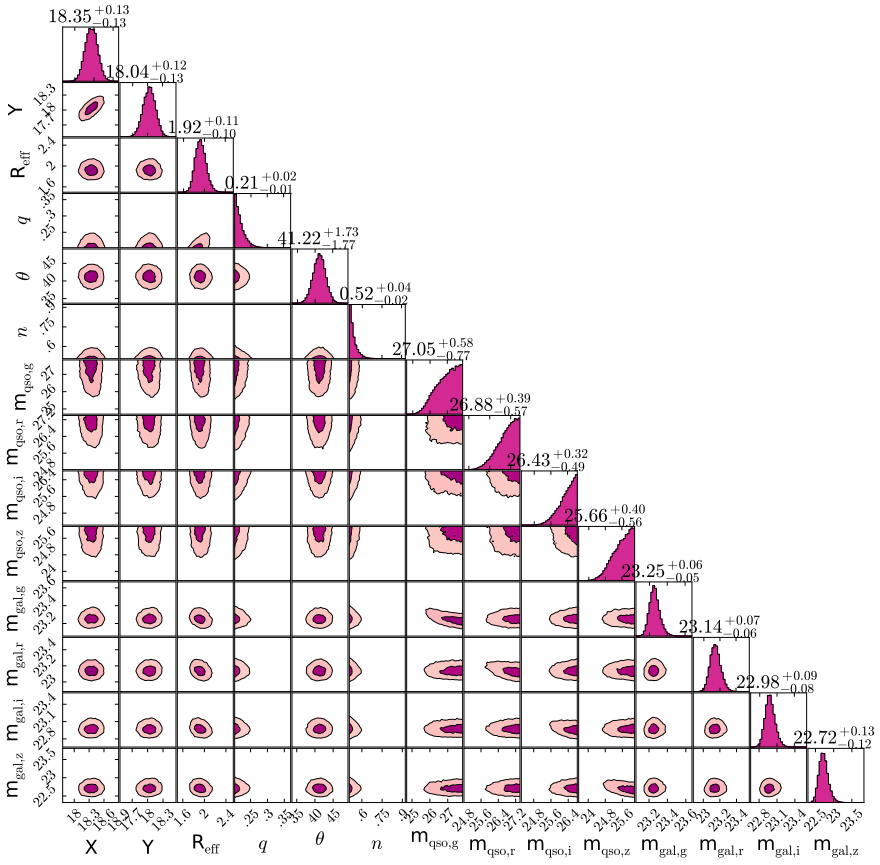

Fig. 3.9 1D and 2D parameter solutions for the 'typical', low-z analogue galaxy in DES Y3A1.

together with the original galaxy. The new images including the simulated quasar component are modelled across the *griz* bands, with all 14 parameters set to vary within the boundary conditions outlined in Section 3.4.1. The returned galaxy magnitudes for G_{bright} and $G_{typical}$ in each band are shown in Figs. 3.10 and 3.11 respectively, where they are directly compared to the values returned from the modelling of the corresponding galaxy (prior to the addition of the quasar component), denoted by the dotted lines in Figs. 3.10 and 3.11.

The galaxy magnitudes returned from the fitting of G_{bright} (Fig. 3.10) are consistent with those predicted from the galaxy-only fitting in Section 3.5.1 across all CASES. Based on this, we expect to robustly recover the galaxy magnitudes for the full range of quasars in our sample, provided the host galaxy is sufficiently bright. We have seen in Chapter 2 that the contrast between the quasar and the host galaxy is largest in the g-band in our obscured quasar sample. Considering the analogue galaxy $G_{typical}$, we find that robust *g*-band magnitudes

Table 3.10 Quasar magnitudes in each band for the quasars added to the DES images. Quasar colours chosen to be representative of those seen in real data, covering the full range of quasar magnitudes in our sample. CASE 4 represents a typical quasar in our sample.

Case Number	g-band	r-band	i-band	z-band
1	29.0	27.0	25.5	24.3
2	28.0	26.0	24.5	23.3
3	27.0	25.0	23.5	22.3
4	26.0	24.0	22.5	21.3
5	25.0	23.0	21.5	20.3
6	24.0	22.0	20.5	19.3
7	23.0	21.0	19.5	18.3

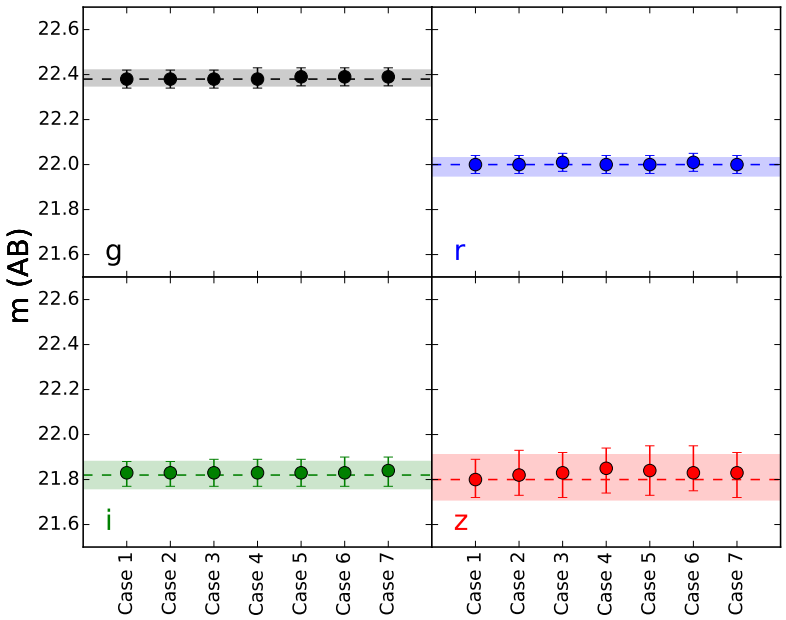

Fig. 3.10 Returned galaxy magnitudes in each band for the bright local DES analogue galaxy (G_{bright}) compared to the galaxy magnitude returned from the galaxy-only fit (*dotted line*). Shaded regions and error bars denote the statistical 68 per cent confidence bounds on the values returned from the fitting.

are returned by the 2D modelling up to CASE 4 (inclusive), representing the typical quasar brightness in our sample. In Chapter 2 we also demonstrate that more luminous quasars tend to reside in more luminous host galaxies. These results therefore suggest that the 2D modelling is capable of constraining at least the g-band magnitudes of the host galaxies for the majority of reddened quasars in our sample. We note however, that several additional factors may improve our ability to recover these magnitudes. If the galaxy appears extended for example, its emission will likely be easier to disentangle from that of the quasar, provided the effects of surface brightness dimming are insufficient in driving the galaxy emission

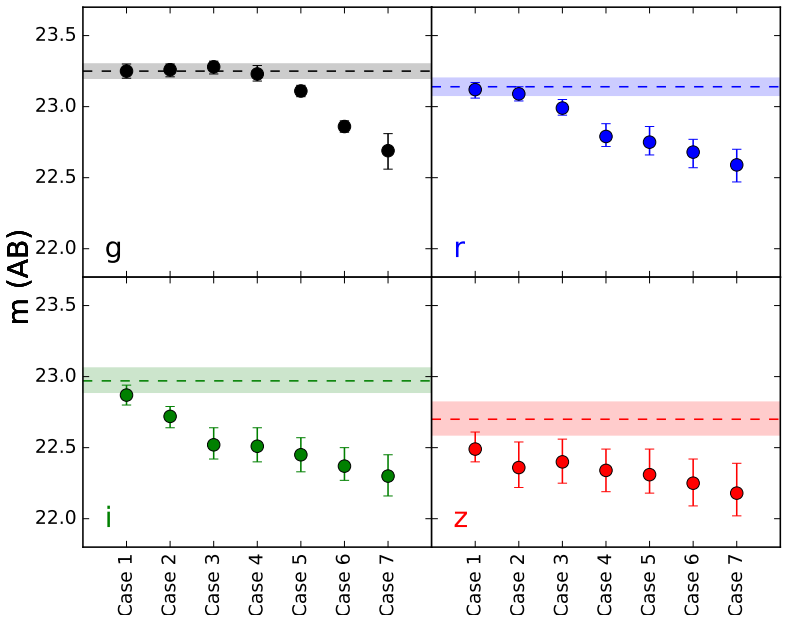

Fig. 3.11 Returned galaxy magnitudes in each band for the typical local DES analogue galaxy ($G_{typical}$) compared to the galaxy magnitude returned from the galaxy-only fit (*dotted line*). Shaded regions and error bars denote the statistical 68 per cent confidence bounds on the values returned from the fitting.

below the noise level of the image. Furthermore, Figs. 3.8 and 3.9 show $R_{eff,G1} > R_{eff,G2}$, implying that our ability to recover the galaxy magnitudes is not simply dependant on the galaxy and quasar brightness, but also on the physical extent.

Figs. 3.12 and 3.13 show the recovered quasar magnitudes for G_{bright} and $G_{typical}$ when including a simulated quasar component in the image. The magnitudes of the brightest quasars (CASES 6,7 and 8) are recovered in the three reddest bands (*riz*) for both G_{bright} and $G_{typical}$, with the correct quasar magnitudes returned in the *z*-band in all but CASE 1, where the quasar is faintest. The fewest quasar magnitudes are returned correctly in the *g*-band, with only CASE 6 and CASE 7 recovering the predicted quasar magnitudes for G_{bright}, with no correctly returned *g*-band magnitudes in the fitting of $G_{typical}$. We note however that this effect may be largely driven by the flux limit of the survey, illustrated by the shaded regions in Figs. 3.12 and 3.13. In the majority of instances for which we return quasar magnitudes inconsistent with the expected value, we find the expected magnitude to lie below the flux limit of the survey, meaning we expect magnitudes to be poorly constrained in these cases.

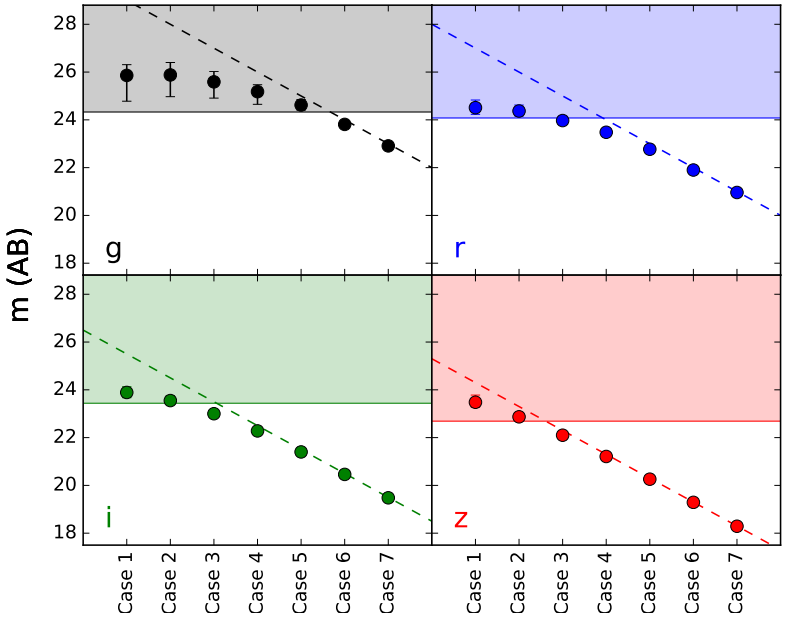

Fig. 3.12 Returned quasar magnitudes in each band for G_{bright} compared to the magnitude of the quasar component added to the original galaxy image (*dotted line*). Error bars denote the 68 percent confidence bounds on the returned magnitudes. Shaded regions in each panel denote the area for which magnitudes lie below the flux limit of DES.

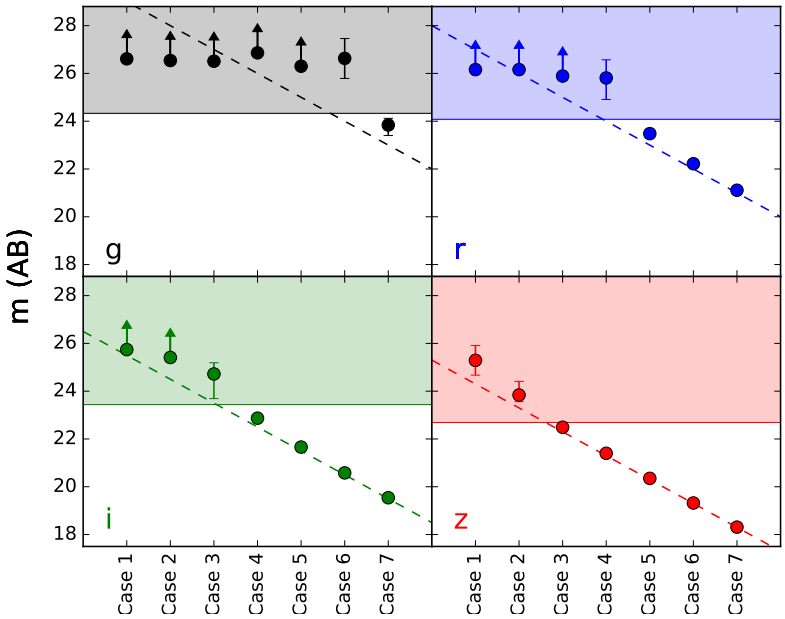

Fig. 3.13 Returned quasar magnitudes in each band for $G_{typical}$ compared to the magnitude of the quasar component added to the original galaxy image (*dotted line*). Error bars denote the 68 percent confidence bounds on the returned magnitudes. Shaded regions in each panel denote the area for which magnitudes lie below the flux limit of DES.

For our DES Y3A1 sample, we therefore expect to return robust quasar magnitudes in all bands across our sample, providing the quasars are brighter than the survey flux limit.

3.5.3 RECOVERING PROPERTIES OF THE GALAXY

Having concluded the 2D modelling to be a valid method of measuring the galaxy and quasar magnitudes, we now investigate to what extent the inferred properties of the host galaxy are reliable. Fig. 3.14 shows the recovered galaxy parameters for the the range of 'bright' composite (galaxy + quasar) images (G_{bright}), alongside the inferred properties when fitting the galaxy image alone (Section 3.5.1). Fig. 3.15 illustrates the same properties returned from the fitting of the 'typical' brightness galaxy ($G_{typical}$).

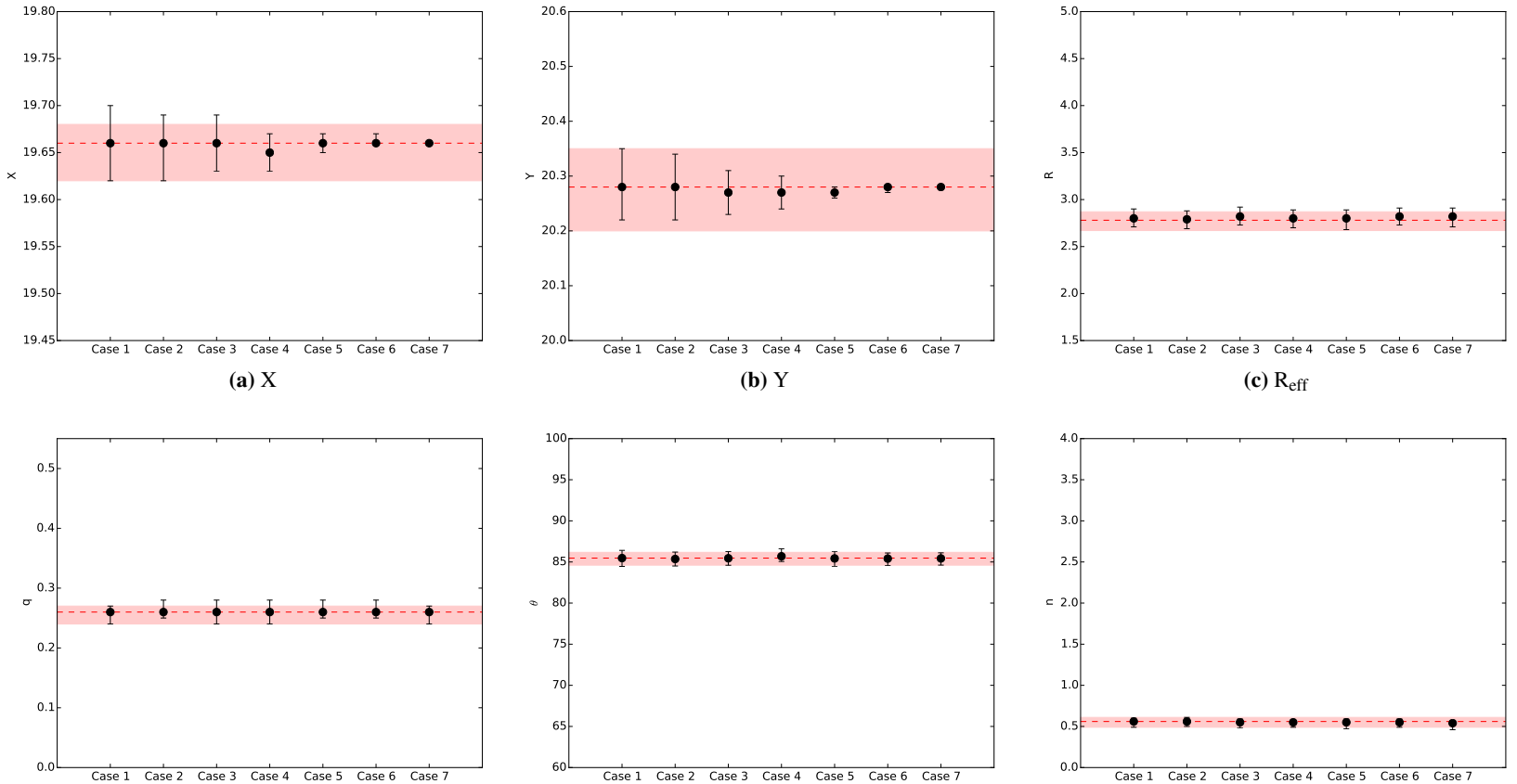

(a) X **(b)** Y **(c)** R_{eff}

(d) q **(e)** θ **(f)** n

Fig. 3.14 Returned galaxy parameters - (X,Y) position of the galaxy and quasar (a) and (b), effective radius (c), axis ratio (d), angle of orientation (e) and Sérsic index (f) - for each bright image with simulated quasars included. Shaded regions and error bars denote the statistical 68 per cent confidence bounds on the values returned from the fitting.

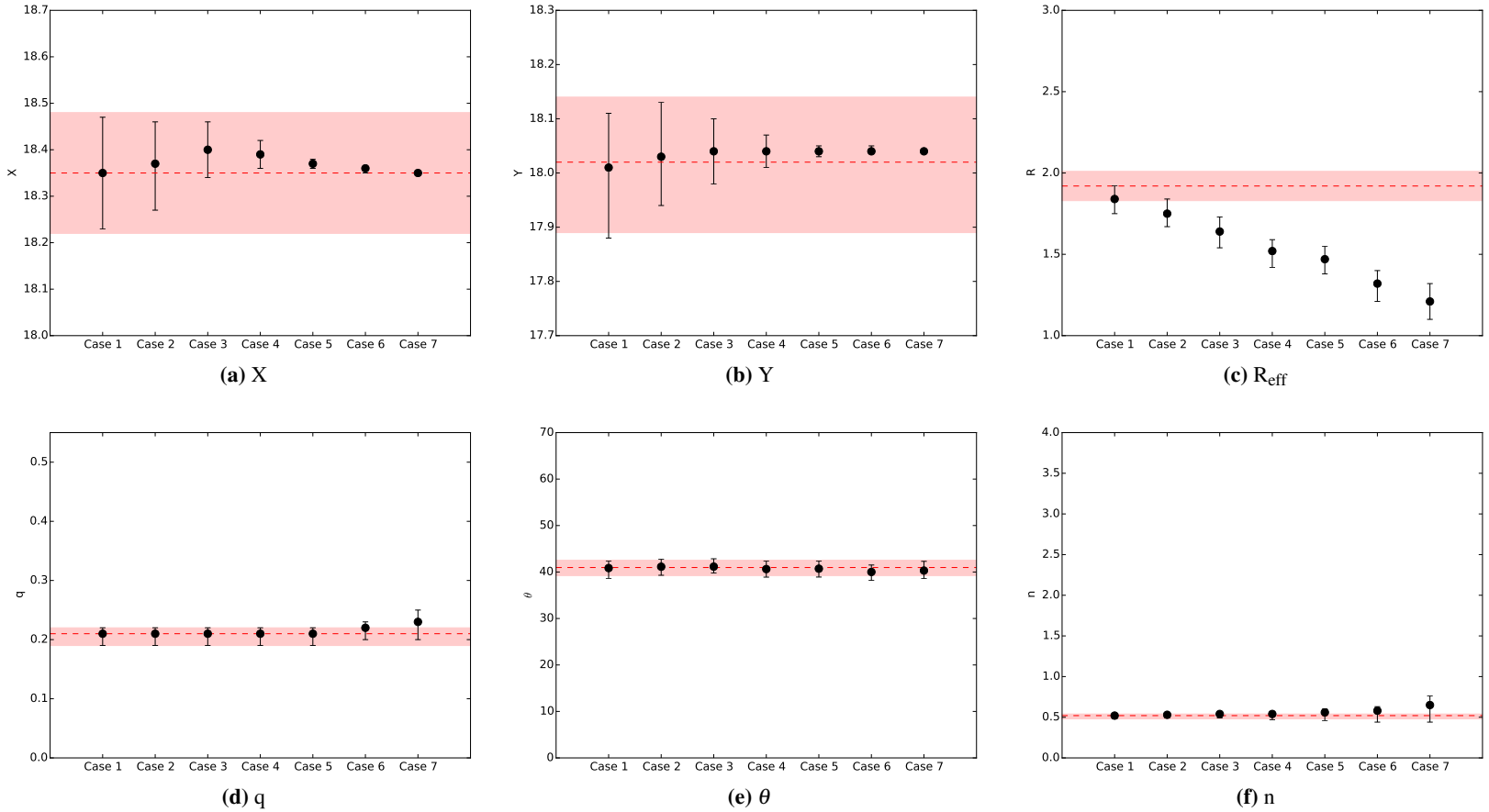

(a) X **(b)** Y **(c)** R_{eff}

(d) q **(e)** θ **(f)** n

Fig. 3.15 Returned galaxy parameters - (X,Y) position of the galaxy and quasar (a) and (b), effective radius (c), axis ratio (d), angle of orientation (e) and Sérsic index (f) - for each average image with simulated quasars included. Shaded regions and error bars denote the statistical 68 per cent confidence bounds on the values returned from the fitting.

From Fig. 3.14, we conclude that all galaxy parameters can be robustly recovered for the brightest host galaxies in our sample. At the average galaxy brightness of our sample, we recover all galaxy parameters with the exception of the effective radius, R_{eff}, which is underestimated in the model when considering quasars brighter than CASE 3 (inclusive). Fig. 3.14 demonstrates that the fitting returns the correct galaxy parameters even for quasars that are brighter than those in our sample. Therefore, for our 'typical' quasar (CASE 4), modelling a slightly dimmer galaxy would likely still return the correct galaxy parameters. Furthermore, we have not yet considered the effects of the galaxy shape on our ability to separate the galaxy and quasar emission in the image. As discussed in Section 3.5.2, one might expect that a more extended galaxy would be more easily disentangled from the quasar in the image, providing the effects of surface brightness dimming are not sufficient to dim the galaxy below the noise in the image. This might be a factor in returning the correct galaxy parameters in G_{bright}. Whilst this chapter considers our ability to recover the galaxy properties to be dependent solely on the magnitude of each component in the image, in reality several other factors are likely to play a role, including the radius, axis ratio and Sérsic index of the system. Quantifying the effect of these parameters in detail lies beyond the scope of this chapter, but would be an interesting avenue to explore as we continue to expand upon this work.

3.5.4 CONCLUSIONS

Until now, 2D modelling of quasar hosts has relied heavily on space-based observations providing high spatial resolution (e.g. Bahcall et al., 1997; Boyce et al., 1998; Dunlop et al., 2003; Hooper et al., 1997; McLeod and McLeod, 2001), with the modelling of ground-based imaging limited to low redshifts. The work presented in this chapter seeks to perform 2D surface photometry on ground based images of luminous, reddened quasars at $z\sim2$, with the aim of returning properties of the host galaxy. In particular, this work focusses on testing the extent to which we can trust the parameters inferred from the models of our sample. From this work we conclude the following;

(i) We successfully model 13 of the 14 objects in our DES Y3A1 sample. Each model returns (data - model) residuals consistent with the noise in the images, indicating they are a good fit to the image data. The single object not returning a good fit is that of VHSJ2332-5240, for which we identify there to be two galaxies in the image and therefore decide to exclude this object from the further analysis of the sample. In future however, we plan to use the methods outlined in this chapter to simultaneously fit models to multiple sources in images such as VHSJ2332-5240.

(ii) We compare the *griz* magnitudes of each model component inferred from this method with those inferred from the SED fitting in Chapter 2, finding a broad consistency between the inferred magnitudes across the two methods. In the cases for which the returned magnitudes do not agree, we suggest that the difference is likely due to the underlying method used to fit the data in each case. In the SED fitting for example, the colour of the galaxy is fixed by the slope of the galaxy template, which is not permitted to vary during the fitting. In this way, the magnitudes in each band are constrained only by the normalisation of the galaxy model (or quasar model when inferring quasar magnitudes). In the 2D modelling however, the colours are unconstrained and the magnitudes of each component are solved for individually in each band. Allowing for a quasar component in the fit of each band instead of fixing the colours of the quasar template like in the SED fitting potentially causes the 2D modelling to infer a compact PSF component in the image where there really is none. Indeed, when we fit a local galaxy from DES with colours similar to a 'bright' galaxy in our sample (Section 3.5.1), the model infers a faint quasar component lying below the detection limit of the DES Y3A1 survey, thus a small fraction of the galaxy light is being attributed to the quasar. Alternatively, the extra spatial dimension of the imaging data provides further constraints when separating the galaxy and quasar light, potentially making it easier to separate the two components. Moving forward, we therefore hope to combine the colour constraints of the SED fitting with the flexibility and spatial information of the 2D modelling by incorporating the SED templates into the priors of the 2D modelling. In this way, we seek to return models for these systems with physical colours consistent with those expected from the heavily reddened quasars of our sample.

(iii) For the 13 objects successfully modelled by the fitting code, we derive constraints on several parameters of the host galaxy. With the exception of the effective galaxy radius, R_{eff}, we find it may be possible to infer parameters of the quasar host galaxies across our sample of reddened quasar hosts. Furthermore, it may be possible to also recover R_{eff} for the brightest host galaxies in our sample. The criteria required to return the galaxy parameters in the fitting, may however depend on several other factors, the effects of which we do not model in this chapter. One may expect, for example, that light from a large or highly elliptical galaxy is easier to disentangle from the quasar than a compact, spherically symmetric galaxy. Quantifying the effect of parameters such as R_{eff}, q and n on our ability to model the galaxy forms the basis of future work in this area, for which we intend to create large sets of simulated images with a range of galaxy properties spanning the region of interest. Because the properties of the simulated data are explicitly known, we will be able to directly measure how well the model returns the properties of the galaxy and place better constraints on the fraction of our DES Y3A1 sample for which the inferences are robust.

For the first time, we have demonstrated that 2D surface photometry can be used to potentially model the hosts of luminous z$\sim$2 quasars from ground-based data. By exploiting the dust reddening of our quasar sample and by implementing a multi-band fitting routine, we successfully model all but one object in our sample. By fitting similar low-redshift systems with a simulated quasar component, we test the reliability of the returned parameters in our models, returning robust measures of all galaxy parameters, with the exception of R_{eff}. Moving forward, we seek to further explore the reliability of this modelling method, accounting for the effects of various parameters, such as the size and shape of the galaxy, in the fitting. Introducing multi-object modelling will also allow us to expand our sample to include objects such as VHSJ2332-5240, where several images are oberved in the data, allowing us to expand the sample of reddened quasars modelled.

CHAPTER 4

REDDENED QUASAR HOSTS IN THE SUB-MM

4.1 INTRODUCTION

Understanding the connection between black hole activity, star formation and dust obscuration in quasar hosts is critical in constraining evolutionary models of massive galaxies. Although dust obscuration in low to moderate luminosity quasars and at low redshift has been shown to arise primarily from orientation effects (e.g. Antonucci, 1993), there is evidence to suggest evolution also plays a role among populations of high redshift luminous quasars (e.g. Chen et al., 2013; Rodighiero et al., 2010). Sanders et al. (1988) for example postulate that heavily obscured quasars exist in a short-lived transitional phase between a merger-driven starburst galaxy and a UV-luminous quasar. One way to test such evolutionary models is therefore to look for excess star formation in the hosts of obscured quasars relative to unobscured populations.

Throughout this thesis we have sought to investigate the star forming properties among a population of obscured quasar hosts at z$\sim$2. Until now however, we have considered only the restframe-UV emission, tracing the unobscured star formation in these galaxies and accounting for a small fraction of the total star formation. To measure the star formation obscured by dust, one must instead look to longer wavelengths, where thermal emission

from dust dominates the spectrum. This thermal emission arises from high-energy photons, often produced by young stars, being absorbed by the interstellar dust and thermally re-radiated at longer wavelengths and thus can act as a tracer of star formation. Over the last decade, observations from *Herschel* - a space based telescope operating at FIR to sub-mm wavelengths (194-671μm) - have been used to study the connection between AGN accretion and star formation at a range of redshifts (e.g. Lutz et al., 2008; Mullaney et al., 2012; Page et al., 2012; Stanley et al., 2015). Over this range of wavelengths however, Rosario et al. (2013) demonstrate that emission in the *Herschel*-SPIRE bands (centred at 250μm, 350μm and 500μm) suffers significant contamination from AGN dust heating, particularly among populations of the most luminous quasars.

At longer sub-mm wavelengths ($\sim$850μm) however, the dust being traced is cooler and thus less likely to have been heated by the AGN. Although synchrotron emission can potentially contaminate emission at these wavelengths, this remains negligible for the majority of AGN which are radio quiet. Instead, dust heating in this regime is often attributed to young stars and is therefore a good tracer of star formation. Early sub-mm studies of X-ray luminous AGN using the SCUBA bolometer on the James Clerk Maxwell Telescope (JCMT) find evidence for high SFRs in obscured AGN hosts, consistent with an evolutionary picture of quasars in which these obscured systems have undergone a recent starburst (e.g. Page et al., 2001, 2004; Stevens et al., 2005). Among populations of unobscured ($A_\nu \sim$ 0 mags), UV-bright quasars, Priddey et al. (2003) also find evidence for strong sub-mm emission in $\sim$15-20 per cent of their sample, but find little evidence to suggest this emission is directly linked to the UV luminosity of the quasar. More recently, the subsequent SCUBA-2 instrument has been used to study the sub-mm properties of very heavily obscured ($A_\nu > 15$ mags) Hot Dust Obscured Galaxies (HotDOGs) selected from WISE (e.g. Jones et al., 2015, 2014). In the radio quiet HotDOGs, Jones et al. (2015) find evidence for strong sub-mm emission in 16 per cent of their sample, but this increases to 60 per cent in the radio-loud sample (Jones et al., 2014). These studies also conclude that heavily obscured quasars reside in overdense regions of the sky, potentially supporting the idea that obscured quasars are driven by mergers (Jones et al., 2015, 2014).

In this chapter, we make use of new, targeted 850μm SCUBA-2 observations for a sample of 19 moderately-obscured ($A_V \sim$ 2-6 mags) quasars at z$\sim$2 - a peak epoch in both star formation and black hole accretion. In particular, we seek to explore the sub-mm properties of the host galaxies, comparing our sample with populations of both more heavily-obscured ($A_V > 15$ mags) and UV-luminous ($A_V \sim 0$ mags) quasars at a similar epoch. In Section 4.2, we outline the sample of obscured quasars considered in this chapter, detailing the reduction pipeline and the resulting SCUBA-2 photometry in Section 4.3. Here, we also explore the star forming and environmental properties of our sample, with comparisons to both heavily obscured and unobscured quasar populations in Section 4.4. Key results are summarised in Section 4.5.

4.2 DATA

This work concerns a sample of 19 reddened quasars ($A_V \sim$ 2 - 6 mags) at redshifts $1.4 <$ z < 2.7, outlined in Banerji et al. (2015a, 2012, 2013), Temple et al. (2018 *in prep.*). The initial selection criteria for these quasars and details of the new sub-mm observations are described below.

4.2.1 NIR SELECTION

Red quasar candidates were identified in the near infra-red (NIR) imaging of the wide-field UKIDSS Large Area Survey (ULAS) and VISTA Hemisphere Survey (VHS), as detailed in Banerji et al. (2015a, 2012). Targets were required to appear as point-sources in the *K*-band, with $K_{AB} < 18.4$[1] to exclude galaxies and isolate the sample of high redshift, NIR-luminous quasars. A $(J\text{-}K)_{AB}$ colour cut ($>$1.5) was applied to select targets with extremely red NIR colours, indicating significant dust reddening ($A_V \sim$ 2 - 6 mags). Of the 66 targets selected in this manner, 61 were successfully followed up with either SINFONI VLT or Gemini-GNIRS observations (Banerji et al., 2015a, 2012, 2013), from which 38 were spectroscopically-confirmed to be Type-1 broad-line (BL) quasars at $1.4 < z < 2.7$. An additional 26 red quasar

[1]Magnitudes were calculated within a 1 arcsecond radius aperture (*apermag3*) and include an aperture correction appropriate for point sources.

candidates were identified from ULAS, VHS and the VISTA Kilo-Degree Infra-red Galaxy Survey (VIKING) and were designed to supplement the Banerji et al. (2015a, 2012, 2013) samples by targeting both the most luminous and reddest quasars with $(H\text{-}K)_{AB}$ >1.5 as well as extending the sample to fainter magnitudes by making use of the VIKING photometry, which probes 1.4 mags deeper than ULAS and VHS in the *K*-band. Twenty-five of these 26 quasar targets were spectroscopically-confirmed to be Type-1 broad-line (BL) quasars with redshifts $0.7 < z < 2.6$. The parent sample for this chapter therefore consists of 63 spectroscopically-confirmed quasars, from which we select 19 quasars observable from the northern hemisphere (Dec >-17deg) for sub-mm follow-up with SCUBA-2. With extinction-corrected bolometric luminosities of $L_{bol,QSO} \sim 10^{47} ergs^{-1}$ and $M_{BH} \sim 10^{9-10}$ $M_{\odot}$ (Banerji et al., 2015a), these quasars are among the most luminous and massive accreting SMBHs known at z$\sim$2.

4.2.2 SCUBA-2 OBSERVATIONS

SCUBA-2 is a dual wavelength camera, operating at 450μm for the short waveband and 850μm for the long waveband, with diffraction-limited beam full-width half maxima (FWHM) of approximately 7.5- and 14.5-arcsec respectively. Each of the two focal planes comprise four sub arrays of 1280 bolometers, totalling 5120 pixels in each plane (Holland et al., 2013).

The 19 quasar targets were observed with SCUBA-2 on the 15m *James Clerk Maxwell Telescope* (JCMT) on Mauna Kea, Hawaii, between 2017 March and May. Each target was observed in the ‘"CV Daisy" observing mode, which is suitable for point-like sources or sources with structure on scales < 3-arcmin. This observing mode produces a 12-arcmin diameter map, with the deepest coverage in the central 3-arcmin diameter region, where all four sub-arrays overlap (Holland et al., 2013). Details of the 19 reddened quasars observed with SCUBA-2 are given in Table 4.1. The exposure time for each observation ranges between 25 and 37 minutes, reaching a 1σ target depth of 1.6 mJy.

Table 4.1 Details of the SCUBA-2 observations for the 19 heavily-obscured quasars in our sample.

Name	RA	DEC	Observation Date	Exposure Time (HH:MM:SS)	z
ULASJ0041-0021	10.3041	-0.3520	2017.05.06	00:32:32	2.517
ULASJ0016-0038	4.0025	-0.6498	2017.05.06	00:32:28	2.194
ULASJ1234+0907	188.6147	9.1317	2017.04.16	00:30:40	2.503
VHSJ1117-1528	169.2656	-15.4749	2017.04.17	00:36:47	2.427
VHSJ1122-1919	170.6018	-19.3215	2017.04.17	00:36:47	2.465
ULASJ1216-0313	184.1324	-3.2264	2017.04.16	00:32:14	2.576
VHSJ1301-1624	195.3805	-16.4150	2017.04.17	00:36:53	2.140
VHSJ1350-0503	207.6552	-5.0665	2017.04.18	00:33:45	2.176
VHSJ1409-0830	212.3721	-8.5163	2017.04.18	00:34:49	2.300
ULASJ1455+1230	223.8375	12.5024	2017.05.04	00:31:10	1.460
ULASJ1539+0057	234.7923	5.9638	2017.04.04	00:30:57	2.658
VHSJ1556-0835	239.1571	-8.5952	2017.04.17	00:33:55	2.188
VHSJ2109-0026	317.3630	-0.4497	2017.04.03	00:32:02	2.344
VHSJ2143-0643	325.8926	-6.7206	2017.03.30	00:33:57	2.383
VHSJ2144-0523	326.2394	-5.3881	2017.04.04	00:25:09	2.152
ULASJ2200+0056	330.1036	0.9346	2017.04.17	00:32:27	2.541
ULASJ2224-0015	336.0392	-0.2566	2017.04.18	00:32:04	2.223
ULASJ2315+0143	348.9843	1.7307	2017.05.05	00:32:32	2.560
VHSJ2355-0011	358.9394	-0.1893	2017.05.06	00:32:25	2.531

4.3 RESULTS

4.3.1 PHOTOMETRY

The 850μm SCUBA-2 observations are reduced with the STARLINK SubMillimetre User Reduction Facility (SMURF) data reduction package. We select the 'REDUCE_SCAN_FAINT _POINT_SOURCES' recipe, which uses a 'Blank Field' configuration suitable for point sources with low signal-to-noise ratio (Chapin et al., 2013). Initial pre-processing is carried out by the SMURF software, which cleans the data by modelling the signal contributions from each bolometer, removing unwanted atmospheric emission and re-gridding the data to produce a science-quality image. Each of these science-quality images are then combined as a mosaic, centred on the sky position of the source, by the PIpeline for Combining and Analysing Reduced Data (PICARD). Finally, a beam-matched filter is applied to the resulting mosaicked image, smoothing the image with a 15 arcsec FWHM Gaussian and calibrating the resulting map with a flux conversion factor of 2.34 Jy pW^{-1}arcsec^{-2} (appropriate for

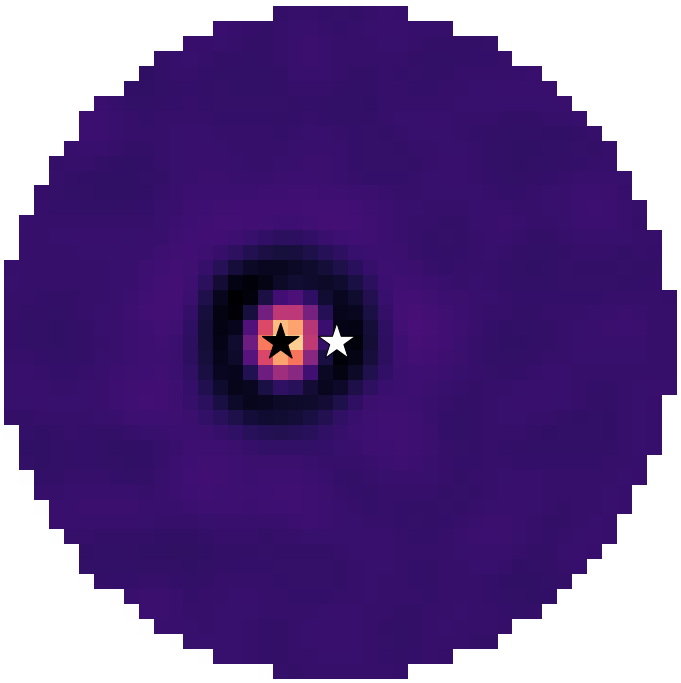

Fig. 4.1 1.5 arcmin radius 850μm map of the pointing calibrator 3C273 showing astrometry offset between the catalogued position (*white star*) and the position of the source in the image (*black star*). North is up, East is to the left.

point sources). In this way, 850μm maps are created for each of the 19 reddened quasars in our sample.

To check the final astrometry and photometry of the SCUBA-2 maps, we also reduce the pointing (3C273) and flux (CRL 2688) calibrators observed on 2017.03.30 through an identical pipeline. The catalogued positions of 3C273 and the SCUBA-2 beam are overlaid on the resulting map (Fig. 4.1), where we derive an offset of |ΔRA| = 15 arcsec and |ΔDec| = 0 arcsec, arising from the mosaicking step in the reduction. These offsets are quoted to the nearest arcsec as they have been calculated from the pixel differences between the catalogued position of the source and the peak flux in the image (Δx, Δy) and thus are accurate to the nearest pixel, corresponding to 4.0 arcsec in the map. This offset is found to result from the mosaicking step in the data reduction and is not due to the pointing of the telescope itself. After accounting for the measured offset in the flux calibrator image, CRL 2688, the peak flux is calculated to be 5.85 Jy/beam, consistent with the 5.64 $\pm$ 0.27 Jy/beam expected at

Table 4.2 Selected calibrators for each night of SCUBA-2 observations, along with the corresponding astrometry offsets in RA and Dec.

Observation Date	Calibrator	ΔRA (arcsec)	ΔDec (arcsec)
2017.03.30	3C273	-15	0
2017.04.03	3C273	-15	0
2017.04.04	3C273	-15	0
2017.04.16	3C273	-15	0
2017.04.17	3C273	-15	0
2017.04.18	3C279	-12	4
2017.05.04	Arp220	-13	1
2017.05.05	IRC+10216	-15	0
2017.05.06	IRC+10216	-15	0

850μm in CRL 2628. In light of the astrometric offset in our reduced images, we reduce a pointing calibrator for each night over which SCUBA-2 data was collected and calculate the RA and Dec offset as above, shifting the SCUBA-2 beam to align with the position of the source. Table 4.2 details the calibrator used for each night and the corresponding offset in the reduced images.

Having corrected for the offsets in the astrometry (Table 4.2), fluxes for the 19 quasar targets are calculated as the peak flux density within a 14.5 arcsec diameter aperture centred on the quasar, matching the beam size of SCUBA-2. These values are given for our full sample in Table 4.3 along with the corresponding noise level (σ_{850}), typically $\sim$1.6 mJy beam^{-1}. The noise level for each map has been directly derived from the sky background using the Kernel APplication PAckage (KAPPA) within the STARLINK software. Of the 19 quasars in our sample, three sources are detected with a confidence $>3\sigma$ - ULASJ1216-0313, ULASJ2200+0056 and ULASJ2315+0143 (Fig. 4.2). Of these, two (ULASJ1216-0313 and ULASJ2315+0143) are detected with a $>4\sigma$ confidence. Here, and throughout this chapter, we classify a detection as an object with a given confidence level overlapping the position of the SCUBA-2 beam, which has been centred on the NIR quasar position. For this reason, we classify ULASJ2200+0056 as a detection despite the apparent offset between the sub-mm source and the centre pointing of the SCUBA-2 beam.

All of the remaining 16 quasar targets in our sample lying below the 3σ detection limit have a positive peak flux within a beam-sized aperture centred on the NIR position of the

Table 4.3 850μm flux densities and associated uncertainties for the 19 quasars in our sample. '*' denotes sources detected at $>3\sigma$ significance.

Name	$S_{850,peak} \pm \sigma_{850}$ (mJy)
ULASJ0041-0021	0.500 ± 1.702
ULASJ0016-0038	0.179 ± 1.735
ULASJ1234+0907	2.473 ± 2.080
VHSJ1117-1528	0.650 ± 1.999
VHSJ1122-1919	0.114 ± 1.626
ULASJ1216-0313*	10.201 ± 1.860
VHSJ1301-1624	2.663 ± 1.623
VHSJ1350-0503	0.702 ± 1.871
VHSJ1409-0830	3.264 ± 1.711
ULASJ1455+1230	3.545 ± 1.874
ULASJ1539+0057	3.176 ± 1.568
VHSJ1556-0835	2.568 ± 1.589
VHSJ2109-0026	1.598 ± 1.620
VHSJ2143-0643	0.743 ± 1.540
VHSJ2144-0523	0.871 ± 1.099
ULASJ2200+0056*	6.017 ± 1.649
ULASJ2224-0015	1.032 ± 2.046
ULASJ2315+0143*	6.324 ± 1.595
VHSJ2355-0011	3.436 ± 1.730

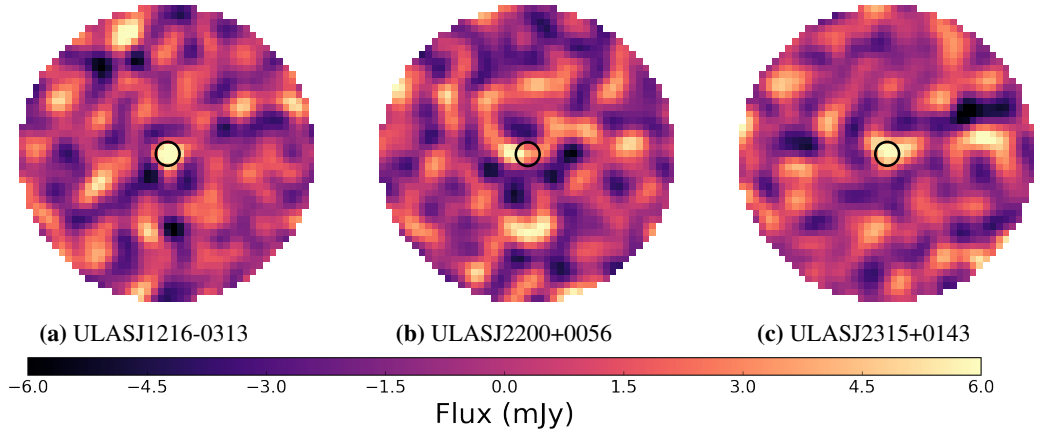

(a) ULASJ1216-0313 **(b)** ULASJ2200+0056 **(c)** ULASJ2315+0143

Fig. 4.2 850μm SCUBA-2 maps for the three sources detected at a significance $>3\sigma$ - ULASJ1216-0313, ULASJ2200+0056 and ULASJ2315+0143. Black circle denotes a 14.5-arcsec diameter aperture centred on the SCUBA-2 position of the target source. North is up, East is to the left.

quasar, with a typical significance of $\sim 1\sigma$. To explore the average sub-mm properties of our sample we stack these 16 undetected sources, which all lie at z$\sim$2, to create a single image centred on the NIR position of each target. An inverse variance weighting is applied to the stack to account for any noise variation across our sample i.e.

$$S_{\rm ij} = \frac{\sum_{\rm k=1}^{\rm N} P_{\rm ij} \times f_{\rm ij}^{\rm k} / (\sigma_{\rm ij}^{\rm k} \times \sigma_{\rm ij}^{\rm k})}{\sum_{\rm k=1}^{\rm N} P_{\rm i,j} / (\sigma_{\rm ij}^{\rm k} \times \sigma_{\rm ij}^{\rm k})}, \tag{4.1}$$

where $S_{\rm ij}$ denotes the stacked flux at the centre of the image. P_{ij} denotes the response function of SCUBA-2 at 850μm, taken to be the PSF for each observation, f_{ij} are the flux densities for each of the N sources in our sample and σ_{ij} are the corresponding RMS noise maps. The resulting stacked image is shown in Fig. 4.3, where we derive a peak flux of 0.776 $\pm$ 0.555 mJy within the SCUBA-2 beam size - a detection of $\sim 1.4\sigma$. Due to the relatively small sample size, a typical jackknife re-sampling technique cannot be used to get an accurate representation of the noise in the stacked image. Instead, the quoted noise level is derived directly from the standard deviation of the pixels over a blank portion of the stacked image itself. Although the returned flux of the stacked image lies below the detection threshold for our sample ($>3.5\sigma$; $\sim$1.9mJy), we note that this value is consistent with that found in the work of Banerji et al. (2015b), who stack the SCUBA-2 non-detections of a much larger sample of 697 X-ray luminous quasars to return a stacked flux of 0.60$\pm$0.07mJy.

4.3.2 DUST-OBSCURED STAR FORMATION

The substantial dust reddening of our sample ($A_\nu \sim$ 2-6 mags) could be associated with significant amounts of obscured star formation. Indeed, the detection of broad emission lines in the spectra of our quasar sample indicate that the dust responsible for the reddening is not nuclear, as would be expected from an AGN torus. Furthermore, several of the quasar targets show evidence for narrow Hα emission, typically associated with star formation (Alaghband-Zadeh et al., 2016b), with *Herschel* observations showing the reddest quasar in our sample - ULASJ1234+0907 - to have significant levels of obscured star formation. Recent ALMA observations of four luminous, obscured quasars from Banerji et al. (2017)

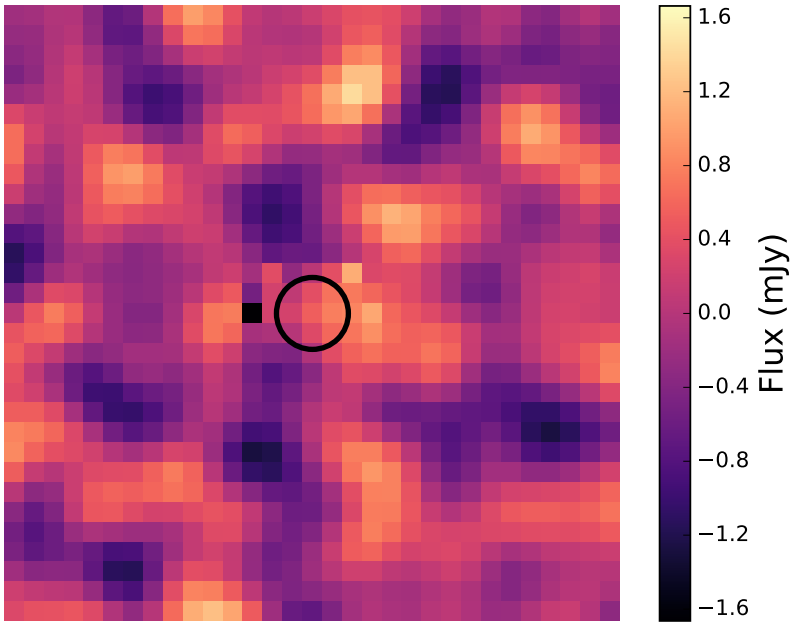

Fig. 4.3 Inverse variance weighted stack for the 16 undetected targets in our sample. Peak flux of 0.776 ± 0.555 mJy ($\sim 1.4\sigma$) within a 14.5 arcsec SCUBA-2 beamsize.

have also demonstrated the host galaxies of these quasars to be in a starburst phase, with two of the four quasars observed - ULASJ1234+0907 and ULSJ2315+0143 - overlapping with our sample.

Based on the photometry in Table 4.3, we now derive SFRs for the three sources in our sample detected at 850μm - ULASJ1216-0313, ULASJ2200+0056 and ULASJ2315+0143 - and for the stacked non-detections (Fig. 4.3). We begin by modelling the sub-mm emission from our reddened quasar sample with a grey-body template, characterised by three parameters; the dust temperature, T, the emissivity index, β and the overall normalisation, $f_{\rm GB}$. The template is characterised as follows;

$$S(\nu) = 10^{-20} \times (1 - e^{\left[\frac{-\nu}{\nu_0}\right]^{\beta}}) \times \frac{\nu^3}{e^{\frac{h\nu}{kT}} - 1}, \tag{4.2}$$

where the grey-body emission, $S(\nu)$, is given in units of mJy (Casey, 2012). If a galaxy's inter-stellar medium (ISM) has been partially heated by star formation, the dust temperature is expected to lie in the range $20 \lesssim T \lesssim 60$ K. In line with this, we select two distinct

grey-body models widely used for quasars in the literature: (i) T=47K, β=1.6 (Priddey and McMahon, 2001) and (ii) T=41K, β=1.95 (Beelen et al., 2006). Each model is fit in turn to the photometry of ULASJ1216-0313, ULASJ2200+0056 and ULASJ2315+0143, with the overall normalisation left as a free parameter in the fitting. The resulting grey-body models for each of the three quasars detected at $>3\sigma$ are shown in Fig. 4.4. Similarly, the grey-body template modelling the stacked non-detections is given in Fig. 4.5. The shaded regions in each of the greybody templates denote the 1σ uncertainty in each fit, derived from fitting the upper and lower 1σ bounds of the photometry.

From the resulting grey-body templates, we derive estimates for the obscured star formation in ULASJ1216-0313, ULASJ2200+0056, ULASJ2315+0143 (Fig. 4.4) and the stacked non-detections (Fig. 4.5). To this end, we integrate over the best-fit grey-body curve for each scenario to get the far infra-red (FIR) luminosity i.e.

$$L_{\rm FIR} = 4\pi D_{\rm L}^2 \int_{\nu_{\rm min}}^{\nu_{\rm max}} S(\nu) d\nu, \tag{4.3}$$

where D_L is the luminosity distance, ν_{min} and ν_{max} denote integral limits in terms of frequency (ν_{min} = 1.0 THz; ν_{max} = 7.5 THz, corresponding to wavelengths $40\mu{\rm m} < \lambda < 300\mu{\rm m}$) and $S(\nu)$ is the best-fit grey-body curve for each of the detected quasars and the stacked image. We opt to use $L_{\rm FIR}$ - tracing the emission at $40\mu{\rm m} < \lambda < 300\mu{\rm m}$ - rather than the total IR luminosity in order to minimise contamination from dust heating caused by the quasar, which can significantly contribute to the flux at $\lambda < 40\mu$m. In this manner, we therefore isolate cold dust emission in the host galaxy caused by star formation. The SFR for each system is then derived from the relation outlined in Kennicutt Jr and Evans (2012) i.e.

$$SFR = 3.89 \times 10^{-44} \times L_{\rm FIR}, \tag{4.4}$$

where the SFR is given in units of $M_\odot yr^{-1}$. Based on the model assumptions of Priddey and McMahon (2001) and the conversion in Eqn. 4.3, we derive SFRs of $\sim$4570 $\pm$ 830 $M_\odot yr^{-1}$, $\sim$2700 $\pm$ 740 $M_\odot yr^{-1}$ and $\sim$2840 $\pm$ 720 $M_\odot yr^{-1}$ for ULASJ1216-0313, ULASJ2200+0056 and ULASJ2315+0143 respectively. Using the grey-body parameters

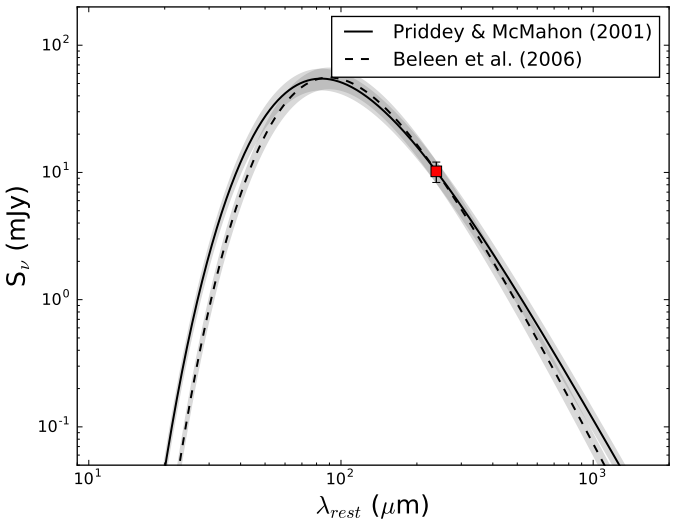

(a) ULASJ1216-0313

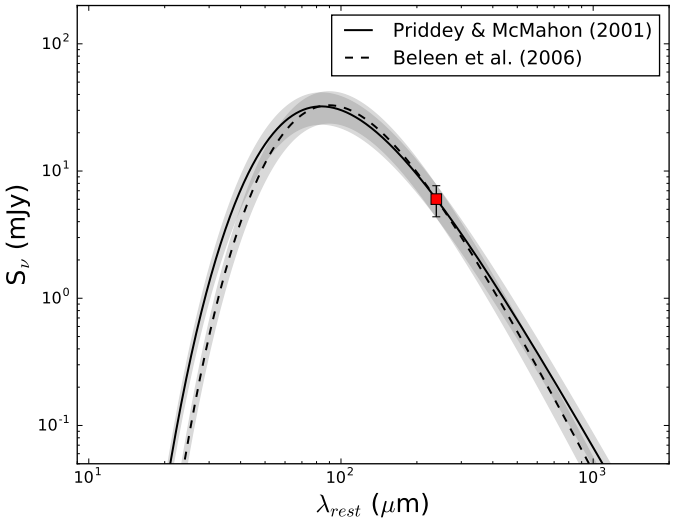

(b) ULASJ2200+0056

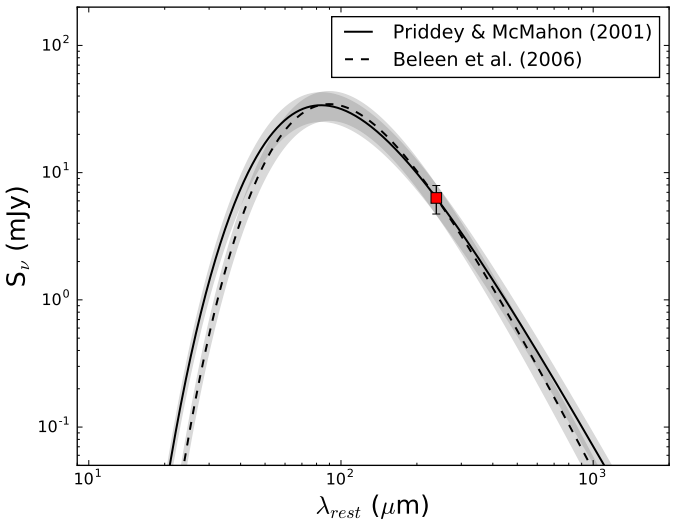

(c) ULASJ2315+0143

Fig. 4.4 Grey-body fit to the 850μm photometry of ULASJ1216-0313 (a), ULASJ2200+0056 (b) and ULASJ2315+0143 (c) assuming (i) T=47K, β=1.6 (Priddey and McMahon, 2001) *(solid)* and (ii) T=41K, β=1.95 (Beelen et al., 2006) *(dashed)*. Shaded regions represent the 1σ uncertainty on each fit.

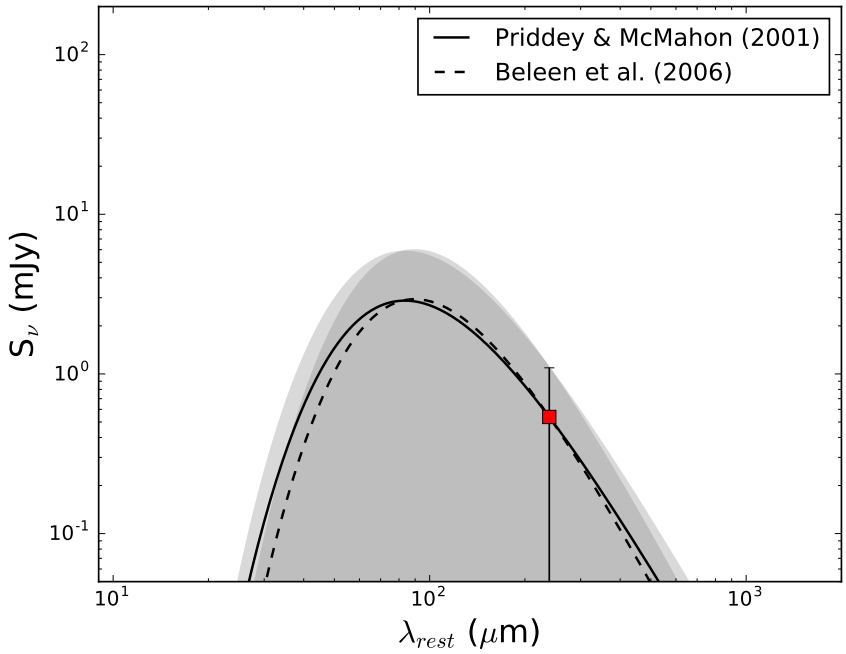

Fig. 4.5 Grey-body fit to the 850μm photometry of the stacked non-detections assuming (i) T=47K, β=1.6 (Priddey and McMahon, 2001) *(solid)* and (ii) T=41K, β=1.95 (Beelen et al., 2006) *(dashed)*. Shaded regions represent the 1σ uncertainty on each fit.

outlined in Beelen et al. (2006), results in slightly lower SFRs of $\sim$4200 $\pm$ 770 $M_\odot yr^{-1}$, $\sim$2480 $\pm$ 680 $M_\odot yr^{-1}$ and $\sim$2600 $\pm$ 660 $M_\odot yr^{-1}$. In the case of the stacked non-detections, we derive 3σ upper limits on the SFRs of $\sim$990 $M_\odot yr^{-1}$ and $\sim$910 $M_\odot yr^{-1}$ assuming the grey-body templates outlined by Priddey and McMahon (2001) and Beelen et al. (2006) respectively. We therefore note that whilst 16 of the 19 quasars in our sample are undetected in SCUBA-2, this does not preclude high SFRs in these systems given the typical flux limit of these observations.

4.3.3 REDDENED QUASAR ENVIRONMENTS

Whilst the majority of our reddened quasar sample are undetected at 850μm, inspection of the maps reveal a number of serendipitous sub-mm detections within a 1.5 arcmin radius of the quasar targets, potentially indicating an environmental overdensity on scales $<$ 1Mpc. To investigate this and to identify any serendipitous detections, we plot contours onto the signal-to-noise ratio maps for each quasar target, denoting regions brighter than the 3, 3.5

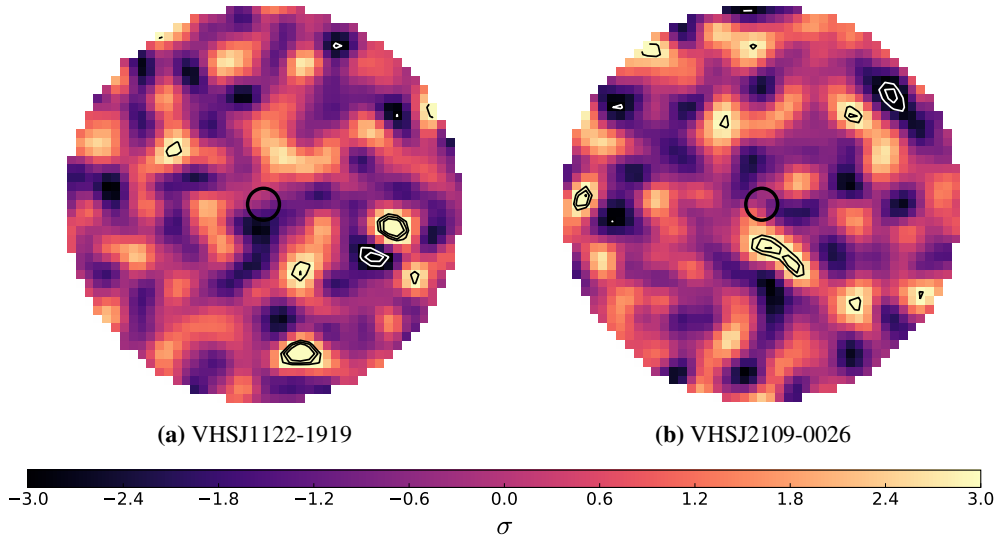

(a) VHSJ1122-1919 **(b)** VHSJ2109-0026

Fig. 4.6 1.5-arcmin radius signal-to-noise ratio maps for two of the quasars in our sample - VHSJ1122-1919 (a) and VHSJ2109-0026 (b) - with $\pm$ 3, 3.5 and 4σ contours overlaid. The SCUBA-2 position of each source is located at the centre of each map, surrounded by a black ring denoting the beamsize of SCUBA-2.

and 4σ noise level of the observation. The signal-to-noise ratio maps were selected in favour of the 850μm maps in order to account for the minor variation in the noise across each image. Objects in the image appearing as two separate sources at either 3.5 or 4σ but as a single, extended object at 3σ were counted as a single object at all thresholds. Furthermore, objects whose contour regions were not fully enclosed within the image (i.e. those lying close to the edge of the map) were omitted from the source count. Similarly, in ULASJ1216-0313, ULASJ2200+0056 and ULASJ2315+0143 - the detected quasar targets, the detections were not counted as additional sources in the image. Fig. 4.6 illustrates the contour plots used to count the sources within 1.5 acrmin of two quasar targets - VHSJ1122-1919 and VHSJ2109-0026.

Table 4.4 shows the number of serendipitous detections found at each significance across our full sample, along with the corresponding number of negative detections for the same threshold. Although a number of negative sources are expected due to 'bowling' around real positive sources in the SCUBA-2 images, we find the number of these negative sources to make up more than half (65 per cent) of the positive sources detected at $>3\sigma$, meaning that only 35 per cent of these positive sources are likely to be real. At 3.5σ, the number of negative sources drops to 52 per cent of the positive detections, with no maps containing

Table 4.4 Number counts for positive and negative sources lying within a 1.5 arcmin radius of each quasar target, detected with a significance above 3, 3.5 and 4σ.

Name	$> 3\sigma$	$< -3\sigma$	$> 3.5\sigma$	$< -3.5\sigma$	$> 4\sigma$	$< -4\sigma$
ULASJ0041-0021	2	3	0	1	0	1
ULASJ0016-0038	3	2	2	1	0	0
ULASJ1234+0907	2	1	1	0	0	0
VHSJ1117-1528	1	1	0	0	0	0
VHSJ1122-1919	5	2	3	1	2	0
ULASJ1216-0313	2	2	1	1	0	0
VHSJ1301-1624	3	1	2	0	0	0
VHSJ1350-0503	1	2	1	0	1	0
VHSJ1409-0830	2	1	0	0	0	0
ULASJ1455+1230	1	1	1	1	1	0
ULASJ1539+0057	1	1	1	0	0	0
VHSJ1556-0835	2	0	1	0	0	0
VHSJ2109-0026	7	2	3	1	2	0
VHSJ2143-0643	1	2	1	1	1	0
VHSJ2144-0523	2	1	2	0	1	0
ULASJ2200+0056	3	3	1	1	0	0
ULASJ2224-0015	0	3	0	1	0	0
ULASJ2315+0143	2	2	1	1	1	1
VHSJ2355-0011	2	1	0	1	0	1
TOTAL	42	31	21	11	9	3

multiple negative detections. When the detection threshold is further increased to 4σ, the negative sources account for just 33 per cent of the positive detections, meaning the majority of sources detected above this threshold are unlikely to be artefacts of the noise in the image. Fig 4.7 shows the location of all 3.5 and 4σ detections across our sample.

In total, we find 21 (10) sub-mm sources at $>3.5\sigma$ ($>4\sigma$) across our reddened quasar sample, corresponding to a survey area of 134.3 arcmin^2. To test whether this is indicative of an environmental overdensity, the number counts for the $>3.5\sigma$ ($\gtrsim$5.6 mJy) and $>4\sigma$ ($\gtrsim$6.4 mJy) detections are directly compared to sub-mm blank field samples (Geach et al., 2017) by plotting the cumulative frequency of the source counts as a function of their 850μm flux (Fig. 4.8). Using the number counts of the positive and negative sources in Table 4.4, we expect 48 per cent of the 3.5σ and 67 per cent of the 4σ detections to be real. We account for this when comparing to the sub-mm blank fields in Fig. 4.8 by scaling the number of sources by the fraction we predict to be real, based on these number counts as follows;

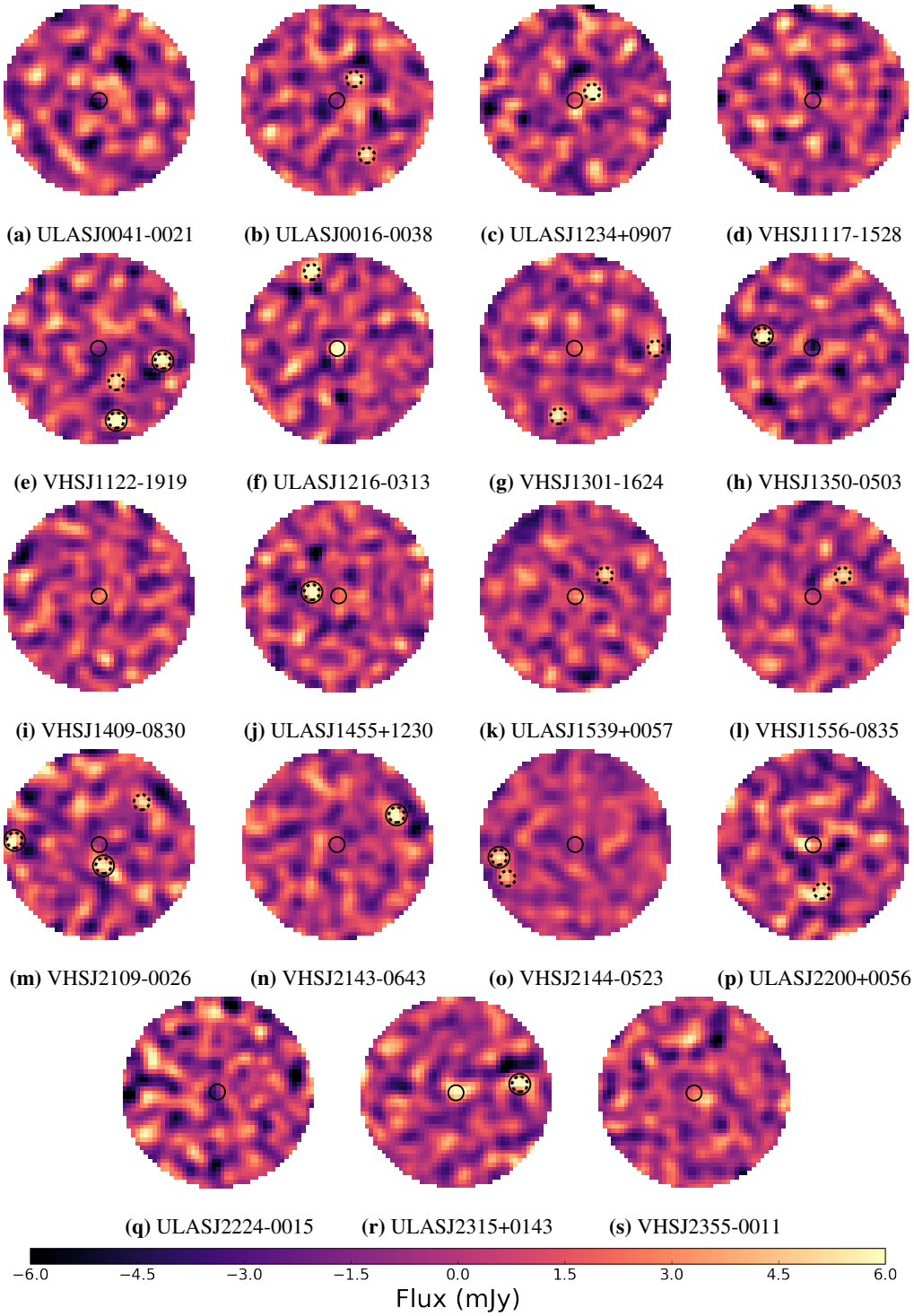

Fig. 4.7 1.5 arcmin radius maps for all quasar targets for which serendipitous sources were detected at $>3.5\sigma$ (*dotted*) and $>4\sigma$ (*solid*). Central aperture denotes the 14.5 arcsec diameter SCUBA-2 beam at the position of each quasar in our sample.

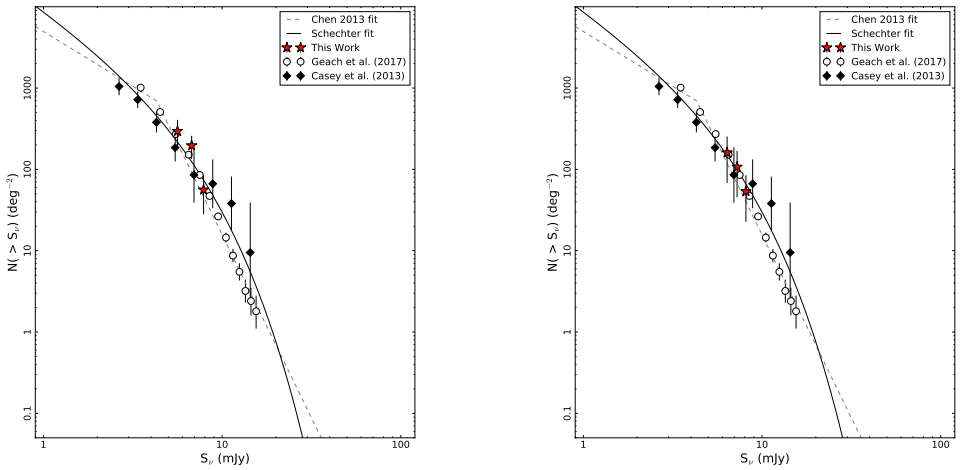

(a) Serendipitous detections $>3.5\sigma$ **(b)** Serendipitous detections $>4\sigma$

Fig. 4.8 Cumulative number of serendipitous 850μm sources above a certain flux density threshold. $>3.5\sigma$ (a) and $>4\sigma$ (b) detections within 1.5 arcmin radius of the reddened quasar targets (red stars) are compared to blank field counts from Geach et al. (2017) (open circles) and Casey et al. (2013) (solid diamonds). All number counts from our sample have been corrected to represent only the fraction of 'real' sources we would expect based on Table 4.4.

$$N_{\rm sources} = N_{+} \times \left(1 - \frac{N_{-}}{N_{+}}\right), \tag{4.5}$$

where N_{+} and N_{-} are the number of positive and negative sources detected respectively across the full survey area.

From Fig. 4.8, we find no evidence for an overdensity in the environments of our dusty quasar sample when compared to the sub-mm blank field. At both >3.5 and $>4\sigma$ we find the source counts within 1.5 arcmins of our quasar sample to be entirely consistent with those in the blank fields when averaging over the full survey area of our sample. We note however, that in seven fields we detect at least one source with a 4σ confidence. Based on the blank field number counts in Geach et al. (2017) and the flux limit of our sample, we would expect just 0.24 sources per map to lie above this threshold, so the fact we see multiple sources surrounding several of the quasars in our sample may indicate that a portion of our sample lies in a significant overdensity compared to the sub-mm blank field. To quantify this, we re-plot Fig 4.8, averaging only over the 56.5 arcmin^2 survey area of the seven targets for which 4σ sources are detected within 1.5 arcmin of the quasar target (Fig. 4.9). Indeed, we now see the number of 4σ detections to lie a factor $\sim$3 above those in the bank fields (Geach

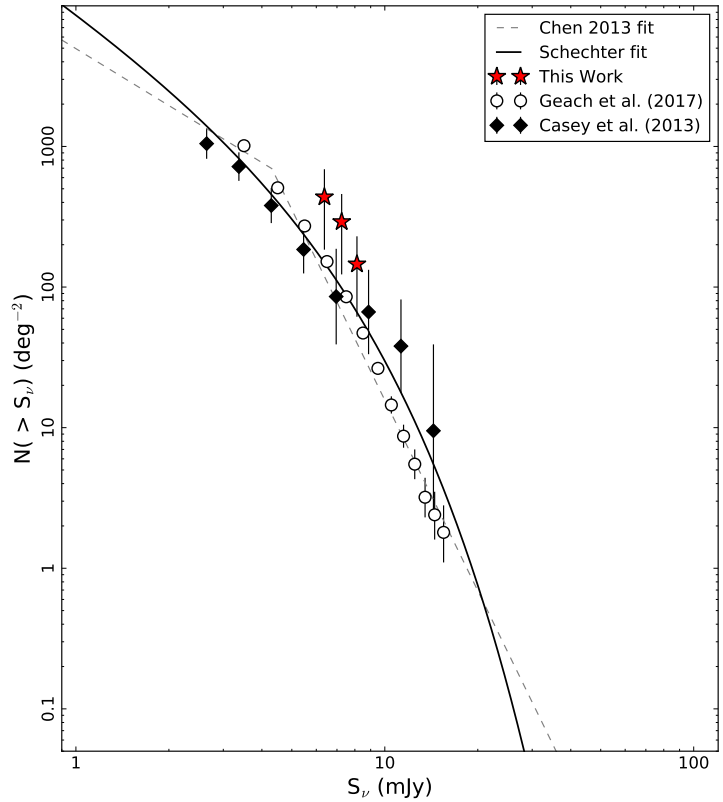

Fig. 4.9 Cumulative frequency of number counts for serendipitous >4σ detections within 1.5 arcmin radius of the reddened quasar targets (red stars), compared to blank field counts from Geach et al. (2017) (open circles) and Casey et al. (2013) (solid diamonds), averaged only over the area of the seven maps in which we detect serendipitous sources >4σ. Discrepancy between our reddened quasar sample and blank fields indicates an environmental overdensity in several of the quasars in our sample.

et al., 2017) and therefore seven of the 19 quasars in our sample (37 per cent) may well be associated with sub-mm overdensities.

4.4 DISCUSSION

4.4.1 ALMA OBSERVATIONS

Two of the reddened quasars in our sample (ULASJ1234+0907 and ULASJ2315+0143) have also been observed with the Atacama Large Millimetre/ submillimetre Array (ALMA) (Banerji et al., 2017, 2018), measuring the 1.24mm and 2.92mm continuum photometry. With the higher resolution of the ALMA observations ($\sim$3 arcsec compared to $\sim$15 arcsec

with SCUBA-2), it is possible to spatially resolve these two sources, finding them to be comprised of multiple sources in both ULASJ1234+0907 and ULASJ2315+0143 (Fig. 4.10). In addition to the continuum emission, ALMA detects multiple molecular lines and thus can be used to determine the redshifts of these sources lying within a 1.5 arcmin radius of the NIR quasar positions. In both ULASJ1234+0907 and ULASJ2315+0143, the sources marked in Fig. 4.10 are found to lie at a similar redshift to the quasar, meaning they do not just appear close in the plane of the image but rather are physically associated with one another. This provides direct evidence that at least some fraction of the reddened quasars in our sample reside in high density sub-mm environments. Furthermore, we note that ULASJ1234+0907 is undetected with SCUBA-2, lying below the $>3\sigma$ detection limit of our sample, yet the two companion galaxies near the quasar are shown to have higher 850μm flux densities of 7.481 mJy (3.6σ) and 5.922 mJy (2.8σ). The detection of multiple sources associated with the quasar may indicate merger activity in these systems, consistent with our reddened quasar sample being in the evolutionary phase suggested by Sanders et al. (1988) in which these systems are evolving from merger-induced starburst galaxies.

We note that not all the sources seen in the SCUBA-2 images will merge with the quasar in this way. No redshift or velocity information is currently available for the serendipitous detections in Fig. 4.8, meaning it is highly likely that some fraction of these detections lie in either the foreground or background of the quasar image. Furthermore, were the detections to be at a similar redshift to the quasar and thus part of the same overdensity, simulations suggest that galaxies would require a velocity separation $<$500kms^{-1} in order to be classed as merging systems (e.g. Hopkins et al., 2006). The 1.5 arcmin radius over which we search for overdensities also corresponds to physical scales $\sim$700kpc. Even assuming the quasars in our sample reside in the most massive halos at z$\sim$2 ($M_{halo} \sim 2\times10^{13}$), the virial radius of the halo would only extend to $\sim$200kpc - much lower than the $\sim$700kpc considered. Objects outside this radius will never merge with the quasar, regardless how close they are in velocity or redshift space. In fact, many simulations (e.g. Hopkins et al., 2006) suggest merging galaxy pairs to be defined as having separations $\lesssim$20kpc.

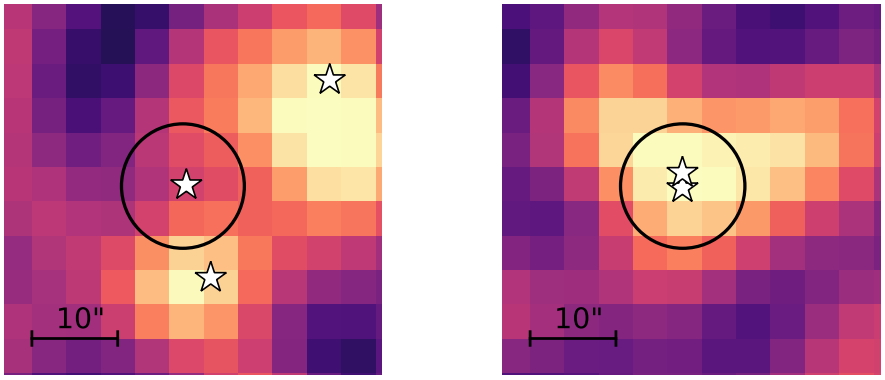

(a) ULASJ1234+0907 **(b)** ULASJ2315+0143

Fig. 4.10 850μm SCUBA-2 maps for the two sources in our sample also observed with ALMA - ULASJ1234+0907 and ULASJ2315+0143. White stars denote the location of individual sources detected with higher-resolution ALMA data (Banerji et al., 2017).

Fig. 4.10 shows that both the ALMA sources detected in the map of ULASJ2315+0143 lie within the beamsize of SCUBA-2, meaning that the SCUBA-2 photometry derived for this source is effectively the sum of these two ALMA sources. We overlay the sum of the photometry for the two ALMA sources at 1.24mm and 2.92mm in Fig. 4.11. At 2.92mm, the combined photometry lies above that predicted by the greybody fit, potentially indicating contamination from synchrotron emission, which has been shown to be present in this source (Banerji et al., 2018). The discrepancy between the 1.24mm photometry and the greybody template may also indicate that the assumptions made about T_{eff} and β in the fitting are incorrect. Together with the 850μm SCUBA-2 detection, the 1.24mm ALMA photometry suggests a steeper β may be required.

4.4.2 COMPARISONS WITH DIFFERENT QUASAR POPULATIONS

This section aims to put our reddened quasar sample in the context of the broader quasar population. In particular, we seek to compare the detection rates and environments of UV-bright ($A_v \sim 0$ mags) and mid-IR luminous, heavily obscured ($A_v \gtrsim 15$ mags) to our sample ($A_v \sim$ 2-6 mags).

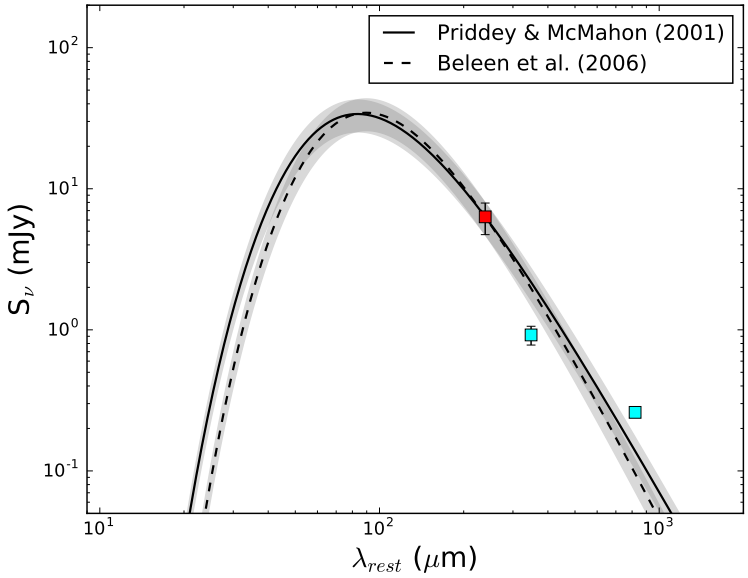

Fig. 4.11 Grey-body fit to the 850μm photometry of ULASJ2315+0143 as a function of wavelength assuming (i) T=47K, β=1.6 (Priddey and McMahon, 2001) *(solid)* and (ii) T=41K, β=1.95 (Beelen et al., 2006) *(dashed)* with 1.24mm and 2.92mm photometry from ALMA overlaid *(cyan points)*. Shaded regions represent the 1σ uncertainty on each fit.

4.4.3 UV-BRIGHT QUASARS

Fig. 4.12 compares the redshifts and dust-corrected bolometric quasar luminosities, L_{bol}, for a sample of UV-bright quasars observed with SCUBA at 850μm (Priddey et al., 2003) with those of our quasar sample. In the case of our sample, L_{bol} is derived from the dust-corrected flux at 5100Å, applying a bolometric correction factor of 7 as outlined in Vestergaard and Peterson (2006). In general, we find our sample to be intrinsically fainter.

Priddey et al. (2003) detect nine of the 57 UV-luminous quasars ($A_v \sim 0$ mags) in their sample (16 per cent) at a significance $>3\sigma$, corresponding to a flux limit of 10mJy at 850μm. In section 4.3.1, we show just one quasar in our sample - ULASJ1216-0313 - to lie above this same flux limit (5 per cent of our sample). We note however that the median dust-corrected L_{bol} of our quasar sample is $10^{47.2}$ ergs^{-1}, compared to $10^{47.7}$ ergs^{-1} in the sample of Priddey et al. (2003) and thus the lower sub-mm detection rate of our sample may be explained by the higher luminosity of the the sample in Priddey et al. (2003). Furthermore, at L_{bol} $>$ 47.5 ergs^{-1} - a luminosity threshold above which all detections in Priddey et al. (2003)

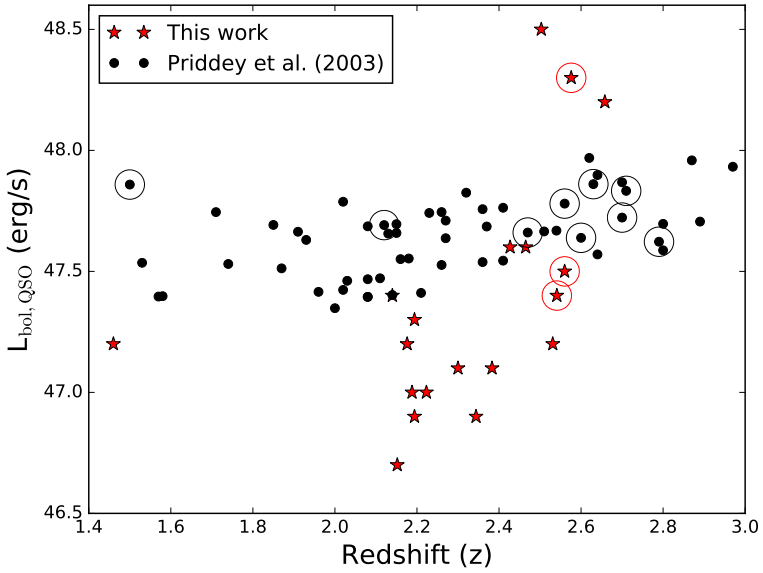

Fig. 4.12 A comparison of the bolometric quasar luminosities (L_{bol}) of our quasar sample (*red stars*) and the UV-luminous quasar sample of Priddey et al. (2003) (*black dots*). Circles denote all detected sources ($>3\sigma$) in each sample, corresponding to a flux limit of >4.8mJy in our sample and >10mJy in that of Priddey et al. (2003). All quoted luminosities have been corrected for the effect of obscuration by dust.

lie - we find five quasars in our sample, of which one is detected with a $>3\sigma$ significance, corresponding to a 20 per cent detection rate in this luminosity range. Nine of the 45 quasar targets lying above the same luminosity threshold in the UV-luminous sample (Priddey et al., 2003) are detected, also corresponding to a detection rate of 20 per cent. We therefore conclude that the difference we observe in the detection rate of obscured and UV-luminous quasars is likely due to the luminosity difference of the two samples considered.

4.4.4 HOTDOGS

Two studies by Jones et al. (2015, 2014) investigate the 850μm properties of dusty, luminous galaxies at z$\sim$1.7-4.6 selected from the WISE all-sky survey. These galaxies, dubbed Hot Dust-Obscured Galaxies (HotDOGs), typically have a dust reddening of $A_v \gtrsim 15$ mags - significantly larger than the intermediate reddening of the quasars presented in this chapter, which have dust extinctions $A_v \sim 2$ - 6 mags. Fig 4.13 compares the redshifts and 22μm (W4) magnitudes for each of the HotDOG samples with that of the quasars in this chapter. To make a direct comparison between the two populations, we consider only the HotDOGs

with known redshifts matching the range of our sample ($1.4 < z < 3$). In Jones et al. (2015) none of the targeted quasars lying in this redshift range are detected at 850μm with a flux limit $>$ 6.3mJy, corresponding to the $>3\sigma$ detection threshold of their sample. Above this same flux we detect two quasars in our sample ($\sim$10 per cent), which we consider consistent with the detection rate of Jones et al. (2015) given the small sample sizes. In Jones et al. (2014), where WISE-selected quasars are additionally required to contain a compact radio source, four of the seven quasars lying at $1.4 < z < 3$ (57 per cent) are detected above a 3σ flux limit of $>$5.8mJy. Comparing this to the 850μm detection rate of our sample, we find just three of the 19 quasars ($\sim$16 per cent) to lie above the same flux limit, although we note that synchrotron emission could be contributing to the observed sub-mm flux in the radio-loud sources of Jones et al. (2014). In fact, Kalfountzou et al. (2017) find sources with flux densities $\gtrsim$ 7-10mJy at 1300μm show significant contamination from radio emission. If this threshold is applied at 850μm (Eqn. 4.6), i.e.

$$\beta \times log_{10}\Big(\frac{S_{1300}}{S_{850}}\Big), \tag{4.6}$$

where S_{1300} and S_{850} are the flux densities at 1300 and 850 μm respectively (mJy) and β denotes the slope of the SED, we find objects with $S_{850} >$ 9-13 mJy likely have some contamination from non-thermal sources. Three of the ten sources presented in Jones et al. (2014) lie above this threshold, indicating that radio contamination may be an issue in these objects.

When we consider only the quasars with a 22μm (W4) magnitude brighter than 8.0 (Vega), above which the entire Jones et al. (2015, 2014) samples lie, we find the detection rate of our sample to increase to 43 per cent. We therefore conclude the detection rate among the most luminous quasars in our sample to be consistent with that of radio-loud HotDOGs. None of the three Jones et al. (2015) quasars brighter than 8.0 mags (Vega) are detected, but the small sample size means we cannot infer whether or not our sample does indeed have a higher detection rate than the HotDogs sample in Jones et al. (2015).

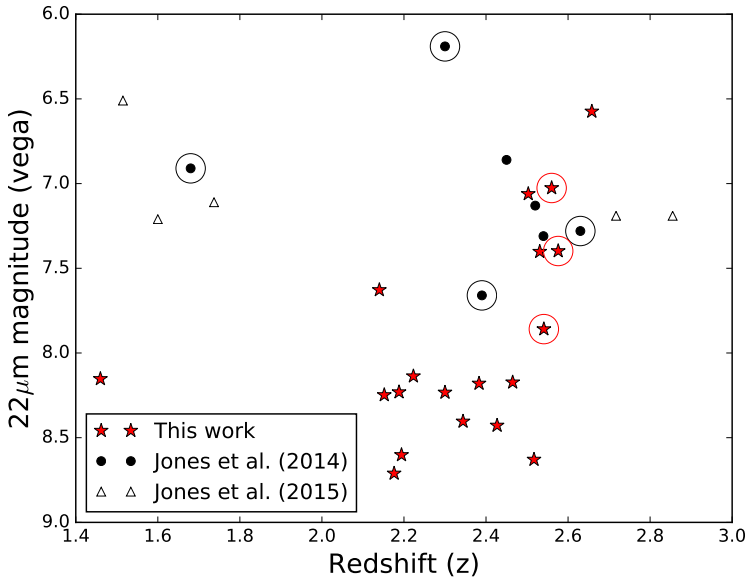

Fig. 4.13 A comparison of the WISE 22μm magnitudes (vega) of our quasar sample (*red stars*) and the HotDOGs in Jones et al. (2014) (*black dots*) and Jones et al. (2015) (*hollow triangles*). Circles denote all detected sources ($>3\sigma$) in each sample, corresponding to a flux limit of >4.8mJy in our sample and >5.8mJy and >6.3mJy in Jones et al. (2014) and Jones et al. (2015) respectively.

In section 4.3.3, we compare the environments of our quasar sample with the sub-mm blank fields, finding little evidence for an overdensity in the average environments of reddened quasars at 850μm. Jones et al. (2015, 2014) perform similar tests, comparing the number of detections within 1.5 arcmin of their quasar targets with the sub-mm blank fields (Weiß et al., 2009). Both Jones et al. (2014) and Jones et al. (2015) find an overdensity in the sub-mm environments of extremely reddened quasars compared to the blank fields. In Jones et al. (2014), they find an environmental overdensity of a factor 2.6 ± 0.7 compared to the blank field, finding 15 serendipitous sources within the 70.7 arcmin^2 survey area. In Jones et al. (2014), this overdensity factor increases to 6.3 ± 1.1, finding 81 serendipitous detections in an area of 212.0 arcmin^2. Whilst this may indicate an environmental overdensity compared to our quasar sample, we note that this is based on the full samples in Jones et al. (2015, 2014), many of which lie outside of the redshift range of our sample ($1.4 < z < 3$). Due to this disparity across the different samples, we cannot reliably compare the environments of our sample with those in Jones et al. (2015, 2014).

4.5 CONCLUSIONS

In this chapter, we have presented new, targeted 850μm SCUBA-2 observations for a sample of 19 dust-reddened quasars ($A_\nu \sim$ 2-6 mags) at $1.4 \leq z \leq 2.7$ - a peak epoch of both star formation and black hole accretion. From this work, we draw the following conclusions;

(i) There is evidence for prodigious dust obscured star formation in three of the 19 reddened quasars in our sample, finding SFRs ranging 2400 - 4600 $M_\odot yr^{-1}$. Whilst the remainder of the quasar sample is undetected at 850μm, this does not preclude high levels of star formation in these systems. Indeed, the stacked non-detections return an average 3σ upper limit on the SFR of 990 $M_\odot yr^{-1}$. Deeper observations from instruments such as ALMA are therefore required to measure the obscured star formation in these systems.

(ii) On average, we find no evidence for overdensities in the sub-mm environments of reddened quasars at z$\sim$2. We note however that several individual quasars in our sample show some evidence that they lie in overdense regions, finding at least one $>4\sigma$ source within a 1.5 arcmin radius of seven quasar targets. When averaging over only the maps in which we detect sources with confidence $>4\sigma$, we find an overdensity of factor $\sim$3 when compared to the blank fields. Furthermore, ALMA observations of two quasars in our sample ULASJ1234+0907 and ULASJ2315+0143 (Banerji et al., 2018) reveal them to be comprised of multiple sources at the same redshifts as the quasars, reinforcing the evidence for a potential overdensity in the environments of individual objects in our obscured quasar sample.

(iii) Overall, the moderately reddened quasars considered in our sample appear to reside in less dense environments than more heavily reddened quasars, sometimes referred to as HotDOGS. Whilst luminous quasars with $A_\nu \gtrsim 15$ mags have been found to reside in sub-mm environments a factor of 2.6 times denser than the sub-mm blank field, our sample shows no such overdensity. We note however that the overdensity found in the HotDOG samples include objects spanning a much wider range of redshifts than our sample and so a direct environmental comparison of these two populations is not possible.

(iv) We find the 850μm detection rate of our obscured quasar sample to be consistent with a population of more heavily obscured HotDOGs at similar redshift. In HotDOGs containing radio sources the detection rate is significantly higher, although we note that this may be due to contamination by synchrotron radiation in the sub-mm emission of these radio-loud systems. The detection rate of UV-luminous quasars is also found to be higher than that of our sample, with 16 per cent of UV-luminous quasars detected $>$10mJy at 850μm compared to just 5 per cent of our sample. When considering only the brightest quasars in our sample however, we find the detection rate to be consistent with both UV-luminous quasars and radio-loud HotDOGs, implying that the detection rate is largely dependent on the average quasar luminosity of the sample. In general therefore, we conclude there to be no significant differences between our reddened quasar sample and either the UV-luminous (Priddey et al., 2003) or HotDOGs populations (Jones et al., 2015, 2014) in terms of their sub-mm emission. If the reddened quasars in our sample are undergoing a blowout phase, as suggested by Sanders et al. (1988), we would expect to observe significant differences in their sub-mm properties compared to UV-luminous quasars and HotDOGs, as obscured quasars are though to be much more highly star-forming than their unobscured counterparts. The fact that we see no such differences implies that this might not be the case. We highlight however, that the sample size considered in this work is relatively small, and comparison samples have not been robustly matched in redshift and luminosity. We also note that this comparison is based on the assumption that the sub-mm emission is tracing the obscured star formation in these galaxies, yet we suggest that radio contamination is likely a problem in at least some fraction of the Jones et al. (2014) sample. Contamination from the quasar itself may also heavily influence the inferred SFR of these galaxies.

In the future, spatially-resolved images of the dust in this quasar sample, such as ALMA observations, will dramatically improve our understanding of the obscured star formation in reddened quasar hosts. Spectroscopic follow-up and accurate redshift estimates for the serendipitous sources across our survey region will also shed light on the sub-mm environments of our sample, allowing us to distinguish between objects spatially correlated with our quasar targets and those lying along the line of sight.

CHAPTER 5

SUMMARY AND FUTURE WORK

This thesis has focussed on characterising the host galaxies of a class of highly luminous yet heavily obscured quasars at z$\sim$2. In particular, we have explored the connection between star formation and quasar activity across multiple wavelengths through three distinct projects, each with the common aim of placing the most luminous reddened quasars in the context of the general quasar population. This final chapter provides a summary of each project, highlighting the key results. Potential directions in which to expand this research in the future are suggested in Section 5.4.

5.1 REDDENED QUASAR HOSTS IN THE UV

Separating quasar emission from that of its host galaxy has long proven challenging, particularly among the most luminous quasars. Typically, astronomers have relied on observations at sub-mm wavelengths, where reprocessed light from star formation dominates, or have required high-resolution space-based imaging to accurately subtract the point spread function. In the rest-frame UV, studies have largely been limited to low redshift, where high spatial resolution is easier to achieve. At higher redshifts (z$\sim$2), where both star formation and black hole accretion has been shown to peak, studies have been limited to individual objects. At this key epoch, we perform the first population study of high-luminosity, reddened quasars

in the rest-frame UV using the first year of deep ground-based observations from DES. By combining the rest-frame UV photometry with NIR data from VISTA and ULAS, we develop an SED-fitting routine to disentangle the quasar emission from that of its host galaxy. By exploiting dust obscuration towards the quasar, we are able to separate these two components and directly probe the unobscured star formation in the host galaxies of the most luminous quasars, finding luminous reddened quasars to reside in prodigiously star forming hosts at $z\sim2$. When these measured SFRs are compared to the intrinsic quasar luminosities of our sample (L_{bol}), we find evidence for a correlation between quasar luminosity and the UV-derived SFR. Although we note that such a correlation may only exist within the populations of very luminous and obscured quasars probed in this work, the existence of such a relation could imply that the same gas supply is fuelling both black hole acretion and star formation in this class of objects.

5.2 A MORPHOLOGICAL STUDY OF REDDENED QUASAR HOSTS AT $z\sim2$

Understanding star formation in quasar host galaxies is key to constraining models of galaxy - quasar coevolution. Modelling the restframe UV emission from quasar hosts, tracing the emission from young stars in the galaxy, has proven challenging in 2D, particularly among populations of very luminous quasars whose light dominate that of the host over multiple passbands. For this reason, 2D modelling of quasar hosts has largely relied on space-based imaging, with attempts using ground-based imaging typically limited to either low redshift systems ($z\lesssim0.2$) or populations of low luminosity quasars. A key issue facing such studies of bright quasars, particularly with ground-based imaging, is the separation of the galaxy and quasar light in the image. Having demonstrated that this separation can be achieved in 1D by exploiting dust obscuration among populations of reddened quasars, we test whether this can also be applied to model these systems in 2D based on imaging from DES Y3. To this end, we make use of a multi-band image fitting code, placing constraints on the galaxy and quasar in the bands in which they dominate. From the fitting, we return models providing a good

description of the DES Y3 observations, inferring galaxy and quasar magnitudes broadly consistent with those returned from the SED fitting in several objects. In cases where the two methods appear to disagree, we suggest the disagreement is likely due to the lack of constraint on the galaxy and quasar colours in the 2D modelling. By simulating a range of quasars with different brightnesses in low-redshift galaxies with similar colours to our sample, we find galaxy properties (i.e. the position of the galaxy in the image, (X,Y), its radius, R_{eff}, axis ratio, q_{GAL}, angle of orientation, θ, and Sérsic index, n) can be accurately returned for a significant portion of our sample. Therefore, modelling z$\sim$2 luminous quasar hosts in 2D is possible with multi-band fitting of data from currents ground-based surveys such as DES, opening the door to future morphological studies of these systems.

5.3 REDDENED QUASAR HOSTS IN THE SUB-MM

At sub-mm wavelengths ($\sim$100μm-1mm), thermal emission from cold dust peaks, making this the perfect regime in which to probe the dust heated by star formation and thus the dust-obscured star formation in the galaxy. Using targeted observations from SCUBA-2, we trace the 850μm emission for a sample of 19 moderately obscured ($A_V \sim$ 2-6 mags) quasars, finding direct evidence for prodigious star formation of $>$2400 $M_\odot yr^{-1}$ in three of the quasar targets. In the remainder of the sample we also do not preclude high levels of obscured star formation, deriving a 3σ upper limit on the SFR of 990 $M_\odot yr^{-1}$ from the stacked image of the non-detections. These high SFRs are consistent with those expected of quasars in a transitional phase between a starburst galaxy and a UV-luminous quasar and thus we conclude our findings to align with this idea. The sub-mm detection rate of our sample is consistent with that of more heavily-obscured HotDOG galaxies ($A_V > 15$ mags), but falls below that of radio-loud samples, likely due to contamination in the 850μm emission of these sources from synchrotron radiation. The sub-mm detection rate of reddened quasars are also shown to be consistent with UV-luminous quasars once the two samples have been matched in both luminosity and redshift.

Overdense environments may be an indication of merger events and thus provide further validation that obscured quasars are in an evolutionary phase following a merger-driven starburst. Whilst we find no indication of an environmental overdensity over our sample as a whole, we demonstrate that several individual objects appear to reside in overdense regions of the sky (a factor $\sim$3 times denser than sub-mm blank fields). Indeed, independent ALMA observations for two quasars in our sample reveal multiple sub-mm sources are associated with each quasar, reinforcing the conclusion that several of the obscured quasars considered here exist in overdense environments. When we compare this to the environments of more heavily-obscured HotDOG galaxies ($A_\nu > 15$ mags), we find the environmental density of HotDOGs to be $\sim$ 2-5 times higher than that of our sample, although we note that this may be due in part to the differences in the quasar luminosity and redshift between the two samples.

5.4 FUTURE PROSPECTS

In Chapter 2, we explore the relation between the unobscured star formation, traced by the rest-frame UV emission, and the quasar luminosity in a sample of highly luminous, dust obscured quasars at z$\sim$2. In general, we conclude the most luminous obscured quasars to reside in the most actively star-forming galaxies. The sample of reddened quasars considered in this work however covers only a narrow range of quasar luminosities ($>10^{46}$erg s^{-1}) and several studies suggest this trend to disappear among lower-luminosity quasar populations (e.g Urrutia et al., 2012). Moving forward, we seek to investigate how this relationship between unobscured star formation and quasar luminosity varies as a function of the quasar luminosity. Already, a new sample of heavily-reddened quasars has been identified in the VIKING survey (Temple et al. 2018 *in prep.*), meaning the fitting techniques outlined in Chapter 2 can be directly applied to this new data set to make similar inferences on lower-luminosity quasar systems.

Chapter 3 outlines a method for modelling the restframe UV emission in hosts of z$\sim$2 luminous quasars in 2D. By including the ability to model multiple objects in an image

and incorporating constraints on the colours of the galaxy and quasar components in the model, based on their SEDs, we hope to improve our ability to model these systems in the future. The 'pilot study' in Chapter 3 demonstrates that host glaxy paremeters can be derived for high redshift obscured quasars using the current generation of ground-based imaging surveys.

At FIR/ sub-mm wavelengths, observations from Herschel Spectral and Photometric Imaging REceiver (SPIRE) may be used to further constrain the obscured SFRs of reddened quasars at z$\sim$2. The SPIRE wavebands lie at 250, 350 and 500μm, meaning they trace the 'bump' of the reprocessed emission from star formation. Combined with the 850μm photometry from SCUBA-2 (Chapter 4), Herschel data can be used to place more constraints on the SED template fitted to this region of the spectrum and thus provide a better measure of the obscured star formation in reddened quasars.

With ongoing observations from ALMA, we also hope to obtain more sensitive observations of z$\sim$2 reddened quasars in the sub-mm. A primary motivation behind these observations is to determine the source of the sub-mm emission in these objects. In Chapter 4, we assume all the sub-mm emission observed at 850μm with SCUBA-2 to arise from the heating of dust by stars, yet luminous quasars themselves may be partially responsible for heating the dust causing this emission. If sub-mm emission is indeed tracing the star formation, we would expect to observe statistical differences in the properties of obscured and unobscured quasar populations in the sub-mm, as obscured quasars are thought to be more highly star-forming than their unobscured counterparts. If however a substantial fraction of the sub-mm emission arises from the dust heated by the quasar, one would instead expect to observe very similar sub-mm properties in the two quasar populations, providing they have similar quasar luminosities. Making direct comparisons between the sub-mm properties of obscured and unobscured z$\sim$2 quasar hosts is therefore a good way to investigate the source of the emission at sub-mm wavelengths. Already, large spectroscopic samples of both obscured and unobscured quasars have been identified at this epoch (Banerji et al., 2015a, 2012; Pâris et al., 2018), providing an excellent base sample with which to carry out this study.

REFERENCES

Abbott, T., Abdalla, F., Alarcon, A., Aleksić, J., Allam, S., Allen, S., Amara, A., Annis, J., Asorey, J., Avila, S., et al. (2017). Dark energy survey year 1 results: Cosmological constraints from galaxy clustering and weak lensing. *arXiv preprint arXiv:1708.01530*.

Abbott, T., Abdalla, F., Aleksić, J., Allam, S., Amara, A., Bacon, D., Balbinot, E., Banerji, M., Bechtol, K., Benoit-Lévy, A., et al. (2016). The dark energy survey: more than dark energy–an overview. *Monthly Notices of the Royal Astronomical Society*, 460(2):1270–1299.

Aird, J., Coil, A. L., Georgakakis, A., Nandra, K., Barro, G., and Pérez-González, P. G. (2015). The evolution of the x-ray luminosity functions of unabsorbed and absorbed agns out to z$\sim$ 5. *Monthly Notices of the Royal Astronomical Society*, 451(2):1892–1927.

Alaghband-Zadeh, S., Banerji, M., Hewett, P. C., and McMahon, R. G. (2016a). Heavily reddened z$\sim$ 2 type 1 quasars–ii. h α star formation constraints from sinfoni ifu observations. *Monthly Notices of the Royal Astronomical Society*, 459(1):999–1017.

Alaghband-Zadeh, S., Banerji, M., Hewett, P. C., and McMahon, R. G. (2016b). Heavily reddened z$\sim$ 2 type 1 quasars–ii. h α star formation constraints from sinfoni ifu observations. *Monthly Notices of the Royal Astronomical Society*, 459(1):999–1017.

Antonucci, R. (1993). Unified models for active galactic nuclei and quasars. *Annual review of astronomy and astrophysics*, 31:473–521.

Armitage, P. J. and Natarajan, P. (2002). Accretion during the merger of supermassive black holes. *The Astrophysical Journal Letters*, 567(1):L9.

Assef, R. J., Eisenhardt, P. R., Stern, D., Tsai, C.-W., Wu, J., Wylezalek, D., Blain, A. W., Bridge, C. R., Donoso, E., Gonzales, A., et al. (2015). Half of the most luminous quasars may be obscured: Investigating the nature of wise-selected hot dust-obscured galaxies. *The Astrophysical Journal*, 804(1):27.

Bahcall, J. N., Kirhakos, S., Saxe, D. H., and Schneider, D. P. (1997). Hubble space telescope images of a sample of 20 nearby luminous quasars. *The Astrophysical Journal*, 479(2):642.

Banerji, M., Alaghband-Zadeh, S., Hewett, P. C., and McMahon, R. G. (2015a). Heavily reddened type 1 quasars at z> 2–i. evidence for significant obscured black hole growth at the highest quasar luminosities. *Monthly Notices of the Royal Astronomical Society*, 447(4):3368–3389.

Banerji, M., Carilli, C., Jones, G., Wagg, J., McMahon, R., Hewett, P., Alaghband-Zadeh, S., and Feruglio, C. (2017). The discovery of gas-rich, dusty starbursts in luminous reddened quasars at z$\sim$ 2.5 with alma. *Monthly Notices of the Royal Astronomical Society*, 465(4):4390–4405.

Banerji, M., Fabian, A., and McMahon, R. (2014). Ulasj1234+ 0907: the reddest type 1 quasar at z= 2.5 revealed in the x-ray and far-infrared. *Monthly Notices of the Royal Astronomical Society: Letters*, 439(1):L51–L55.

Banerji, M., Jones, G. C., Wagg, J., Carilli, C. L., Bisbas, T. G., and Hewett, P. C. (2018). The interstellar medium properties of heavily reddened quasars & companions at z$\sim$ 2.5 with alma & jvla. *Monthly Notices of the Royal Astronomical Society*.

Banerji, M., McMahon, R. G., Hewett, P. C., Alaghband-Zadeh, S., Gonzalez-Solares, E., Venemans, B. P., and Hawthorn, M. J. (2012). Heavily reddened quasars at z$\sim$ 2 in the ukidss large area survey: a transitional phase in agn evolution. *Monthly Notices of the Royal Astronomical Society*, 427(3):2275–2291.

Banerji, M., McMahon, R. G., Hewett, P. C., Gonzalez-Solares, E., and Koposov, S. E. (2013). Hyperluminous reddened broad-line quasars at z$\sim$ 2 from the vista hemisphere survey and wise all-sky survey. *Monthly Notices of the Royal Astronomical Society: Letters*, 429(1):L55–L59.

Banerji, M., McMahon, R. G., Willott, C., Geach, J., Harrison, C., Alaghband-Zadeh, S., Alexander, D., Bourne, N., Coppin, K., Dunlop, J., et al. (2015b). Cold dust emission from x-ray agn in the scuba-2 cosmology legacy survey: dependence on luminosity, obscuration and agn activity. *Monthly Notices of the Royal Astronomical Society*, 454(1):419–438.

Barnes, J. E. and Hernquist, L. E. (1991). Fueling starburst galaxies with gas-rich mergers. *The Astrophysical Journal*, 370:L65–L68.

Barthel, P. D. (1989). Is every quasar beamed? *The Astrophysical Journal*, 336:606–611.

Beelen, A., Cox, P., Benford, D. J., Dowell, C. D., Kovács, A., Bertoldi, F., Omont, A., and Carilli, C. L. (2006). 350 μm dust emission from high-redshift quasars. *The Astrophysical Journal*, 642(2):694.

Bennert, V. N., Auger, M. W., Treu, T., Woo, J.-H., and Malkan, M. A. (2011). The relation between black hole mass and host spheroid stellar mass out to z$\sim$ 2. *The Astrophysical Journal*, 742(2):107.

Benson, A., Bower, R., Frenk, C., Lacey, C. G., Baugh, C., and Cole, S. (2003). What shapes the luminosity function of galaxies? *The Astrophysical Journal*, 599(1):38.

Böehringer, H., Voges, W., Fabian, A., Edge, A., and Neumann, D. (1993). A rosat hri study of the interaction of the x-ray-emitting gas and radio lobes of ngc 1275. *Monthly Notices of the Royal Astronomical Society*, 264(1):L25–L28.

Bond, J., Cole, S., Efstathiou, G., and Kaiser, N. (1991). Excursion set mass functions for hierarchical gaussian fluctuations. *The Astrophysical Journal*, 379:440–460.

Bongiorno, A., Zamorani, G., Gavignaud, I., Marano, B., Paltani, S., Mathez, G., Møller, P., Picat, J., Cirasuolo, M., Lamareille, F., et al. (2007). The vvds type-1 agn sample: the faint end of the luminosity function. *Astronomy & Astrophysics*, 472(2):443–454.

Bower, R. G., Benson, A., Malbon, R., Helly, J., Frenk, C., Baugh, C., Cole, S., and Lacey, C. G. (2006). Breaking the hierarchy of galaxy formation. *Monthly Notices of the Royal Astronomical Society*, 370(2):645–655.

Boyce, P., Disney, M., Blades, J., Boksenberg, A., Crane, P., Deharveng, J., Macchetto, F., Mackay, C., and Sparks, W. (1998). Hst planetary camera images of quasar host galaxies. *Monthly Notices of the Royal Astronomical Society*, 298(1):121–130.

Bruzual, G. and Charlot, S. (2003). Stellar population synthesis at the resolution of 2003. *Monthly Notices of the Royal Astronomical Society*, 344(4):1000–1028.

Cai, Z., Fan, X., Noterdaeme, P., Wang, R., McGreer, I., Carithers, B., Bian, F., Miralda-Escudé, J., Finley, H., Pâris, I., et al. (2014). A glimpse at quasar host galaxy far-uv emission using damped lyα's as natural coronagraphs. *The Astrophysical Journal*, 793(2):139.

Calzetti, D., Armus, L., Bohlin, R. C., Kinney, A. L., Koornneef, J., and Storchi-Bergmann, T. (2000). The dust content and opacity of actively star-forming galaxiesbased on observations with iso, an esa project with instruments funded by esa member states (especially the pi countries: France, germany, the netherlands, and the united kingdom) with the participation of isas and nasa. *The Astrophysical Journal*, 533(2):682.

Cardelli, J. A., Clayton, G. C., and Mathis, J. S. (1989). The relationship between infrared, optical, and ultraviolet extinction. *The Astrophysical Journal*, 345:245–256.

Casey, C. M. (2012). Far-infrared spectral energy distribution fitting for galaxies near and far. *Monthly Notices of the Royal Astronomical Society*, 425(4):3094–3103.

Casey, C. M., Chen, C.-C., Cowie, L. L., Barger, A. J., Capak, P., Ilbert, O., Koss, M., Lee, N., Le Floc'h, E., Sanders, D. B., et al. (2013). Characterization of scuba-2 450 μm and 850 μm selected galaxies in the cosmos field. *Monthly Notices of the Royal Astronomical Society*, 436(3):1919–1954.

Chabrier, G. (2003). The galactic disk mass function: reconciliation of the hubble space telescope and nearby determinations. *The Astrophysical Journal Letters*, 586(2):L133.

Chapin, E. L., Berry, D. S., Gibb, A. G., Jenness, T., Scott, D., Tilanus, R. P., Economou, F., and Holland, W. S. (2013). Scuba-2: iterative map-making with the sub-millimetre user reduction facility. *Monthly Notices of the Royal Astronomical Society*, 430(4):2545–2573.

Charlot, S. and Fall, S. M. (2000). A simple model for the absorption of starlight by dust in galaxies. *The Astrophysical Journal*, 539(2):718.

Chen, C.-T. J., Hickox, R. C., Alberts, S., Brodwin, M., Jones, C., Murray, S. S., Alexander, D. M., Assef, R. J., Brown, M. J., Dey, A., et al. (2013). A correlation between star formation rate and average black hole accretion in star-forming galaxies. *The Astrophysical Journal*, 773(1):3.

Cisternas, M., Jahnke, K., Inskip, K. J., Kartaltepe, J., Koekemoer, A. M., Lisker, T., Robaina, A. R., Scodeggio, M., Sheth, K., Trump, J. R., et al. (2010). The bulk of the black hole growth since z 1 occurs in a secular universe: no major merger-agn connection. *The Astrophysical Journal*, 726(2):57.

Collins, C. A., Stott, J. P., Hilton, M., Kay, S. T., Stanford, S. A., Davidson, M., Hosmer, M., Hoyle, B., Liddle, A., Lloyd-Davies, E., et al. (2009). Early assembly of the most massive galaxies. *Nature*, 458(7238):603.

Coppin, K., Swinbank, A., Neri, R., Cox, P., Alexander, D., Smail, I., Page, M., Stevens, J., Knudsen, K., Ivison, R., et al. (2008). Testing the evolutionary link between submillimetre galaxies and quasars: Co observations of qsos at z$\sim$ 2. *Monthly Notices of the Royal Astronomical Society*, 389(1):45–62.

Cowie, L. L., Songaila, A., Hu, E. M., and Cohen, J. (1996). New insight on galaxy formation and evolution from keck spectroscopy of the hawaii deep fields. *arXiv preprint astro-ph/9606079*.

Croton, D. J., Springel, V., White, S. D., De Lucia, G., Frenk, C. S., Gao, L., Jenkins, A., Kauffmann, G., Navarro, J., and Yoshida, N. (2006). The many lives of active galactic nuclei: cooling flows, black holes and the luminosities and colours of galaxies. *Monthly Notices of the Royal Astronomical Society*, 365(1):11–28.

Czerny, B., Li, J., Loska, Z., and Szczerba, R. (2004). Extinction due to amorphous carbon grains in red quasars from the sloan digital sky survey. *Monthly Notices of the Royal Astronomical Society*, 348(3):L54–L57.

De Vries, W., Becker, R., White, R., and Loomis, C. (2005). Structure function analysis of long-term quasar variability. *The Astronomical Journal*, 129(2):615.

Delvecchio, I., Lutz, D., Berta, S., Rosario, D., Zamorani, G., Pozzi, F., Gruppioni, C., Vignali, C., Brusa, M., Cimatti, A., et al. (2015). Mapping the average agn accretion rate in the sfr–m* plane for herschel-selected galaxies at $0< z\leq 2.5$. *Monthly Notices of the Royal Astronomical Society*, 449(1):373–389.

Desai, S., Armstrong, R., Mohr, J., Semler, D., Liu, J., Bertin, E., Allam, S., Barkhouse, W., Bazin, G., Buckley-Geer, E., et al. (2012). The blanco cosmology survey: Data acquisition, processing, calibration, quality diagnostics, and data release. *The Astrophysical Journal*, 757(1):83.

Di Matteo, T., Springel, V., and Hernquist, L. (2005). Energy input from quasars regulates the growth and activity of black holes and their host galaxies. *Nature*, 433(7026):604.

Diehl, H. et al. (2014). The dark energy survey and operations: year 1. Technical report, Fermi National Accelerator Laboratory (FNAL), Batavia, IL.

Draine, B. (2003). Scattering by interstellar dust grains. ii. x-rays. *The Astrophysical Journal*, 598(2):1026.

Drlica-Wagner, A., Sevilla-Noarbe, I., Rykoff, E., Gruendl, R., Yanny, B., Tucker, D., Hoyle, B., Rosell, A. C., Bernstein, G., Bechtol, K., et al. (2017). Dark energy survey year 1 results: Photometric data set for cosmology. *arXiv preprint arXiv:1708.01531*.

Dunlop, J., McLure, R., Kukula, M., Baum, S., O'Dea, C., and Hughes, D. (2003). Quasars, their host galaxies and their central black holes. *Monthly Notices of the Royal Astronomical Society*, 340(4):1095–1135.

Eisenhardt, P. R., Wu, J., Tsai, C.-W., Assef, R., Benford, D., Blain, A., Bridge, C., Condon, J., Cushing, M. C., Cutri, R., et al. (2012). The first hyper-luminous infrared galaxy discovered by wise. *The Astrophysical Journal*, 755(2):173.

Elitzur, M. and Shlosman, I. (2006). The agn-obscuring torus: The end of the "doughnut" paradigm? *The Astrophysical Journal Letters*, 648(2):L101.

Faber, S. and Jackson, R. E. (1976). Velocity dispersions and mass-to-light ratios for elliptical galaxies. *The Astrophysical Journal*, 204:668–683.

Fabian, A. (2012). Observational evidence of active galactic nuclei feedback. *Annual Review of Astronomy and Astrophysics*, 50:455–489.

Fan, L., Han, Y., Fang, G., Gao, Y., Zhang, D., Jiang, X., Wu, Q., Yang, J., and Li, Z. (2016). The most luminous heavily obscured quasars have a high merger fraction: Morphological study of wise-selected hot dust-obscured galaxies. *The Astrophysical Journal Letters*, 822(2):L32.

Ferrarese, L. and Ford, H. (2005). Supermassive black holes in galactic nuclei: past, present and future research. *Space Science Reviews*, 116(3-4):523–624.

Ferrarese, L. and Merritt, D. (2000). A fundamental relation between supermassive black holes and their host galaxies. *The Astrophysical Journal Letters*, 539(1):L9.

Flaugher, B., Diehl, H., Honscheid, K., Abbott, T., Alvarez, O., Angstadt, R., Annis, J., Antonik, M., Ballester, O., Beaufore, L., et al. (2015). The dark energy camera. *The Astronomical Journal*, 150(5):150.

Foreman-Mackey, D., Hogg, D. W., Lang, D., and Goodman, J. (2013). emcee: The mcmc hammer. *Publications of the Astronomical Society of the Pacific*, 125(925):306.

Francis, P. J., Hewett, P. C., Foltz, C. B., Chaffee, F. H., Weymann, R. J., and Morris, S. L. (1991). A high signal-to-noise ratio composite quasar spectrum. *The Astrophysical Journal*, 373:465–470.

Frieman, J., Collaboration, D. E. S., et al. (2013). The dark energy survey: Overview. In *American Astronomical Society Meeting Abstracts# 221*, volume 221.

Gallerani, S., Maiolino, R., Juarez, Y., Nagao, T., Marconi, A., Bianchi, S., Schneider, R., Mannucci, F., Oliva, T., Willott, C., et al. (2010). The extinction law at high redshift and its implications. *Astronomy & Astrophysics*, 523:A85.

Gaskell, C. M., Goosmann, R. W., Antonucci, R. R., and Whysong, D. H. (2004). The nuclear reddening curve for active galactic nuclei and the shape of the infrared to x-ray spectral energy distribution. *The Astrophysical Journal*, 616(1):147.

Geach, J., Dunlop, J., Halpern, M., Smail, I., van der Werf, P., Alexander, D., Almaini, O., Aretxaga, I., Arumugam, V., Asboth, V., et al. (2017). The scuba-2 cosmology legacy survey: 850 μm maps, catalogues and number counts. *Monthly Notices of the Royal Astronomical Society*, 465(2):1789–1806.

Gebhardt, K., Bender, R., Bower, G., Dressler, A., Faber, S., Filippenko, A. V., Green, R., Grillmair, C., Ho, L. C., Kormendy, J., et al. (2000). A relationship between nuclear black hole mass and galaxy velocity dispersion. *The Astrophysical Journal Letters*, 539(1):L13.

Glikman, E., Simmons, B., Mailly, M., Schawinski, K., Urry, C., and Lacy, M. (2015). Major mergers host the most-luminous red quasars at z$\sim$ 2: A hubble space telescope wfc3/ir study. *The Astrophysical Journal*, 806(2):218.

Graham, J., Fabian, A., and Sanders, J. (2008). The weak shock in the core of the perseus cluster. *Monthly Notices of the Royal Astronomical Society*, 386(1):278–288.

Grupe, D. (2004). A complete sample of soft x-ray-selected agns. ii. statistical analysis. *The Astronomical Journal*, 127(4):1799.

Gull, S. and Northover, K. (1973). Bubble model of extragalactic radio sources. *Nature*, 244(5411):80.

Gültekin, K., Richstone, D. O., Gebhardt, K., Lauer, T. R., Tremaine, S., Aller, M. C., Bender, R., Dressler, A., Faber, S., Filippenko, A. V., et al. (2009). The m-σ and ml relations in galactic bulges, and determinations of their intrinsic scatter. *The Astrophysical Journal*, 698(1):198.

Harris, K., Farrah, D., Schulz, B., Hatziminaoglou, E., Viero, M., Anderson, N., Béthermin, M., Chapman, S., Clements, D. L., Cooray, A., et al. (2016). Star formation rates in luminous quasars at 2< z< 3. *Monthly Notices of the Royal Astronomical Society*, 457(4):4179–4194.

Hastings, W. K. (1970). Monte carlo sampling methods using markov chains and their applications. *Biometrika*, 57(1):97–109.

Hatziminaoglou, E., Omont, A., Stevens, J., Amblard, A., Arumugam, V., Auld, R., Aussel, H., Babbedge, T., Blain, A., Bock, J., et al. (2010). Hermes: Far infrared properties of known agn in the hermes fields. *Astronomy & Astrophysics*, 518:L33.

Hewett, P. C., Warren, S. J., Leggett, S. K., and Hodgkin, S. T. (2006). The ukirt infrared deep sky survey zy jhk photometric system: passbands and synthetic colours. *Monthly Notices of the Royal Astronomical Society*, 367(2):454–468.

Holland, W., Bintley, D., Chapin, E., Chrysostomou, A., Davis, G., Dempsey, J., Duncan, W., Fich, M., Friberg, P., Halpern, M., et al. (2013). Scuba-2: the 10 000 pixel bolometer camera on the james clerk maxwell telescope. *Monthly Notices of the Royal Astronomical Society*, 430(4):2513–2533.

Hooper, E. J., Impey, C. D., and Foltz, C. B. (1997). Hubble space telescope imaging of $z \geq$ 0.4 quasar host galaxies selected by quasar radio and optical properties. *The Astrophysical Journal Letters*, 480(2):L95.

Hopkins, P. F., Hernquist, L., Cox, T. J., Di Matteo, T., Martini, P., Robertson, B., and Springel, V. (2005). Black holes in galaxy mergers: Evolution of quasars. *The Astrophysical Journal*, 630(2):705.

Hopkins, P. F., Hernquist, L., Cox, T. J., Di Matteo, T., Robertson, B., and Springel, V. (2006). A unified, merger-driven model of the origin of starbursts, quasars, the cosmic x-ray background, supermassive black holes, and galaxy spheroids. *The Astrophysical Journal Supplement Series*, 163(1):1.

Hopkins, P. F., Richards, G. T., and Hernquist, L. (2007). An observational determination of the bolometric quasar luminosity function. *The Astrophysical Journal*, 654(2):731.

Hunt, L. and Malkan, M. (1999). Morphology of the 12 micron seyfert galaxies. i. hubble types, axial ratios, bars, and rings. *The Astrophysical Journal*, 516(2):660.

Ishibashi, W. and Fabian, A. (2012). Active galactic nucleus feedback and triggering of star formation in galaxies. *Monthly Notices of the Royal Astronomical Society*, 427(4):2998–3005.

Ishibashi, W. and Fabian, A. C. (2014). How the central black hole may shape its host galaxy through agn feedback. *Monthly Notices of the Royal Astronomical Society*, 441(2):1474–1478.

Jahnke, K., Kuhlbrodt, B., and Wisotzki, L. (2004). Quasar host galaxy star formation activity from multicolour data. *Monthly Notices of the Royal Astronomical Society*, 352(2):399–415.

Jones, S. F., Blain, A. W., Lonsdale, C., Condon, J., Farrah, D., Stern, D., Tsai, C.-W., Assef, R. J., Bridge, C., Kimball, A., et al. (2015). Submillimetre observations of wise/radio-selected agn and their environments. *Monthly Notices of the Royal Astronomical Society*, 448(4):3325–3338.

Jones, S. F., Blain, A. W., Stern, D., Assef, R. J., Bridge, C. R., Eisenhardt, P., Petty, S., Wu, J., Tsai, C.-W., Cutri, R., et al. (2014). Submillimetre observations of wise-selected high-redshift, luminous, dusty galaxies. *Monthly Notices of the Royal Astronomical Society*, 443(1):146–157.

Kalfountzou, E., Stevens, J., Jarvis, M., Hardcastle, M., Wilner, D., Elvis, M., Page, M., Trichas, M., and Smith, D. (2017). Observational evidence that positive and negative agn feedback depends on galaxy mass and jet power. *Monthly Notices of the Royal Astronomical Society*, 471(1):28–58.

Kauffmann, G. and Heckman, T. M. (2009). Feast and famine: regulation of black hole growth in low-redshift galaxies. *Monthly Notices of the Royal Astronomical Society*, 397(1):135–147.

Kennicutt Jr, R. C. and Evans, N. J. (2012). Star formation in the milky way and nearby galaxies. *Annual Review of Astronomy and Astrophysics*, 50:531–608.

King, A. (2003). Black holes, galaxy formation, and the mbh-σ relation. *The Astrophysical Journal Letters*, 596(1):L27.

Kocevski, D. D., Faber, S., Mozena, M., Koekemoer, A. M., Nandra, K., Rangel, C., Laird, E. S., Brusa, M., Wuyts, S., Trump, J. R., et al. (2011). Candels: constraining the agn-merger connection with host morphologies at z 2. *The Astrophysical Journal*, 744(2):148.

Kolykhalov, P. and Sunyaev, R. (1984). Radiation of accretion disks in quasars and galactic nuclei. *Advances in space research*, 3(10-12):249–254.

Konigl, A. and Kartje, J. F. (1994). Disk-driven hydromagnetic winds as a key ingredient of active galactic nuclei unification schemes. *The Astrophysical Journal*, 434:446–467.

Kormendy, J., Dressler, A., Byun, Y.-I., Faber, S., Grillmair, C., Lauer, T., Richstone, D., and Tremaine, S. (1994). Hst photometry of the cores of early-type galaxies. In *European Southern Observatory Conference and Workshop Proceedings*, volume 49, page 147.

Kormendy, J. and Ho, L. C. (2013). Coevolution (or not) of supermassive black holes and host galaxies. *Annual Review of Astronomy and Astrophysics*, 51:511–653.

Kormendy, J. and Richstone, D. (1995). Inward bound—the search for supermassive black holes in galactic nuclei. *Annual Review of Astronomy and Astrophysics*, 33(1):581–624.

Krolik, J. H. and Begelman, M. C. (1988). Molecular tori in seyfert galaxies-feeding the monster and hiding it. *The Astrophysical Journal*, 329:702–711.

Kukula, M. J., Dunlop, J. S., McLure, R. J., Miller, L., Percival, W. J., Baum, S. A., and O'Dea, C. P. (2001). A nicmos imaging study of high-z quasar host galaxies. *Monthly Notices of the Royal Astronomical Society*, 326(4):1533–1546.

Lacey, C. and Cole, S. (1993). Merger rates in hierarchical models of galaxy formation. *Monthly Notices of the Royal Astronomical Society*, 262(3):627–649.

Liu, G., Zakamska, N. L., Greene, J. E., Nesvadba, N. P., and Liu, X. (2013). Observations of feedback from radio-quiet quasars–i. extents and morphologies of ionized gas nebulae. *Monthly Notices of the Royal Astronomical Society*, 430(3):2327–2345.

Lutz, D., Sturm, E., Tacconi, L., Valiante, E., Schweitzer, M., Netzer, H., Maiolino, R., Andreani, P., Shemmer, O., and Veilleux, S. (2008). Star formation in the hosts of high-z qsos: evidence from spitzer pah detections. *The Astrophysical Journal*, 684(2):853.

Lynden-Bell, D. (1969). Galactic nuclei as collapsed old quasars. *Nature*, 223(5207):690–694.

Lynden-Bell, D. and Rees, M. (1971). On quasars, dust and the galactic centre. *Monthly Notices of the Royal Astronomical Society*, 152(4):461–475.

MacLeod, C. L., Ivezić, Ž., Sesar, B., de Vries, W., Kochanek, C. S., Kelly, B. C., Becker, A. C., Lupton, R. H., Hall, P. B., Richards, G. T., et al. (2012). A description of quasar variability measured using repeated sdss and poss imaging. *The Astrophysical Journal*, 753(2):106.

Madau, P. and Dickinson, M. (2014). Cosmic star-formation history. *Annual Review of Astronomy and Astrophysics*, 52:415–486.

Maddox, N., Hewett, P. C., Péroux, C., Nestor, D. B., and Wisotzki, L. (2012). The large area kx quasar catalogue-i. analysis of the photometric redshift selection and the complete quasar catalogue. *Monthly Notices of the Royal Astronomical Society*, 424(4):2876–2895.

Maddox, N., Hewett, P. C., Warren, S., and Croom, S. (2008). Luminous k-band selected quasars from ukidss. *Monthly Notices of the Royal Astronomical Society*, 386(3):1605–1624.

Magorrian, J., Tremaine, S., Richstone, D., Bender, R., Bower, G., Dressler, A., Faber, S., Gebhardt, K., Green, R., Grillmair, C., et al. (1998). The demography of massive dark objects in galaxy centers. *The Astronomical Journal*, 115(6):2285.

Marconi, A. and Hunt, L. K. (2003). The relation between black hole mass, bulge mass, and near-infrared luminosity. *The Astrophysical Journal Letters*, 589(1):L21.

Matsuoka, Y., Strauss, M. A., Shen, Y., Brandt, W. N., Greene, J. E., Ho, L. C., Schneider, D. P., Sun, M., and Trump, J. R. (2015). The sloan digital sky survey reverberation mapping project: Post-starburst signatures in quasar host galaxies at z$<$ 1. *The Astrophysical Journal*, 811(2):91.

McLeod, K. and McLeod, B. (2001). Nicmos observations of low-redshift quasar host galaxies. *The Astrophysical Journal*, 546(2):782.

McLeod, K. and Rieke, G. (1995). Luminous quasars in luminous early-type host galaxies. *The Astrophysical Journal Letters*, 454(2):L77.

Mechtley, M., Jahnke, K., Windhorst, R., Andrae, R., Cisternas, M., Cohen, S., Hewlett, T., Koekemoer, A., Schramm, M., Schulze, A., et al. (2016). Do the most massive black holes at z= 2 grow via major mergers? *The Astrophysical Journal*, 830(2):156.

Metropolis, N., Rosenbluth, A. W., Rosenbluth, M. N., Teller, A. H., and Teller, E. (1953). Equation of state calculations by fast computing machines. *The journal of chemical physics*, 21(6):1087–1092.

Miyaji, T., Hasinger, G., Salvato, M., Brusa, M., Cappelluti, N., Civano, F., Puccetti, S., Elvis, M., Brunner, H., Fotopoulou, S., et al. (2015). Detailed shape and evolutionary behavior of the x-ray luminosity function of active galactic nuclei. *The Astrophysical Journal*, 804(2):104.

Mullaney, J., Alexander, D., Goulding, A., and Hickox, R. C. (2011). Defining the intrinsic agn infrared spectral energy distribution and measuring its contribution to the infrared output of composite galaxies. *Monthly Notices of the Royal Astronomical Society*, 414(2):1082–1110.

Mullaney, J., Pannella, M., Daddi, E., Alexander, D., Elbaz, D., Hickox, R., Bournaud, F., Altieri, B., Aussel, H., Coia, D., et al. (2012). Goods-herschel: the far-infrared view of star formation in active galactic nucleus host galaxies since z$\simeq$ 3. *Monthly Notices of the Royal Astronomical Society*, 419(1):95–115.

Netzer, H. (2009). Accretion and star formation rates in low-redshift type ii active galactic nuclei. *Monthly Notices of the Royal Astronomical Society*, 399(4):1907–1920.

Obied, G., Zakamska, N. L., Wylezalek, D., and Liu, G. (2016). Giant scattering cones in obscured quasars. *Monthly Notices of the Royal Astronomical Society*, 456(3):2861–2876.

Page, M., Stevens, J., Mittaz, J., and Carrera, F. (2001). Submillimeter evidence for the coeval growth of massive black holes and galaxy bulges. *Science*, 294(5551):2516–2518.

Page, M., Symeonidis, M., Vieira, J., Altieri, B., Amblard, A., Arumugam, V., Aussel, H., Babbedge, T., Blain, A., Bock, J., et al. (2012). The suppression of star formation by powerful active galactic nuclei. *Nature*, 485(7397):213.

Page, M. J., Stevens, J., Ivison, R., and Carrera, F. (2004). The evolutionary sequence of active galactic nuclei and galaxy formation revealed. *The Astrophysical Journal Letters*, 611(2):L85.

Pâris, I., Petitjean, P., Aubourg, É., Myers, A. D., Streblyanska, A., Lyke, B. W., Anderson, S. F., Armengaud, É., Bautista, J., Blanton, M. R., et al. (2018). The sloan digital sky survey quasar catalog: Fourteenth data release. *Astronomy & Astrophysics*, 613:A51.

Pei, Y. C. (1992). Interstellar dust from the milky way to the magellanic clouds. *The Astrophysical Journal*, 395:130–139.

Peng, C. Y., Ho, L. C., Impey, C. D., and Rix, H.-W. (2002). Detailed structural decomposition of galaxy images. *The Astronomical Journal*, 124(1):266.

Peng, C. Y., Impey, C. D., Ho, L. C., Barton, E. J., and Rix, H.-W. (2006). Probing the coevolution of supermassive black holes and quasar host galaxies. *The Astrophysical Journal*, 640(1):114.

Peterson, B. M. and Wandel, A. (2000). Evidence for supermassive black holes in active galactic nuclei from emission-line reverberation. *The Astrophysical Journal Letters*, 540(1):L13.

Pitchford, L. K., Hatziminaoglou, E., Feltre, A., Farrah, D., Clarke, C., Harris, K., Hurley, P., Oliver, S., Page, M., and Wang, L. (2016). Extreme star formation events in quasar hosts over $0.5< z< 4$. *Monthly Notices of the Royal Astronomical Society*, 462(4):4067–4077.

Priddey, R. S., Isaak, K. G., McMahon, R. G., and Omont, A. (2003). The scuba bright quasar survey (sbqs)—ii. unveiling the quasar epoch at submillimetre wavelengths. *Monthly Notices of the Royal Astronomical Society*, 339(4):1183–1188.

Priddey, R. S. and McMahon, R. G. (2001). The far-infrared–submillimetre spectral energy distribution of high-redshift quasars. *Monthly Notices of the Royal Astronomical Society*, 324(1):L17–L22.

Reddy, N. A., Steidel, C. C., Pettini, M., Adelberger, K. L., Shapley, A. E., Erb, D. K., and Dickinson, M. (2008). Multiwavelength constraints on the cosmic star formation history from spectroscopy: The rest-frame ultraviolet, hα, and infrared luminosity functions at redshifts $1.9\leq z\leq 3.4$. *The Astrophysical Journal Supplement Series*, 175(1):48.

Reed, S., McMahon, R., Martini, P., Banerji, M., Auger, M., Hewett, P., Koposov, S., Gibbons, S., Gonzalez-Solares, E., Ostrovski, F., et al. (2017). Eight new luminous $z>6$ quasars selected via sed model fitting of vista, wise and dark energy survey year 1 observations. *arXiv preprint arXiv:1701.04852*.

Ridgway, S. E., Heckman, T. M., Calzetti, D., and Lehnert, M. (2001). Nicmos imaging of the host galaxies of z$\sim$ 2-3 radio-quiet quasars. *The Astrophysical Journal*, 550(1):122.

Rodighiero, G., Cimatti, A., Gruppioni, C., Popesso, P., Andreani, P., Altieri, B., Aussel, H., Berta, S., Bongiovanni, A., Brisbin, D., et al. (2010). The first herschel view of the mass-sfr link in high-z galaxies. *Astronomy & Astrophysics*, 518:L25.

Rosario, D., Trakhtenbrot, B., Lutz, D., Netzer, H., Trump, J., Silverman, J., Schramm, M., Lusso, E., Berta, S., Bongiorno, A., et al. (2013). The mean star-forming properties of qso host galaxies. *Astronomy & Astrophysics*, 560:A72.

Rowan-Robinson, M. (1977). On the unity of activity in galaxies. *The Astrophysical Journal*, 213:635–647.

Salpeter, E. (1964). Accretion of interstellar matter by massive objects. *The Astrophysical Journal*, 140:796–800.

Sánchez, C., Carrasco Kind, M., Lin, H., Miquel, R., Abdalla, F. B., Amara, A., Banerji, M., Bonnett, C., Brunner, R., Capozzi, D., et al. (2014). Photometric redshift analysis in the dark energy survey science verification data. *Monthly Notices of the Royal Astronomical Society*, 445(2):1482–1506.

Sanders, D., Soifer, B., Elias, J., Madore, B., Matthews, K., Neugebauer, G., and Scoville, N. (1988). Ultraluminous infrared galaxies and the origin of quasars. *The Astrophysical Journal*, 325:74–91.

Scannapieco, E., Silk, J., and Bouwens, R. (2005). Agn feedback causes downsizing. *The Astrophysical Journal Letters*, 635(1):L13.

Schmidt, M. (1963). 3c273: a star-like object with large red-shift.".

Schneider, D. P., Richards, G. T., Hall, P. B., Strauss, M. A., Anderson, S. F., Boroson, T. A., Ross, N. P., Shen, Y., Brandt, W., Fan, X., et al. (2010). The sloan digital sky survey quasar catalog. v. seventh data release. *The Astronomical Journal*, 139(6):2360.

Shankar, F., Weinberg, D. H., and Miralda-Escudé, J. (2008). Self-consistent models of the agn and black hole populations: duty cycles, accretion rates, and the mean radiative efficiency. *The Astrophysical Journal*, 690(1):20.

Shao, L., Lutz, D., Nordon, R., Maiolino, R., Alexander, D., Altieri, B., Andreani, P., Aussel, H., Bauer, F., Berta, S., et al. (2010). Star formation in agn hosts in goods-n. *Astronomy & Astrophysics*, 518:L26.

Shields, G. (1978). Thermal continuum from accretion disks in quasars. *Nature*, 272(5655):706.

Sijacki, D., Springel, V., Di Matteo, T., and Hernquist, L. (2007). A unified model for agn feedback in cosmological simulations of structure formation. *Monthly Notices of the Royal Astronomical Society*, 380(3):877–900.

Smith, E. P., Heckman, T., Bothun, G., Romanishin, W., and Balick, B. (1986). On the nature of qso host galaxies. *The Astrophysical Journal*, 306:64–89.

Stanley, F., Harrison, C., Alexander, D., Swinbank, A., Aird, J., Del Moro, A., Hickox, R., and Mullaney, J. (2015). A remarkably flat relationship between the average star formation rate and agn luminosity for distant x-ray agn. *Monthly Notices of the Royal Astronomical Society*, 453(1):591–604.

Stevens, J. A., Page, M., Ivison, R., Carrera, F., Mittaz, J., Smail, I., and McHardy, I. (2005). Submillimetre photometry of x-ray absorbed quasi-stellar objects: their formation and evolutionary status. *Monthly Notices of the Royal Astronomical Society*, 360(2):610–618.

Symeonidis, M., Giblin, B., Page, M., Pearson, C., Bendo, G., Seymour, N., and Oliver, S. (2016). Agn are cooler than you think: the intrinsic far-ir emission from qsos. *Monthly Notices of the Royal Astronomical Society*, 459(1):257–276.

Symeonidis, M. and Page, M. (2018). What powers hyperluminous infrared galaxies at z$\sim$ 1–2? *Monthly Notices of the Royal Astronomical Society: Letters*.

Tokunaga, A. T. and Vacca, W. (2005). The mauna kea observatories near-infrared filter set. iii. isophotal wavelengths and absolute calibration. *Publications of the Astronomical Society of the Pacific*, 117(830):421.

Tran, H. D. (2001). Hidden broad-line seyfert 2 galaxies in the cfa and 12 μm samples. *The Astrophysical Journal Letters*, 554(1):L19.

Treister, E., Schawinski, K., Urry, C., and Simmons, B. (2012). Major galaxy mergers only trigger the most luminous active galactic nuclei. *The Astrophysical Journal Letters*, 758(2):L39.

Treister, E., Schawinski, K., Volonteri, M., Natarajan, P., and Gawiser, E. (2011). Black hole growth in the early universe is self-regulated and largely hidden from view. *Nature*, 474(7351):356.

Tremaine, S., Gebhardt, K., Bender, R., Bower, G., Dressler, A., Faber, S. M., Filippenko, A. V., Green, R., Grillmair, C., Ho, L. C., et al. (2002). The slope of the black hole mass versus velocity dispersion correlation. *The Astrophysical Journal*, 574(2):740.

Urrutia, T., Lacy, M., and Becker, R. H. (2008). Evidence for quasar activity triggered by galaxy mergers in hst observations of dust-reddened quasars. *The Astrophysical Journal*, 674(1):80.

Urrutia, T., Lacy, M., Spoon, H., Glikman, E., Petric, A., and Schulz, B. (2012). Spitzer observations of young red quasars. *The Astrophysical Journal*, 757(2):125.

Vanden Berk, D. E., Wilhite, B. C., Kron, R. G., Anderson, S. F., Brunner, R. J., Hall, P. B., Ivezić, Ž., Richards, G. T., Schneider, D. P., York, D. G., et al. (2004). The ensemble photometric variability of$\sim$ 25,000 quasars in the sloan digital sky survey. *The Astrophysical Journal*, 601(2):692.

Vanden Berk, D. E. V., Shen, J., Yip, C.-W., Schneider, D. P., Connolly, A. J., Burton, R. E., Jester, S., Hall, P. B., Szalay, A. S., and Brinkmann, J. (2006). Spectral decomposition of broad-line agns and host galaxies. *The Astronomical Journal*, 131(1):84.

Vestergaard, M. and Peterson, B. M. (2006). Determining central black hole masses in distant active galaxies and quasars. ii. improved optical and uv scaling relationships. *The Astrophysical Journal*, 641(2):689.

Villforth, C., Hamann, F., Rosario, D., Santini, P., McGrath, E., Wel, A., Chang, Y., Guo, Y., Dahlen, T., Bell, E., et al. (2014). Morphologies of z 0.7 agn host galaxies in candels: no trend of merger incidence with agn luminosity. *Monthly Notices of the Royal Astronomical Society*, 439(4):3342–3356.

Villforth, C., Hamilton, T., Pawlik, M., Hewlett, T., Rowlands, K., Herbst, H., Shankar, F., Fontana, A., Hamann, F., Koekemoer, A., et al. (2016). Host galaxies of luminous z 0.6 quasars: Major mergers are not prevalent at the highest agn luminosities. *Monthly Notices of the Royal Astronomical Society*, page stw3037.

Wang, M., Li, A., Xiang, F., Tang, Y., and Zhong, J. (2014). Dust in active galactic nuclei. 44:771.

Weingartner, J. C. and Draine, B. (2001). Dust grain-size distributions and extinction in the milky way, large magellanic cloud, and small magellanic cloud. *The Astrophysical Journal*, 548(1):296.

Weiß, A., Ivison, R., Downes, D., Walter, F., Cirasuolo, M., and Menten, K. (2009). First redshift determination of an optically/ultraviolet faint submillimeter galaxy using co emission lines. *The Astrophysical Journal Letters*, 705(1):L45.

White, S. D. and Frenk, C. S. (1991). Galaxy formation through hierarchical clustering. *The Astrophysical Journal*, 379:52–79.

Xu, L., Rieke, G. H., Egami, E., Haines, C., Pereira, M., and Smith, G. (2015). The relation between luminous agns and star formation in their host galaxies. *The Astrophysical Journal*, 808(2):159.

Young, S., Axon, D., Robinson, A., and Capetti, A. (2009). The contribution from scattered light to quasar galaxy hosts. *The Astrophysical Journal Letters*, 698(2):L121.

Zel'dovich, Y. B. and Novikov, I. D. (1965). Relativistic astrophysics. i. *Physics-Uspekhi*, 7(6):763–788.

APPENDIX

A

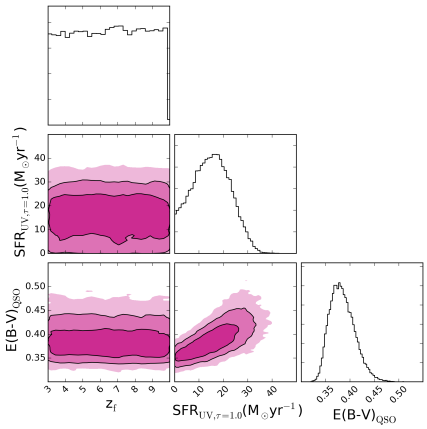

(a) ULASJ0016-0038

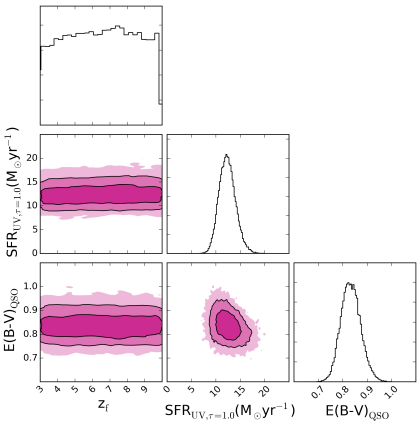

(b) ULASJ1002+0137

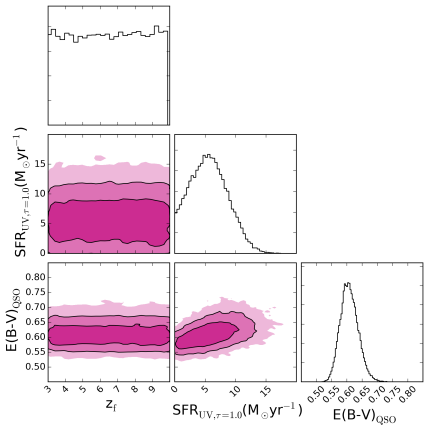

(c) VHSJ2024-5623

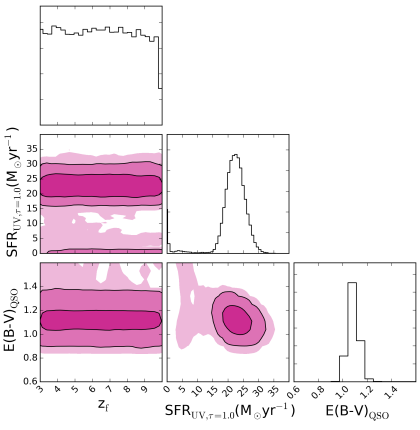

(d) VHSJ2028-5740

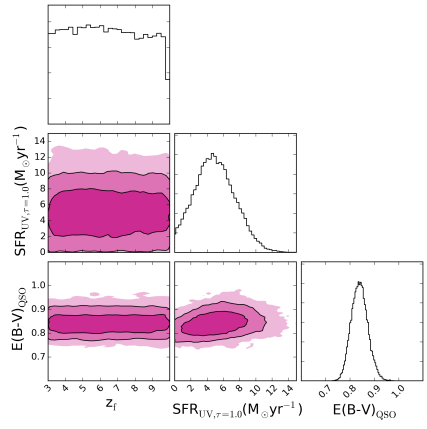

(e) VHSJ2100-5820

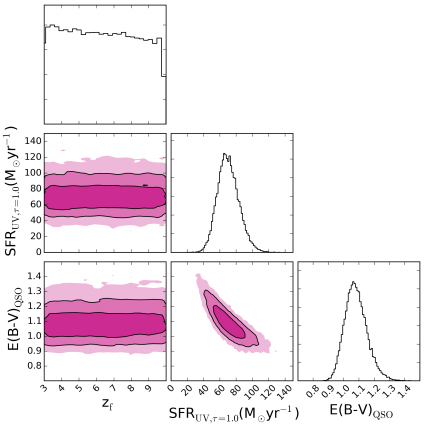

(f) VHSJ2115-5913

Fig. A.1 1D and 2D posterior distributions from the MCMC fitting. Shaded regions in the 2D distributions denote 1,2 and 3σ parameter uncertainties in the fitting. $SFR_{UV,\tau_v=1.0}$ and associated uncertainties (prior to dust corrections) are based on a galaxy template with τ_V = 1.0 and have been converted from the normalisation of the galaxy template (f_{gal}) in the fitting. Histograms illustrate the relative 1D probability distributions for each parameter.

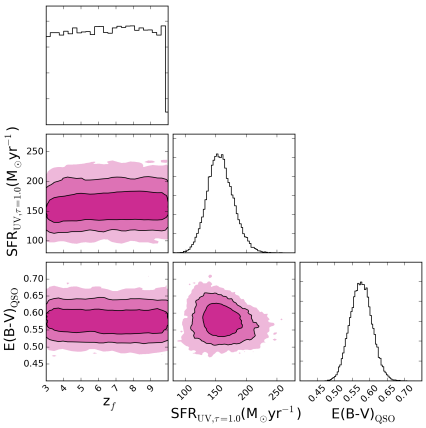

(g) ULASJ2200+0056

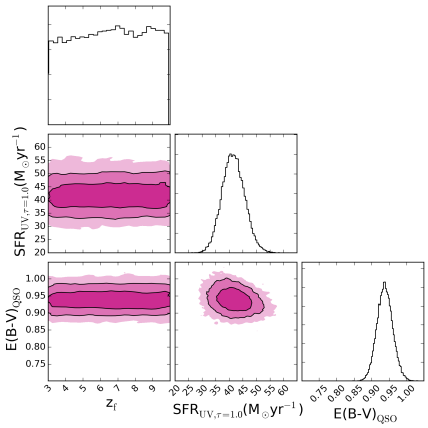

(h) VHSJ2220-5618

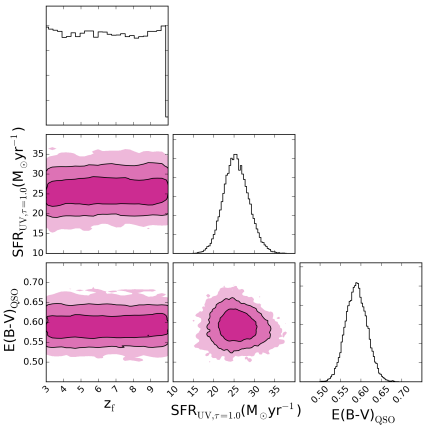

(i) ULASJ2224-0015

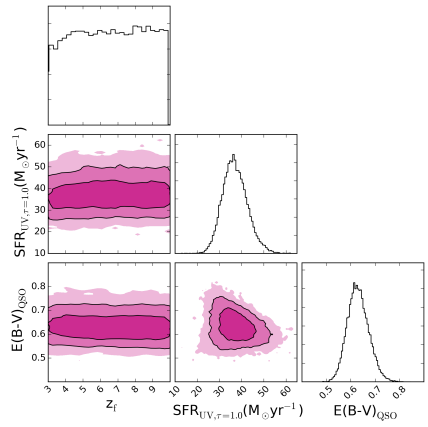

(j) VHSJ2227-5203

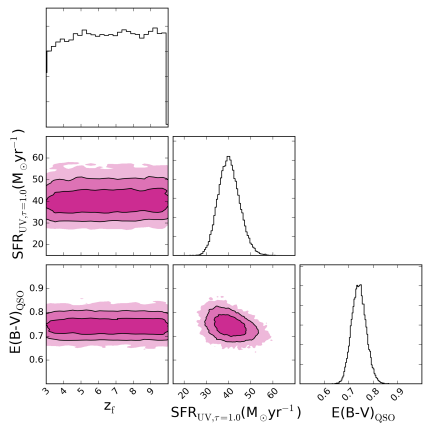

(k) VHSJ2235-5750

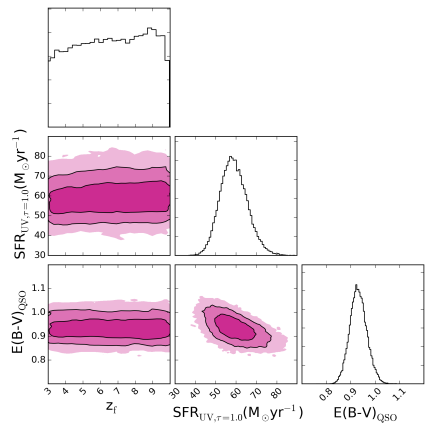

(l) VHSJ2355-0011

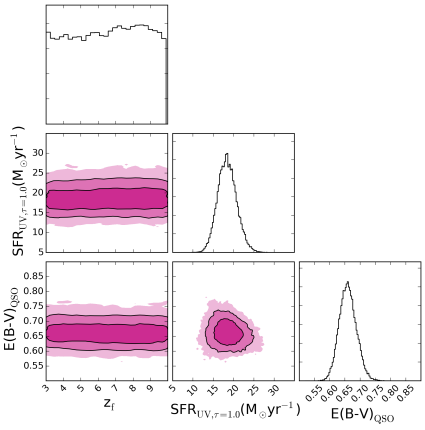

(m) VHSJ2306-5447

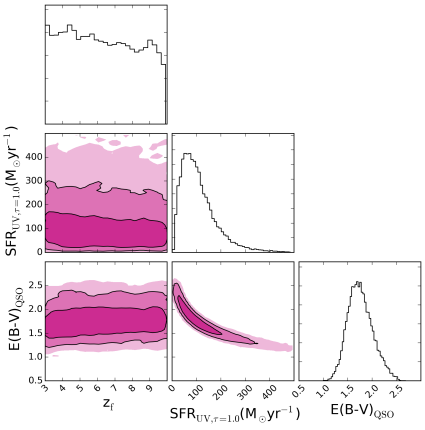

(n) ULASJ2315+0143

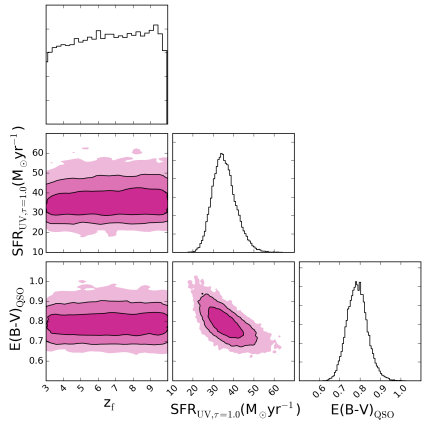

(o) VHSJ2332-5240

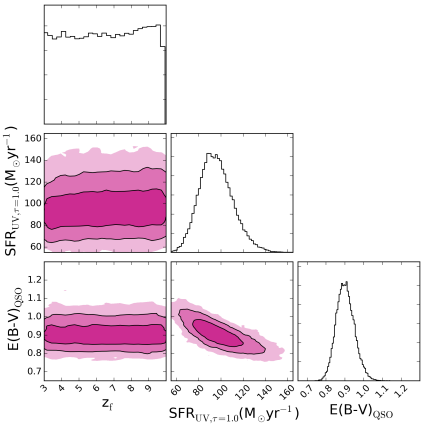

(p) VHSJ2355-0011

Table A.1 Reduced χ^2 results for all objects in the sample. Those marked with an '*' denote values calculated prior to the correction of the Hα equivilant width in models which were discounted for the reasons outlined in Section 2.4. We note however, that the difference in the Hα equivilant width would make little difference to the measured goodness of fit in these models.

Name	Quasar	Quasar + Galaxy	Scattered Continuum	Lyman-α
ULASJ0016-0038	2.64	3.01	4.35*	4.84*
ULASJ1002+0137	13.83	0.96	1.32	17.30
VHSJ2024-5623	1.33	1.29	1.29	1.47
VHSJ2028-5740	15.59	3.25	3.37	14.74
VHSJ2100-5820	1.43	1.15	1.15	1.17
VHSJ2115-5913	26.85	1.48	0.89	14.09
ULASJ2200+0056	6.19	0.13	0.35	7.70
VHSJ2220-5618	20.43	1.04	2.588*	18.12*
ULASJ2224-0015	9.44	2.86	3.96*	13.31*
VHSJ2227-5203	9.08	5.66	6.23	8.12
VHSJ2235-5750	12.20	0.48	0.47	3.83
VHSJ2256-4800	24.79	3.52	3.54	3.54
VHSJ2257-4700	0.44	0.54	0.77*	0.79*
VHSJ2306-5447	9.85	2.58	1.30*	12.43*
ULASJ2315+0143	28.15	1.08	0.88	22.11
VHSJ2332-5240	15.59	2.76	1.75	4.87
VHSJ2355-0011	29.72	3.06	1.53	14.91

APPENDIX

B

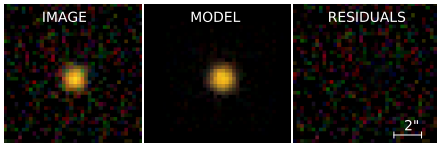

(a) ULASJ0016-0038

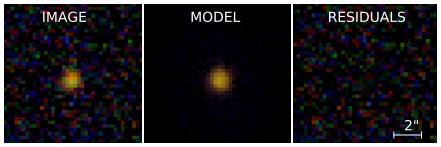

(b) VHSJ2024-5623

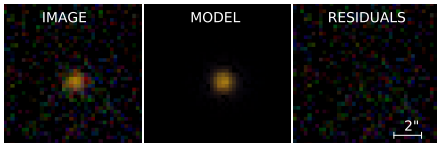

(c) VHSJ2028-5740

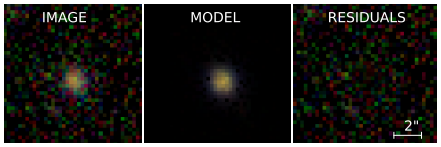

(d) VHSJ2115-5913

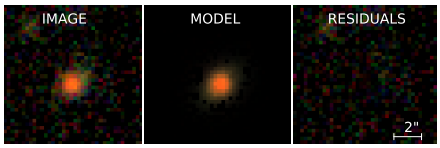

(e) VHSJ2220-5618

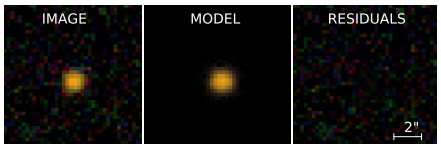

(f) ULASJ2224-0015

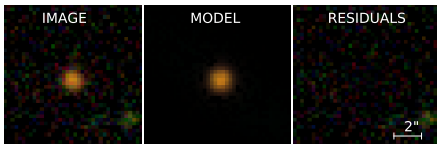

(g) VHSJ2227-5203

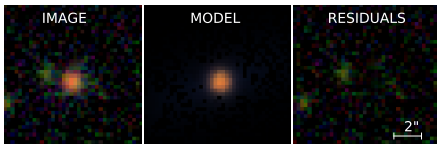

(h) VHSJ2235-5750

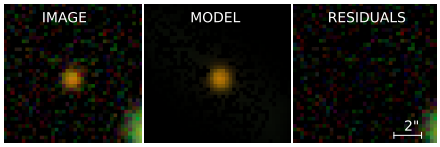

(i) VHSJ2257-4700

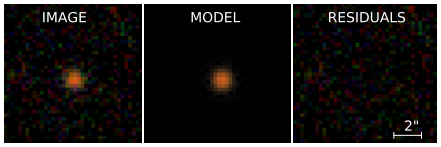

(j) VHSJ2306-5447

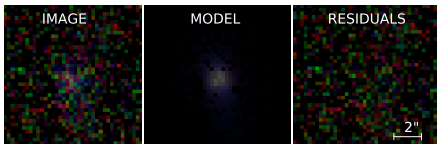

(k) ULASJ2315+0143

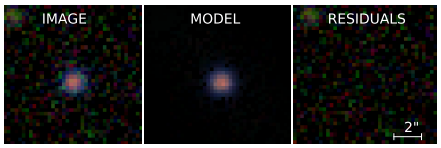

(l) VHSJ2355-0011

Fig. B.1 (data-model) residual plots across our full sample shown as a *g* (*blue*), *i* (*green*), *z* (*red*) colour image. Residuals appear consistent with the noise level of the image in 13 objects in our sample

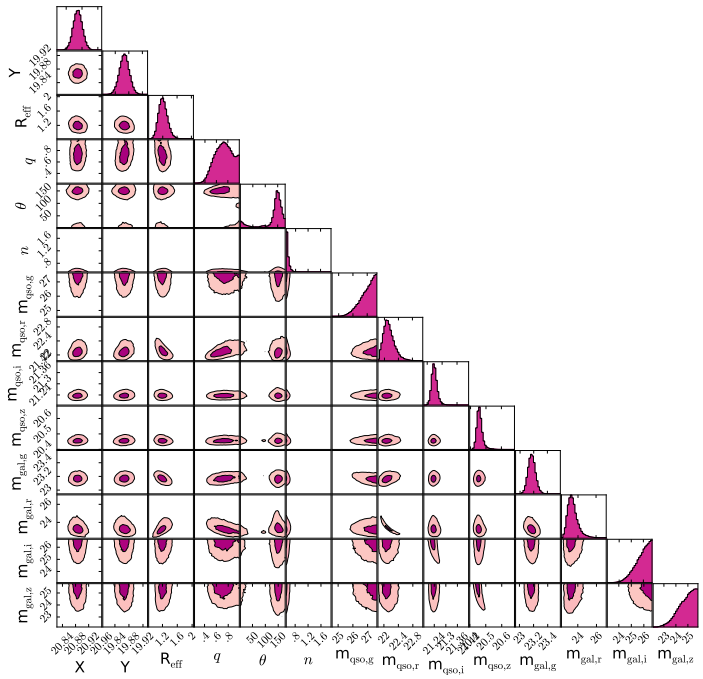

(a) ULASJ0016-0038

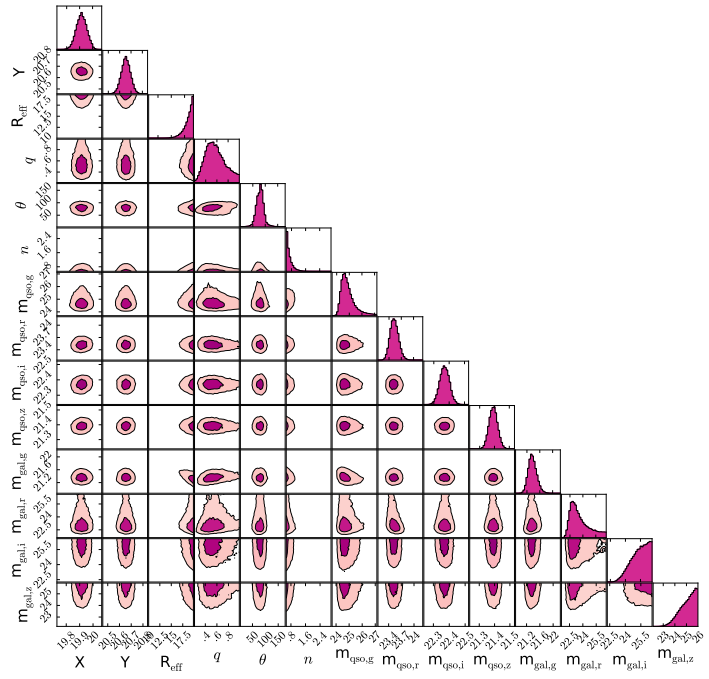

(b) VHSJ2024-5623

Fig. B.2 1D and 2D parameter solutions for all galaxies in our DES Y3A1 sample.

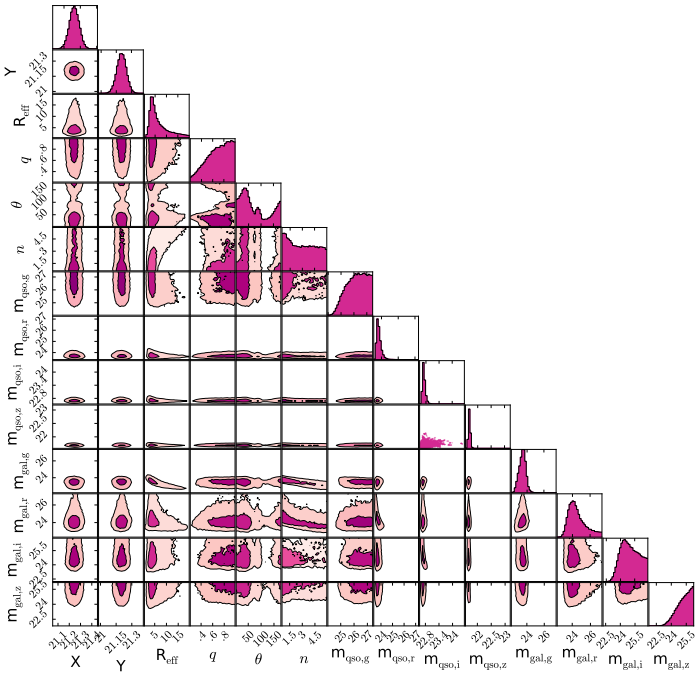

(c) VHSJ2028-5740

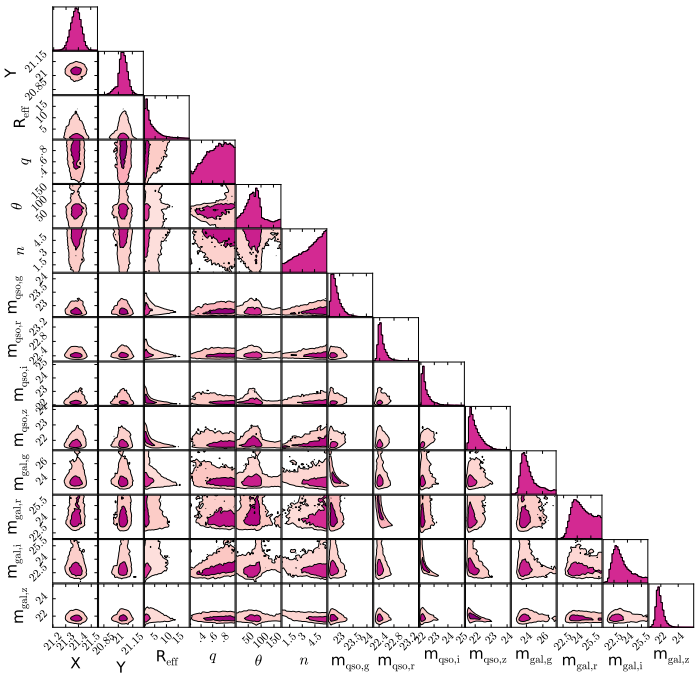

(d) VHSJ2115-5913

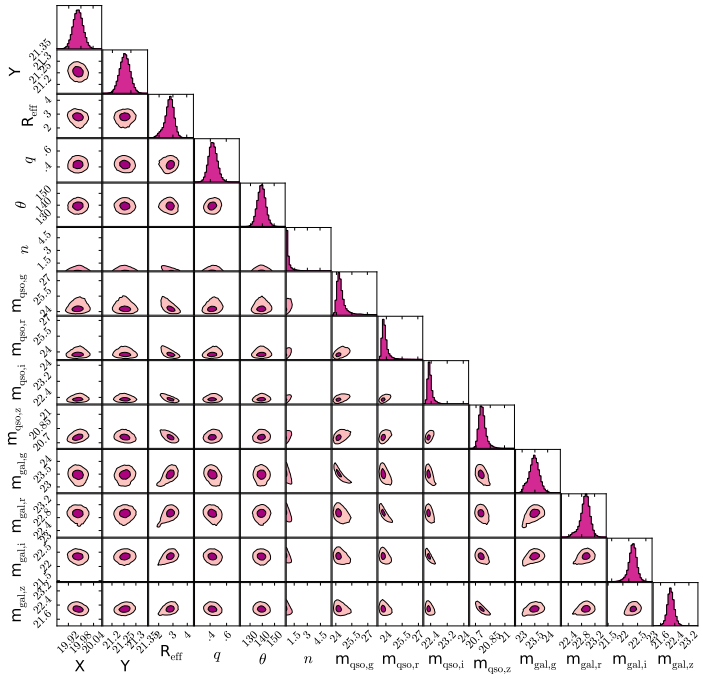

(e) VHSJ2220-5618

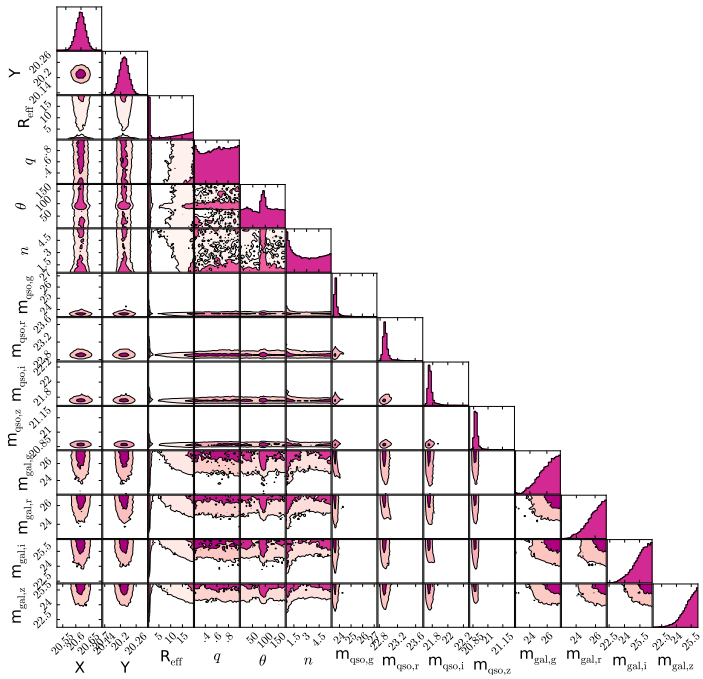

(f) ULASJ2224-0015

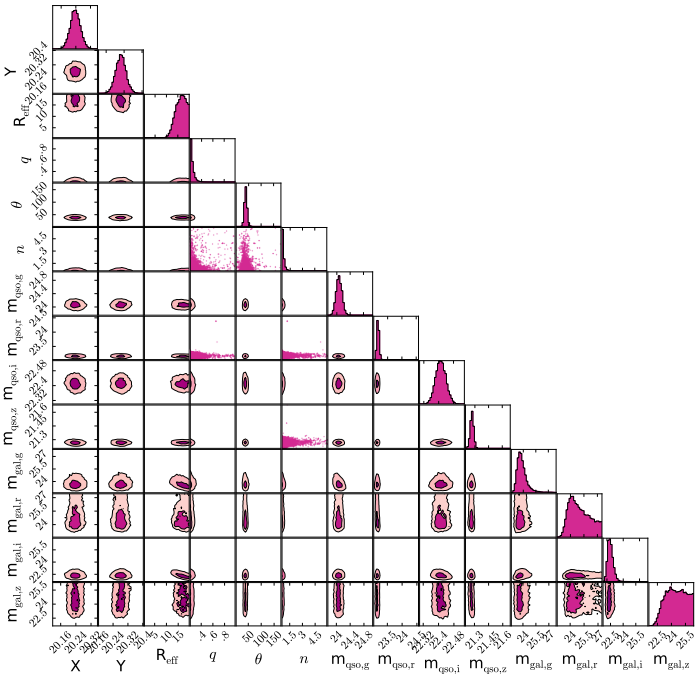

(g) VHSJ2227-5203

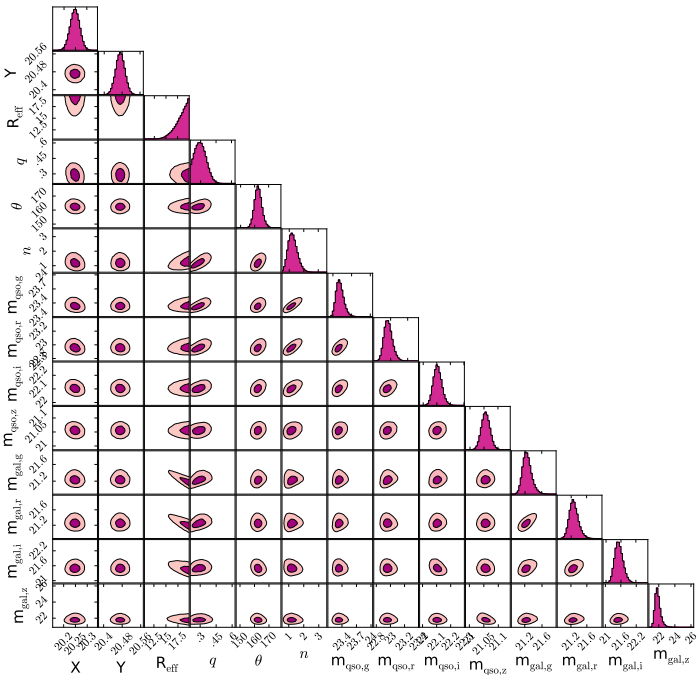

(h) VHSJ2235-5750

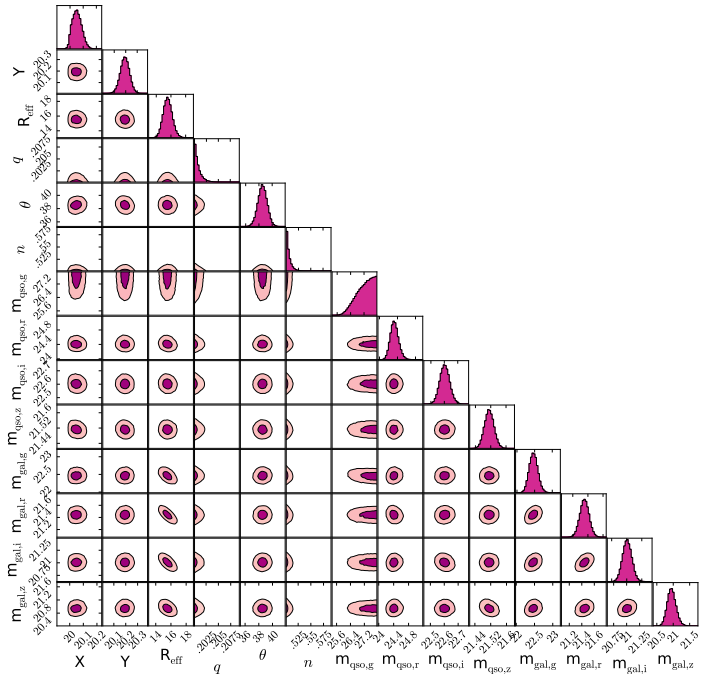

(i) VHSJ2257-4700

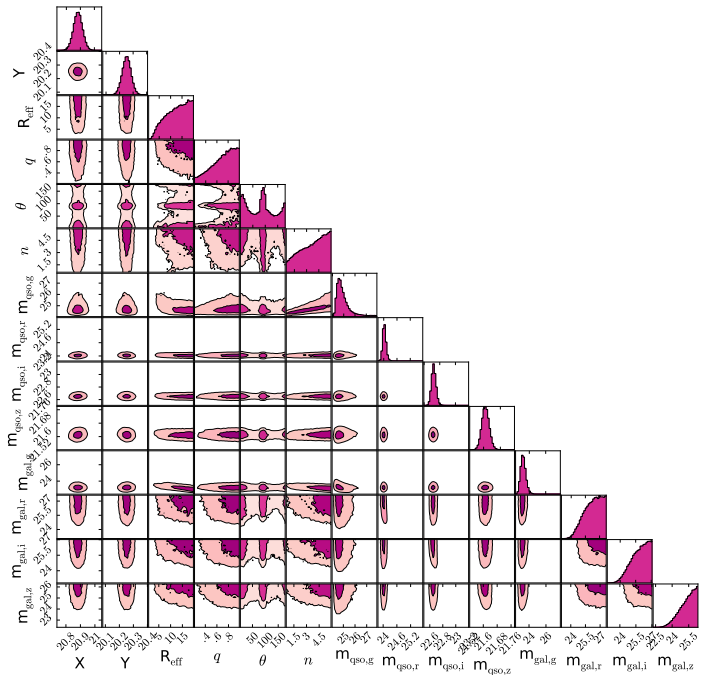

(j) VHSJ2306-5447

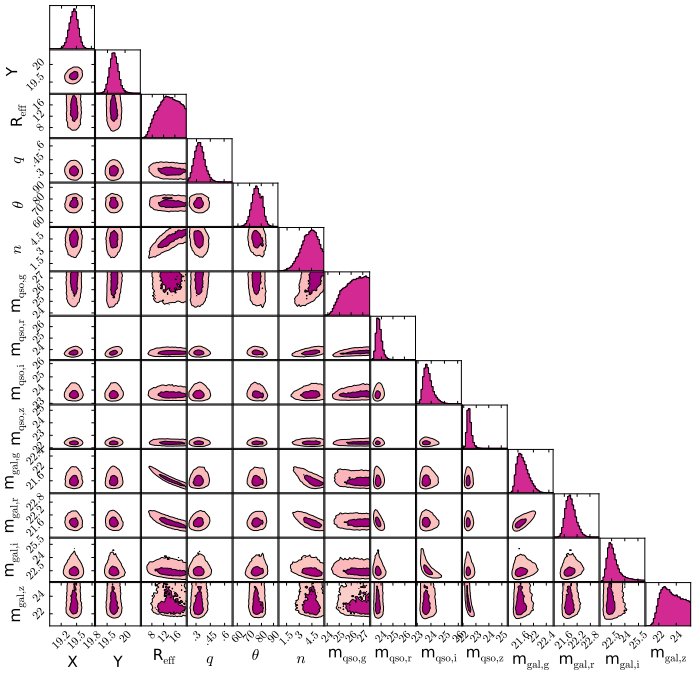

(k) ULASJ2315+0143

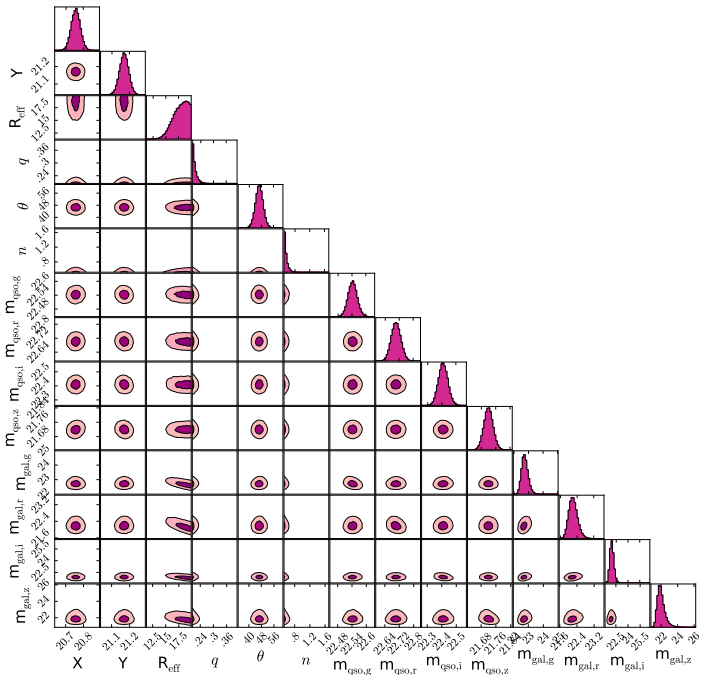

(l) VHSJ2355-0011